Influence of Grain Size, Morphology and Aggregation on Galena Dissolution

Juan Liu

Dissertation submitted to the faculty of the Virginia Polytechnic Institute and State University in partial fulfillment of the requirements for the degree of

Doctor of Philosophy
In
Geosciences

Michael F. Hochella, Jr., Chair
Deborah M. Aruguete
J. Donald Rimstidt
Madeline E. Schreiber

January 30, 2009
Blacksburg, VA

Keywords: galena (PbS), nanoparticle, dissolution, high-resolution transmission electron microscopy (HRTEM), size, morphology, aggregation

Influence of Grain Size, Morphology and Aggregation on Galena Dissolution

Juan Liu

Abstract

The acidic, non-oxidative dissolution of galena nanocrystals has been studied using both microscopic and wet-chemical methods. The effects of particle size, shape, aggregation state, and grain proximity on dissolution rates were investigated. Nearly monodisperse galena nanocrystals with an average diameter of 14.4 nm and a truncated cubic shape were synthesized. In the dissolution experiments of dispersed nanocrystals, galena nanocrystals attached on the surface of a TEM grid were exposed to deoxygenated HCl solutions (pH 3) at 25 °C. Capping groups on nanocrystals were removed via a washing process, and chemistry of nanocrystals was examined using X-ray photoelectron spectroscopy (XPS). The evolution of the size and shape of the pre- and post-dissolution nanocrystals were studied using transmission electron microscopy (TEM), and the dissolution rate was calculated directly according to the size shrinking of galena nanocrystals. To assess the size effect, galena microcrystals (~ 3 μm) were synthesized and dissolved under similar conditions to the dispersed nanocrystals. The results showed that the nanocrystals dissolved at a surface area normalized rate of one order of magnitude faster than the microcrystals. In addition, dissolution rate is orientation-dependent on a single nanocrystal. High-resolution TEM (HRTEM) images indicated the {111} and {110} faces dissolve faster than {100} faces on galena nanocrystals, rationalized by the average coordination number of ions on each of these faces. To assess the aggregation effect, dissolution experiments of aggregated galena nanocrystals were conducted using a wet-chemical method, and the results were compared with the rates of microcrystals and dispersed nanocrystals. These experiments showed that the rate of aggregated nanocrystals is in the same order of magnitude as the rate of microcrystals, but one order of magnitude smaller than that of dispersed nanocrystals. Finally, the effect

of the close proximity between nanocrystals on dissolution was observed by HRTEM. Dissolution was greatly inhibited on nanocrystal surfaces that were closely adjacent (1-2 nm, or less) to other nanocrystals, which is probably relevant to the slow dissolution of aggregated nanocrystals. The dissolution phenomena of galena nanocrystals observed in this study is likely important for understanding the environmental fate and behavior of nanoparticles in aquatic systems.

Acknowledgements

First and foremost, I would like to sincerely thank my advisor, Mike Hochella. Over the four and a half years, Mike has given me the freedom to pursue my scientific interests, provided insightful advice and guidance, taught me great skills in researching, writing, and presenting, etc. I consider myself extremely lucky to have had Mike as my advisor. Thank you for everything you've done for me. I would also like to thank many past and present members in the Mike's group for providing an excellent research/learning environment. I'd also like to thank my committee members for the time they put in to help me establish and complete this research study. In particular, I want to say a big thank you to Deborah for working closely with me on my research and teaching me a lot about nanoparticle synthesis.

I'd like to acknowledge Steve McCartney, Frank Cromer, Jerry Hunter, John McIntosh, Joerg Jinschek, and Mitsuhiro Murayama for their help with SEM, XPS, and TEM measurements. I would also like to thank Matthew Eick, Lucian Zelazny, Todd Luxton, Athena Tilley, and Patricia Dove, for all the helpful advice and the use of their equipments. Nizhou Han deserves special thanks for helping me and giving me invaluable advice with aspect to various matters, including my research and life, over these years. I really appreciate her generous help and time. I want to thank the staff members of the Department of Geosciences for their help behind the scenes.

I would also like to express appreciation to many friends I met in Virginia Tech, some of whom remain in Blacksburg and some who have moved on. Thank you all for your support on both personal and professional levels. I would specially like to thank Bing Shen for valuable discussions about my research, and Yaodong Yang for lending me the synthesis apparatus.

Financial assistance for this study was provided by the U.S. Department of Energy (DE-FG02-06ER15786) and the Institute for Critical Technology and Applied Science (ICTAS) at Virginia Tech.

This work could not have been completed without the continuous support and encouragement of my family. Special thanks to my husband, Junyi, for his great love,

support, and understanding. Studying abroad is not very easy. His involvement with every aspect of my life makes my every day so much easier and happier.

Attributions

Several colleagues aided in the research presented within this dissertation. A brief description of their backgrounds and their contributions are included here.

Prof. Michael F. Hochella, Jr. (Dept. of Geosciences, Virginia Tech) is the primary advisor who was responsible for funding all of this work. He provided scientific guidance and writing assistance on this entire dissertation.

Dr. Deborah Aruguete (Dept. of Geosciences, Virginia Tech) provided scientific assistance and advice in nanoparticle synthesis and experiment design, assisted writing chapter 2, and wrote the appendix B.

Prof. J. Donald Rimstidt (Dept. of Geosciences, Virginia Tech) provided scientific guidance of analyzing the dissolution data and designing dissolution experiments.

Dr. Joerg R. Jinschek (FEI Europe Nanoport) provided scientific guidance regarding TEM and helped with TEM experimental design.

Table of Contents

Abstract ... ii

Acknowledgements ... iv

Attributions ... vi

Table of Contents ... vii

Table of Figures ... ix

List of Tables ... xi

Chapter 1 - Introduction ... 1

Nanominerals in the environment ... 1
Methods for dissolution studies ... 2
Nanomaterial dissolution ... 4
Sulfide dissolution ... 6
Dissertation outline ... 7
References ... 9

Chapter 2 - The non-oxidative dissolution of galena nanocrystals: Insights into mineral dissolution rates as a function of grain size, shape, and aggregation state ... 12

Abstract ... 12
2.1. Introduction ... 13
2.2. Materials and Methods ... 15
2.2.1. Galena Synthesis and preparation for dissolution experiments ... 15
2.2.2. Dissolution Experiments ... 16
2.2.3. Characterization of Galena Nanocrystals ... 16
2.2.3.1. X-ray diffraction (XRD) ... 16
2.2.3.2. X-ray Photoelectron Spectroscopy (XPS) ... 16
2.2.3.3.Transmission Electron Microscopy (TEM) ... 17
2.3. Results and Discussion ... 18
2.3.1. Pre-dissolution galena nanocrystals ... 18
2.3.1.1. XRD crystal structure and particle size ... 18
2.3.1.2. Chemical composition of nanocrystals ... 18
2.3.1.3. Pre-dissolution crystal structure and morphology observed by HRTEM ... 20
2.3.2. Shape and Size Evolution of Post-dissolution PbS Nanocrystals ... 21
2.3.2.1. Shape evolution ... 21
2.3.2.2. Statistical analysis of size evolution ... 22
2.3.2.3.HRTEM observations of nanocrystal morphology evolution ... 24
Isolated nanocrystals ... 24
Particle clusters ... 26
2.4. Implications ... 27

Acknowledgements 29
Appendix A - Calculation of geometric surface area (Ageo) and Ageo normalized dissolution rate (Rgeo) 30
References 46

Chapter 3 - Influence of size and aggregation on the non-oxidative dissolution of galena (PbS) 49
References and Notes 56
Supporting online material 58

Appendix B - Size/shape-property relationships of non-carbonaceous inorganic nanoparticles: Towards an understanding of environmental implications 75

Table of Figures

Figure 2.1. X-ray diffraction pattern of PbS nanocrystals……....32

Figure 2.2. Bright field TEM images of PbS nanocrystals (a) before wash, (b) after wash, (c) after wash and 2-hour-dissolution, as well as (d) after wash and 3-hour-dissolution. Scale bar is 10 nm……..33

Figure 2.3. Normalized XPS survey scans for natural and synthetic galena samples: (a) synthetic galena before washing, (b) fresh surfaces of natural galena exposed by grinding after exposure to air for two weeks, (c) synthetic galena after washing……....34

Figure 2.4. C1s XPS spectra for: (a) natural galena, (b) synthetic galena nanocrystals without wash, (c) washed galena nanocrystals before dissolution, (d) washed galena nanocrystals after dissolution…….35

Figure 2.5. Pb4f XPS spectra for: (a) natural galena, (b) washed galena nanocrystals before dissolution, (c) washed galena nanocrystals after dissolution……36

Figure 2.6. S2p XPS spectra for: (a) natural galena, (b) washed galena nanocrystals before dissolution, (c) washed galena nanocrystals after dissolution……37

Figure 2.7. O1s XPS spectra for: (a) natural galena, (b) washed galena nanocrystals before dissolution, (c) washed galena nanocrystals after dissolution……38

Figure 2.8. HRTEM images of isolated PbS nanocrystals before dissolution (a and c), and after 3-hour-dissolution (b and d). (a) and (b) are viewed along <100> zone axis. (c) and (d) are viewed along <110> zone axis . {110} and {111} faces developed faster relative to {100} faces……...……....39

Figure 2.9. (a) Plots of the ratio of particle width in <100> orientation to the width in <110> orientation, as schematically depicted in the insert. Sample a is the washed particles before dissolution, and sample b is the particles after 2-hr dissolution. The dots represent the raw data and the circles are the mean values. The vertical bars in the plot represent 95% confidence intervals for the mean. (b) Schematic drawing of typical morphology change of PbS nanocrystal upon dissolution…….40

Figure 2.10. Variation in shape descriptors of PbS nanocrytals as a function of dissolution time. Solid squares and circles are the mean values of aspect ratio and roundness, respectively. The vertical bars in the plot represent 95% confidence intervals for the mean……...41

Figure 2.11. Mean diameter of galena nanocrystals dependence on dissolution time at pH 3 and 25°C. The solid line represents the linear regression of all data. ($\Delta d/\Delta t$) = -1.020 nm/hr……..42

Figure 2.12. Two examples of steps on galena nanocrystals after dissolution……..…..43

Figure 2.13. (a) HRTEM image of pre-dissolution PbS nanocrystal cluster. The inter-particle spacing is nanoscaled. (b) HRTEM image of the post-dissolution PbS nanocrystal, P_1, adjacent to two nanocrystals, P_2 and P_3. {110} faces on the left side, open to bulk solution, are dissolved faster than the equivalent faces on the right side, close to other particles…….44

Figure 2.14. HRTEM image of PbS nanocrystal formed by oriented attachment. (a) is a pre-dissolution nanocrystal. (b) and (c) are the Fast Fourier Transform (FFT) pattern of the upper and the lower primary building blocks, respectively. (d) is a post-dissolution nanocrystal. (e) and (f) are high-magnification images of the interfaces between primary building blocks……...45

Figure 3.1. Comparison of nanoscale and microscale galena particles. (a) TEM images of galena nanocrystals. (b) the size distribution of nanocrystals. (c) SEM images of galena microcrystals. (d) the size distribution of microcrystals……62

Figure 3.2. Lead concentration vs. time in the dissolution of galena particles in HCl solution at pH 3 and 25 °C. (a) galena microcrysals. The line is the linear fit of raw data. Its slope is $(\Delta C_{Pb}/\Delta t) = 0.01865$ mg L^{-1} h^{-1}. (b) nanocrystals aggregates using 100nm filter (■) and 6 nm filter (○), respectively. The slope of the solid line is $(\Delta C_{Pb}/\Delta t) = 0.4926$ mg L^{-1} h^{-1}; the slope of the dashed line is $(\Delta C_{Pb}/\Delta t) = 0.458$ mg L^{-1} h^{-1}……63

Figure 3.3. Representative SEM (a) and bight-field TEM (b) image of galena nanoparticle aggregates. (c) High-resolution TEM image of the nanoscale interparticle spacing in a nanoparticle cluster……64

List of Tables

Table 2.1. Binding energies and peak area ratios (I_C:I_{Pb} and I_O:I_{Pb}) of various XPS peaks on natural and synthetic galena samples……31

Table 3.1. Size, geometric SSA (A_{geo}), BET SSA (A_{BET}), geometric surface area normalized dissolution rate (R_{geo}), and BET surface area normalized dissolution rate (R_{BET}) of primary nanocrystals, microcrystals, and nanocrytal aggregates……...57

Chapter 1 – Introduction

Nanominerals in the environment

In recent years, nanocrystalline materials widely present in solid earth materials, the hydrosphere, the atmosphere, and the biosphere have attracted more and more attention (Banfield and Navrotsky, 2001; Hochella et al., 2008). The visible improvement of synthesis and characterization techniques for nanomaterials offers a unique opportunity for "nanogeoscience". In natural environments, nanoparticles can be produced via a variety of natural inorganic and biological pathways (Banfield and Navrotsky, 2001; Gilbert and Banfield, 2005; Hochella et al., 2008). In addition, with the increasing application of nanotechnology in industry, many manufactured nanomaterials will be exposed to the environment as an unintended consequence of human activity (Christian et al., 2008). Nanomaterials account for a disproportionately large amount of potentially reactive surface area in the environment because of their very high surface area to volume ratio.

A great deal of research has shown the nanoscale inorganic solids may exhibit substantially modified properties relative to their bulk counterparts (e.g. Alivisatos, 1996; Murray et al., 2000; Trindade et al., 2001; Madden and Hochella, 2005). These size-dependent structures and properties of nanominerals impact the geologic processes that they participate in (Banfield and Navrotsky, 2001; Gilbert and Banfield, 2005; Wigginton et al., 2007). One of the most important size-dependent properties for minerals is solubility, which affects many Earth surface processes. Understanding solubility and reactivity of nanominerals in aqueous solution is critical for predicting their mobility and fate in water-based environmental settings (Borm et al., 2006). However, as is apparent from chapter 2, few studies that target the size-dependent dissolution of minerals have been carried out.

Investigating size-dependent properties of pure nanomaterials is only the first step in understanding the likely fate and behaviour of nanominerals in the environment. In natural aquatic systems, nanominerals may interact with natural water components, including colloids, natural organic matter (NOM), contaminants, and aqueous ions. As a result of these interactions, many processes, such as the formation of NOM surface

coatings on nanominerals, aggregation, disaggregation, sorption of contaminants onto nanoparticles, etc., may occur (Christian et al., 2008). These processes could change the properties of nanominerals and consequently affect their behavior in aquatic environment. To better estimate the reactivity and fate of nanominerals in the aquatic systems, it is essential to understand their interaction with natural water components and the potentially consequent processes. Aggregation is a common phenomenon affecting nanoparticles in waters, and the degree of aggregation is believed to greatly influence dissolution rate. However, no previous studies have been done to quantify this effect. Chapter 3 describes the first effort to specifically address the relationship between dissolution rate and aggregation state.

Although this dissertation focuses on investigating properties and dissolution of synthetic nanoparticles in laboratory systems, the systematic study of nanoparticle characteristics and their reactivity, as this and similar studies show, is the foundation for the next generation of risk assessment in more complex systems. Our understanding of the environmental implications of nanomaterials can be developed from controlled laboratory experiments to ecosystems with multiple organisms and phases. Extensive and interdisciplinary collaboration is needed to assess environmental impacts of nanomaterials. This study can supply useful information for investigations about nanoparticle transport in the environment, nanoparticle-organism interaction, toxicity and bioavailability of nanomaterials, environmental availability of nanomaterials in intermediate products and finished goods.

Methods for dissolution studies

Dissolution phenomena have been studied for more than a century and a half. The dissolution kinetics of materials are of critical importance in geosciences, material sciences, chemistry, and many industrial applications, such as food and pharmaceutical products, chemicals, fertilizers, paints. Dissolution is a complex process, which may involve some or all of the following elementary steps: (i) mass transport of solutes to the solid surface; (ii) surface attachment of the solutes; (iii) various surface chemical reactions at active surface sites; (iv) ion or molecule detachment from dissolution sites; and (v) mass transfer away from the crystal into bulk solution. When any of these surface

processes [steps (ii) to (iv)] is slow compared to the transport process [step (i) and step (v)], the dissolution reaction is called surface-controlled dissolution. Conversely, when the surface processes are relatively fast, the reaction is termed transport-controlled dissolution.

Particle dissolution studies can be performed utilizing "macroscopic" (bulk) approaches or "microscopic" approaches. In bulk experiments, a considerable amount of particles are dissolved, and the concentration of chemical species in solution is measured. The dissolution rate is deduced from the time evolution of this concentration. There are three fundamental types of experimental setups for bulk experiments: batch reactors, plug flow reactors, and mixed flow reactors (Rimstidt and Newcomb, 1993). In the dissolution study of galena nanoparticles in this dissertation, batch reactors were used in order to avoid the high mobility of nanoparticles in a flow-through system.

The microscopic approach is to directly observe the evolution of the surface topology or particle size at the microscopic scale. The dissolution rate is deduced from retreat velocity of surface features or from the shrinking rate of particle size. For example, the dissolution rate of phlogopite {001} surfaces was measured using in-situ atomic force microscopy (AFM) by examining the retreat velocity of etch pit walls on basal plane surfaces (Rufe and Hochella, 1999). Particle size analysis by microscopic techniques can also be used to study dissolution. The change of particle size distribution as a function of time could be used to obtain a particle dissolution profile(Liu et al., 2008). Electron microscopy or optical microscopy is capable of enabling visualization of the particle dissolution process. Especially for nanomaterial studies, Transmission Electron Microscope (TEM) plays an indispensable role is size measurement and crystal structure determination.

As an important complement to experimental observation, theoretical calculation can also be used to describe fundamental atomic processes during dissolution (Lasaga, 1990). Many mathematical models have been developed to explain experimental observations of dissolution. For example, Marabi et al. (2008) investigated the kinetics of sucrose particle dissolution utilizing images of single dissolving particles, and modeled the dissolution process based on the viscosity of the dissolving medium predicted from the Einstein-Stokes equation.

Nanomaterial dissolution

Worldwide concerns about global climate change, pollution, and ground-water management have led to an intense interest in the science of crystal dissolution (LASAGA and LUTTGE, 2003). Recent reports about the presence of nanoparticles in nature arouse a tremendous interest in determining solubility of geomaterials as a function of particle size. The expectation that finely divided solids should have greater solubilities than coarse crystals was assumed as early as 1813 (WOLLASTON, 1813). This phenomenon has long been described by the following modified Kelvin equation:

$$\frac{RT}{\overline{V}} \ln \frac{S}{S_0} = \frac{2\gamma}{r} \tag{1.1}$$

where S is the solubility (in mol · kg^{-1}) of fine grains with inscribed radius r in m, S_0 is the solubility of the bulk material. $\overline{V}$ is molecular volume in $m^3 \cdot mol^{-1}$, γ is the surface free energy in mJ · m^{-2}, R is the gas constant in nJ · mol^{-1} · K^{-1}, and T is the temperature in K. It indicates, as the grain dimensions decrease, that the solubility of the grain will increase exponentially relative to the bulk solubility. For a macroscopic grain, its size has no appreciable effect on solubility. Only if the radius of the particles being dissolved gets very small, that is, down to the nanoscale, the measured solubility may deviate from the macroscopic value dramatically (HOCHELLA, 2002).

However, the range of validity of the modified Kelvin equation has been the subject of scientific debate. Knapp (1922) suggested a correction to the modified Kelvin equation in order to include the effect of surface charge on solubility:

$$\frac{RT}{\overline{V}} \ln \frac{S}{S_0} = \frac{2\gamma}{r} - \frac{q^2}{8\pi K r^4} \tag{1.2}$$

where q is the electric charge, and K is the permittivity of the medium in which the particles are dispersed. Based on this, it can be seen that the exponential increase in solubility is not infinite as the particle size is reduced, but instead exhibits a maximum corresponding to a certain value of particle size r^* equal to

$$r^* = \sqrt[3]{\frac{q^2}{4\pi K \gamma}} \tag{1.3}$$

In dissolution studies of synthetic enamel-like hydroxyapatite, the critical size phenomenon for dissolution has been observed (Tang et al., 2003). The size change of etch pits on the surface of hydroxyapatite during dissolution was observed by AFM. When the etch pit size fell into a critical length scale, always at the nanoscale, dissolution rate decreased, eventually resulting in effective dissolution suppression (Tang et al., 2001). Based on this, Tang proposed a nano-dissolution model that is analogous to that of crystallization but with the participation of critical conditions involving dissolution pits rather than growth hillocks. This phenomenon cannot be observed in the dissolution of crystals much larger than the critical size, but only for nanosized sparingly soluble crystallites, such as hydroxyapatite, with normal size distributions of 10-10^3 nanometers (Tang et al., 2003). Therefore, this critical size effect could be embodied in the dissolution studies of nanocrystals.

So far very few experimental studies have been done to investigate size-dependent dissolution of nanomaterials. Meulenkamp (1998) has studied size-selective etching of ZnO nanoparticles using optical absorption spectroscopy. It was found that the dissolution rate was strongly dependent on average particle size. However, size distribution and the degree of polydispersity were not reported in this paper. These factors can greatly affect dissolution.

The fast dissolution of nanoparticles cannot just be attributed to the small particle size. Vogelsberger et al. (2008) investigated dissolution of γ-aluminium oxide, titanium dioxide, zirconium dioxide, and silicon dioxide nanoparticles in aqueous solution. The results showed a maximum dissolution rate at the beginning of the dissolution process, whereas over time, the dissolution rates were shown to decrease. Under some special conditions, the solubility maximum exceeded the long-time solubility of the nanoparticles by several orders of magnitude. Again, the size distribution and aggregation degree of nanoparticles were not well defined in this paper.

These previous studies actually reported the apparent results affected by many factors including particle size. Dissolution of mono-dispersed nanoparticles has never been reported before, until this study. Chapter 2 reports our work on the dissolution of mono-dispersed galena nanoparticles. Size-dependent dissolution of nanoparticles, as a frontier of environmental mineralogy, is still in its infancy.

Sulfide dissolution

Mechanisms of sulfide mineral dissolution are central to several Earth surface processes, such as acid mine drainage, contaminant desorption, and low-enthalpy water-rock interaction (e.g. Singer and Stumm, 1970; Nesbitt and Muir, 1994; Bostick et al., 2003). For example, dissolution reactions of galena (PbS) are responsible for a number of environmental problems, like Pb releases which result in the incorporation of toxic metals into surface water and groundwater. The release of heavy metals, such as Pb, may pose a threat to basic links in an ecosystem food web as well as to environmental niches and the ecosystem they comprise (SIEGEL, 2002). A detailed understanding of the dissolution of galena is an important key to more accurately predicting and monitoring the long-term mobility and bioavailability of Pb in natural settings. Moreover, a knowledge of the mobility potential of toxic metals under existing environmental conditions and how this might change as natural conditions change will assist remediation planning.

Galena (PbS) has a rocksalt or halite (NaCl) crystal structure. Basically, sulfur atoms are arranged in cubic close packing and all the octahedral interstitial positions are filled with lead atoms. Both lead and sulfur have an octahedral coordination (CN = 6). Galena has perfect cleavage along the three {100)} faces. As one of the most abundant and widely distributed sulfide minerals, galena is not only the most important lead ore mineral, but also associated with many other metal ore deposits. It commonly exists in mining sites and consequently becomes an obvious potential source of pollution from mine wastes. In addition, galena has attracted the interest of material scientists because of its technological importance, such as in IR detectors (e.g. Kumar et al., 2005). It is also an attractive substance for surface science experimentation and computer modeling studies, because it has a simple crystal structure and a perfect cleavage (Rosso and Vaughan, 2006).

Galena is insoluble in water at room temperature, but on exposure to acid it becomes more soluble. Lead sulfide is generally found under reducing environments, such as sludge digesters and anoxic aquatic sediments (MOREL et al., 1975). The overall non-oxidative dissolution reaction of galena in acid solution can be given by:

$$PbS + 2H^{+} = Pb^{2+} + H_2S(aq) \qquad (1.4)$$

The free energy change for this reaction is $\Delta G^0 = 42.44$ kJmol^{-1}(MAJIMA et al., 1981).The high apparent activation energies for non-oxidative dissolution of galena in acid solution suggest that the dissolution rate is surface-controlled (Awakura et al., 1980; Hsieh and Huang, 1989). Even after several decades of experimental investigations using bulk and surface analytical measurements (e.g. Awakura et al., 1980; Nunez et al., 1988; Zhang et al., 2004; De Giudici et al., 2005), and quantum mechanical calculations (Gerson and O'dea, 2003), a detailed knowledge of the dissolution mechanisms of lead sulfide is still incomplete. In particular, all the previous dissolution studies focus on bulk materials. The dissolution of sulfide nanoparticles has never been studied experimentally. As we mentioned above, solubility of minerals changes with particle size, and when the particle size goes down into the nanometer scale, the size effect on solubility may become detectable (LASAGA, 1998). Therefore, a systematic investigation of the effect of size on sulfide dissolution will have significant geochemical and environmental implications.

Dissertation outline

This dissertation presents my research efforts to understand the fate and behavior of nanoscale sulfide minerals in aqueous solution both from a microscopic and a macroscopic perspective. Influence of factors, such as particle size, morphology, and aggregation state, on the dissolution of nanoparticles has been investigated.

Chapter 2 is a paper published in *Geochimica Cosmochimica et Acta*, entitled "The non-oxidative dissolution of galena nanocrystals: Insights into mineral dissolution rates as a function of grain size, shape, and aggregation state". It describes the study of the acidic, non-oxidative dissolution of galena nanocrystals. The evolution of the size and shape of the nanocrystals before and after dissolution experiments has been studied in detail using transmission electron microscopy (TEM), and the dissolution rate was calculated directly according to the size shrinking of galena nanocrystals. This paper focuses on the microscopic observation of nanocrystal dissolution.

Chapter 3, entitled "Influence of size and aggregation on the non-oxidative dissolution of galena particles", is a paper in preparation. This work investigates the size and aggregation effect on nanocrystal dissolution. To assess the size effect, galena microcrystals (~ 3 μm) were synthesized and characterized, and the dissolution rate of

these microcrystals was compared with that of dispersed galena nanocrystals under similar conditions. To assess the aggregation effect, dissolution experiments of aggregated galena nanocrystals were conducted, and the result was compared with the rates of microcrystals and dispersed nanocrystals. The dissolution experiments were conducted using wet chemical method. It is the first work to compare the dissolution rates of dispersed and aggregated nanocrystals.

The Appendix 2. is a book chapter in *Environmental and Human Health Impacts of Nanotechnology* (Lead, J. R. and Smith, E., Editors), entitled "Size/shape-property relationships of non-carbonaceous inorganic nanoparticles: towards an understanding of environmental implications". This chapter reviews current knowledge about the size- and shape-dependent behaviour of non-carbonceous inorganic nanoparticles, and also discusses how this knowledge might be applied to understanding the fate and bioavailability of nanoparticles in environmental systems, as well as in assisting environmental remediation. The article is currently in press with Blackwell publishing.

References

Alivisatos, A. P., 1996. Perspectives on the physical chemistry of semiconductor nanocrystals. *Journal of Physical Chemistry B* **100**, 13226-13239.

Awakura, Y., Kamei, S., and Majima, H., 1980. A Kinetic-Study of Non-Oxidative Dissolution of Galena in Aqueous Acid-Solution. *Metall. Mater. Trans. B* **11**, 377-381.

Banfield, F. and Navrotsky, A., 2001. Nanoparticles in the environment. *Reviews in Mineralogy and geochemistry* **44**, 1-51.

Borm, P., Klaessig, F. C., Landry, T. D., Moudgil, B., Pauluhn, J., Thomas, K., Trottier, R., and Wood, S., 2006. Research strategies for safety evaluation of nanomaterials, Part V: Role of dissolution in biological fate and effects of nanoscale particles. *Toxicol Sci* **90**, 23-32.

Bostick, B. C., Fendorf, S., and A., M. B., 2003. Arsenite adsorption on galena (PbS) and sphalerite (ZnS). *Geochimica et Cosmochimica Acta* **67**, 895-907.

Christian, P., Von der Kammer, F., Baalousha, M., and Hofmann, T., 2008. Nanoparticles: structure, properties, preparation and behaviour in environmental media. *Ecotoxicology* **17**, 326-343.

De Giudici, G., Rossi, A., Fanfani, L., and Lattanzi, P., 2005. Mechanisms of galena dissolution in oxygen-saturated solutions: Evaluation of pH effect on apparent activation energies and mineral-water interface. *Geochim. Cosmochim. Acta* **69**, 2321-2331.

Gerson, A. R. and O'dea, A. R., 2003. A quantum chemical investigation of the oxidation and dissolution mechanisms of Galena. *Geochim. Cosmochim. Acta* **67**, 813-822.

Gilbert, B. and Banfield, J. F., 2005. Molecular-scale processes involving nanoparticlate minerals in Biogeochmical systems. *Reviews in Mineralogy and Geochemistry* **59**, 109-155.

Hochella, M. F., 2002. Nanoscience and technology the next revolution in the Earth sciences. *Earth and Planetary Science Letters* **203**, 593-605.

Hochella, M. F., Lower, S. K., Maurice, P. A., Penn, R. L., Sahai, N., Sparks, D. L., and Twining, B. S., 2008. Nanominerals, mineral nanoparticles, and Earth systems. *Science* **319**, 1631-1635.

Hsieh, Y. H. and Huang, C. P., 1989. The Dissolution of Pbs(S) in Dilute Aqueous-Solutions. *J Colloid Interf Sci* **131**, 537-549.

Knapp, L. F., 1922. The solubility of small particles and the stability of colloids. *Transactions of the Faraday Society* **17**, 457-465.

Kumar, S., Zishan, H. K., Khan, M. A. M., and Husain, M., 2005. Studies on thin films of lead chalcogenides. *Curr Appl Phys* **5**, 561-566.

Lasaga, A. C., 1990. Atomic Treatment of Mineral-Water Surface-Reactions. *Rev Mineral* **23**, 17-85.

Lasaga, A. C., 1998. *Kinetic theory in the earth sciences*. Princeton University Press, Princeton.

Lasaga, A. C. and Luttge, A., 2003. A model for crystal dissolution. *European Journal of Mineralogy* **15**, 603-615.

Liu, J., Aruguete, D. M., Jinschek, J. R., Rimstidt, J. D., and Hochella, M. F., Jr., 2008. The non-oxidative dissolution of galena nanocrystals: Insights into mineral

dissolution rates as a function of grain size, shape, and aggregation state *Geochim Cosmochim Ac* **72**, 5984 - 5996.

Madden, A. S. and Hochella, M. F., 2005. A test of geochemical reactivity as a function of mineral size: Manganese oxidation promoted by hematite nanoparticles. *Geochim. Cosmochim. Acta* **69**, 389-398.

Majima, H., Awakura, Y., and Misaki, N., 1981. A Kinetic-Study on Non-Oxidative Dissolution of Sphalerite in Aqueous Hydrochloric-Acid Solutions. *Metallurgical Transactions B-Process Metallurgy* **12**, 645-649.

Marabi, A., Mayor, G., Burbidge, A., Wallach, R., and Saguy, I. S., 2008. Assessing dissolution kinetics of powders by a single particle approach. *Chem Eng J* **139**, 118-127.

Meulenkamp, E. A., 1998. Size dependence of the dissolution of ZnO nanoparticles. *J. Phys. Chem. B* **102**, 7764-7769.

Morel, F. M. M., Westall, J. C., Omelia, C. R., and Morgan, J. J., 1975. Fate of Trace-Metals in Los-Angeles-County Wastewater Discharge. *Environmental Science & Technology* **9**, 756-761.

Murray, C. B., Kagan, C. R., and Bawendi, M. G., 2000. Synthesis and characterization of monodisperse nanocrystals and close-packed nanocrystal assemblies. *Annual Review of Materials Science* **30**, 545-610.

Nesbitt, H. W. and Muir, I. J., 1994. X-ray photoelectron spectroscopic study of a pristine pyrite surface reacted with water vapour and air. *Geochimica et Cosmochimica Acta* **58**, 4667-4679.

Nunez, C., Espiell, F., and Garciazayas, J., 1988. Kinetics of Nonoxidative Leaching of Galena in Perchloric, Hydrobromic, and Hydrochloric-Acid Solutions. *Metall Trans B* **19**, 541-546.

Rimstidt, J. D. and Newcomb, W. D., 1993. Measurement and Analysis of Rate Data - the Rate of Reaction of Ferric Iron with Pyrite. *Geochim Cosmochim Ac* **57**, 1919-1934.

Rosso, K. M. and Vaughan, D. J., 2006. Sulfide mineral surfaces. *Rev Mineral Geochem* **61**, 505-556.

Rufe, E. and Hochella, M. F., 1999. Quantitative assessment of reactive surface area of phlogopite during acid dissolution. *Science* **285**, 874-876.

Siegel, F. R., 2002. *Environmental geochemistry of potentially toxic metals*. Spinger.

Singer, P. C. and Stumm, W., 1970. Acid mine drainage: The rate limiting step. *Science* **167**, 1121-1123.

Tang, R. K., Nancollas, G. H., and Orme, C. A., 2001. Mechanism of dissolution of sparingly soluble electrolytes. *J. Am. Chem. Soc.* **123**, 5437-5443.

Tang, R. K., Orme, C. A., and Nancollas, G. H., 2003. A new understanding of demineralization: The dynamics of brushite dissolution. *J. Phys. Chem. B* **107**, 10653-10657.

Trindade, T., O'Brien, P., and Pickett, N. L., 2001. Nanocrystalline semiconductors: synthesis, properties, and prespectives. *Chemistry of Materials* **13**.

Vogelsberger, W., Schmidt, J., and Roelofs, F., 2008. Dissolution kinetics of oxidic nanoparticles: The observation of an unusual behaviour. *Colloid Surface A* **324**, 51-57.

Wigginton, N. S., Haus, K. L., and Hochella, M. F., 2007. Aquatic environmental nanoparticles. *J Environ Monitor* **9**, 1306-1316.

Wollaston, W. H., 1813. The Bakerian lecture: on the elementary particles of certain crystals. *Philosophical Transactions of the Royal Society of London* **103**, 51-63.

Zhang, S., Li, J. P., Wang, Y. R., and Hu, G. Q., 2004. Dissolution kinetics of galena in acid NaCl solutions at 25-75 degrees C. *Applied Geochemistry* **19**, 835-841.

Chapter 2 - The non-oxidative dissolution of galena nanocrystals: Insights into mineral dissolution rates as a function of grain size, shape, and aggregation state

Juan Liu[1], Deborah M. Aruguete[1], Joerg R. Jinschek[2], J. Donald Rimstidt[1], and Michael F. Hochella Jr.[1]

[1]Center for NanoBioEarth, Department of Geosciences, Virginia Tech, Blacksburg, VA 24061, USA
[2] FEI Europe Nanoport, Achtseweg Noord 5, Bldg. AAE-III-0-075, P.O. Box 80066, 5600 KA Eindhoven, The Netherlands

Reprinted from Geochimica et Cosmochimica Acta, vol. 72, 2008, 5984-5996, with permission from Elsevier.

Abstract

The acidic, non-oxidative dissolution of galena nanocrystals has been studied in detail using transmission electron microscopy (TEM) to follow the evolution of the size and shape of the nanocrystals before and after dissolution experiments, X-ray photoelectron spectroscopy (XPS) to follow particle chemistry, and dissolution rate analysis to compare dissolution rates between nanocrystalline and bulk galena. Dissolution characteristics were also studied as a function of nanocrystal access to bulk vs. confined solution due to the degree of proximity of next-nearest grains. Nearly monodisperse galena nanocyrstals with an average diameter of 14.4 nm were synthesized for this study, and samples were exposed to pH 3, deoxygenated HCl solutions for up to 3 hours at 25°C. Detailed XPS analysis showed the nanocrystals to be free of unwanted contamination, surface complexes, and oxidative artifacts, except for small amounts of lead-containing oxidation species in both pre- and post-dissolution samples which have been observed in fresh, natural bulk galena. Depending on the calculation methods used, galena nanocrystals, under the conditions of our experiments, dissolve at a surface area normalized rate of one to two orders of magnitude faster than bulk galena under similar conditions. We believe that this reflects the higher percentage of reactive surface area on nanocrystalline surfaces vs. surfaces on larger crystals. In addition, it was shown that

{111} and {110} faces dissolve faster than {100} faces on nanocrystals, rationalized by the average coordination number of ions on each of these faces. Finally, dissolution was greatly inhibited for galena nanocrystal surfaces that were closely adjacent (1-2 nm, or less) to other nanocyrstals, a direct indication of the properties of aqueous solutions and ion transport in extremely confined spaces and relevant to dissolution variations that have been suspected within aggregates.

2.1. INTRODUCTION

In the environment, mineral nanoparticles with dimensions ranging from 1-100 nm are abundant, formed by such common processes as mineral weathering or direct precipitation from solution (Banfield and Zhang, 2001 and references therein). These mineral nanoparticles may show variations as a function of their size and shape in the nanoscale regime, behaving quite differently from the same mineral in the micro- and macroscales. This has broadened our understanding of several local, regional, and global Earth processes (Hochella et al., 2008). Indeed, size-dependent reactivity of minerals has already been specifically demonstrated for geochemically important phenomena such as electron transfer and metal sorption (e.g. Madden and Hochella, 2005; Madden et al., 2006).

Another geochemically important process that can be affected by size is solubility. For example, fine quartz fragments were shown to have enhanced solubility (Stöber and Arnold, 1961). This phenomenon has been described by a modified version of the Kelvin equation (also known as the Gibbs-Thomson and as the Ostwald-Freundlich equation):

$$\frac{S}{S_0} = \exp[\frac{2\gamma \overline{V}}{RTr}] \tag{2.1}$$

where S is the solubility (in mol · kg^{-1}) of fine grains with inscribed radius r in m, and S_0 is the solubility of the bulk material. $\overline{V}$ is molecular volume in $m^3 \cdot mol^{-1}$, γ is the surface free energy in $mJ \cdot m^{-2}$, R is the gas constant in $nJ \cdot mol^{-1} \cdot K^{-1}$, and T is the temperature in K. According to this equation, as the grain size decreases, its solubility is expected to increase exponentially relative to the bulk solubility. Especially when particle size goes

down into the nanoscale, solubility is predicted to dramatically increase with particle size according to this relationship.

Nevertheless, recent studies have indicated that this phenomenon may not apply to all nanoparticulate minerals. For example, Tang et al. (2001) suggested the existence of a critical size, always at the nanoscale, for dissolution pit/step formation for sparingly soluble calcium phosphates. Because pit formation and growth are often important steps for dissolution, critical size effects should be taken into account in studies of size-dependent dissolution. Also, size effects on the dissolution rate of nanoscale metal oxides have been investigated (e.g. Meulenkamp, 1998; Roelofs and Vogelsberger, 2006), but these studies leave many unanswered questions due to uncertainty about the nature of the samples, their size uniformity, and/or their aggregation state, and few conclusions have been drawn.

This investigation concerns the acidic, non-oxidative dissolution of galena nanocrystals measured by following the evolution of their size, shape, and chemical composition. Galena is a significant source of lead in natural aqueous environments. An understanding of galena dissolution is highly desirable to accurately predict the long-term mobility and bioavailability of lead in many natural settings. To this end, the kinetics of galena dissolution in acidic solution has been extensively studied using wet-chemical experiments, surface analysis techniques, as well as quantum chemical calculations (e.g. Awakura et al., 1980; Gerson and O'dea, 2003). However, all previous studies have focused on bulk samples. As far as we are aware, no previous studies concerning the dissolution of galena nanocrystals have been reported. In this study, nearly monodisperse PbS nanocrystals were synthesized and thoroughly characterized. Galena nanocrystals deposited on transmission electron microscopy (TEM) grids were partially dissolved in deoxygenated hydrochloric acid solutions for different lengths of time. The dissolution rate was directly measured from TEM images of the nanocrystals. Chemical compositions of pre- and post-dissolution galena nanocrystals were analyzed by X-ray photoelectron spectroscopy (XPS). Morphology evolution of galena nanocrystals during dissolution was observed by high resolution TEM (HRTEM). The effects of size, morphology, and aggregation of nanocrystals on dissolution rate are discussed.

2.2. MATERIALS AND METHODS

2.2.1. Galena Synthesis and preparation for dissolution experiments

Galena nanocrystals were synthesized by the reaction of $PbCl_2$ and elemental sulfur in oleylamine (OLA, $CH_3(CH_2)_7CH{=}CH(CH_2)_8NH_2$) under inert atmosphere (Ar or N_2) (Joo et al., 2003). OLA is both a surfactant and a solvent. All reagents were purchased from Sigma-Aldrich and used without further purification. The procedure is as follows: 2 mmol $PbCl_2$ and 10 mL technical grade OLA were put into a 100 mL three-necked round-bottom flask equipped with a condenser, thermocouple, and septum port for reagent injection. This mixture was magnetically stirred and heated at 120 °C for 15-30 minutes. At the same time, 1.7 mmol sulfur were dissolved in 5 mL OLA at 80 °C for about 15 minutes. After $PbCl_2$ was totally dissolved in OLA, the sulfur-OLA solution was quickly injected into the $PbCl_2$-OLA solution using a syringe. The temperature was increased to 220 °C and maintained for 2.5 hours. The reaction was ended by rapidly cooling the reaction mixture to ≤170 °C by blowing air on the outside of flask and then adding hexanes. The resulting solution was centrifuged to remove excess $PbCl_2$. Isopropyl alcohol was added to the supernatant dropwise until it grew turbid, indicating that the nanocrystals were flocculated. The flocculated nanocrystals were separated from the supernatant by centrifugation and then dispersed in fresh hexanes (Cademartiri et al., 2006). Nanocrystal solutions were stored in the dark at 4 °C.

Synthetic galena nanocrystals are totally or partially coated by OLA ligands, which prevent agglomeration in nonpolar solvents. These capping groups may block active surface sites for dissolution; therefore we removed them before any dissolution experiments. The excess OLA molecules in solution, which were not bound to nanocrystal surfaces, were washed away by centrifuging the nanocrystal solutions, removing the hexanes supernatant containing unbound OLA, and re-dispersing them in fresh hexanes. This process was repeated 3-4 times. TEM samples were prepared by dipping a carbon-coated 400-mesh copper TEM grid into the washed nanocrystal solution. The grid was allowed to dry in air. To remove any residual OLA, the grid was further

cleaned by repeatedly depositing drops of isopropyl alcohol onto the grid and wicking the alcohol away with filter paper.

2.2.2. Dissolution Experiments

Nanocrystal samples for dissolution experiments were prepared as above, with gold TEM grids. The grids were then secured onto a PTFE grid holder. Dissolution experiments were performed in a glass reactor (~750 mL capacity) under constant mechanical stirring at 25 °C. 500 mL of hydrochloric acid solution (pH 3) were added to the chamber and purged with nitrogen for 30 minutes to remove dissolved O_2. The chamber was quickly opened to immerse the nanocrystals attached to the TEM grids in the acid, but otherwise was sealed. Nitrogen purging was maintained throughout the experiment and the pH was monitored constantly with a pH meter. When the desired dissolution time was reached (in this study, between 1 and 3 hr), the grids were removed from the acid and dried with filter paper which only took a couple of minutes. Grids were stored overnight in a desiccator prior to TEM analysis. XPS measurements (see below) showed that this storage did not result in significant (detectable) galena surface oxidation.

2.2.3. Characterization of Galena Nanocrystals

2.2.3.1. X-ray diffraction (XRD)

The crystal phase of the synthetic nanocrystals was identified by a Pan Analytical X'PERT-Pro X-ray powder diffractometer, equipped with a Co Kα source. Samples were mounted on a zero-background sample holder. Diffraction patterns were collected in the 2θ range of 20-100° using a step size of 0.067°.

2.2.3.2. X-ray Photoelectron Spectroscopy (XPS)

All XPS measurements were carried out with a Perkin-Elmer 5400 X-ray photoelectron spectrometer (Physical Electronic Industries, Inc.) using an Al Kα X-ray

source and two-channel collector. The pass energy for survey scans was 89.45 eV, and for narrow scans it was 17.9 eV. Data was analyzed using AugerScan 3.12 (RBD Enterprises Inc.). XPS samples of nanocrystals were prepared by evaporating concentrated nanocrystal solutions onto silicon wafers. An XPS sample of natural bulk galena was prepared by grinding fragments in an agate mortar and pestle. A minute amount of gold was deposited onto all samples, and all spectra were calibrated using the position of the Au $4f_{7/2}$ (binding energy = 84.0 eV) line. The sample and substrate were sufficiently conductive so that charge compensation was not needed, and sulfur volatilization or any other sample instability under the X-ray beam was not observed. Spectral peaks were resolved into their components after non-linear background subtraction. Curve-fitting parameters, such as peak widths, were determined from the spectra of the natural galena, and were kept constant. The atomic ratios were calculated according to the formula:

$$\text{Atomic ratio of A to B} = (I_A/F_A)/(I_B/F_B) \quad (2.2)$$

where I_A and I_B are the peak area of the photoemission lines of element A and B, respectively. F_A and F_B are the sensitivity factors for element A and B, which are constant for a given spectrometer. Therefore, the ratio of peak areas I_A:I_B is proportional to the relative atomic ratios.

2.2.3.3. Transmission Electron Microscopy (TEM)

The size and shape of nanocrystals were observed with an FEI Titan 300 Transmission Electron Microscope operated in both bright-field mode and high-resolution (HRTEM) mode at 200 kV. To quantitatively describe the shape and size distribution of nanocrystals, bright-field TEM images were taken from various regions of each experiment sample (performed in duplicate). For each sample, at least 100 nanocrystals were randomly selected and analyzed. The size and shape changes of nanocrystals could be measured with good precision due to the strong image contrast between the nanocrystals and background (carbon film). These images were analyzed using the image processing and analysis program, ImageJ (Rasband, 1997-2007). Particle dimensions (projected area) and shape parameters (roundness and aspect ratio) were quantified with

the 'Shape descriptors' plugin (Bright, 2004). To avoid measurement artifacts, the outlines of each particle defined by ImageJ were compared to the actual particle boundaries in the original image. If these did not match each other for a given particle, that particle was excluded from the data. Particle size, *i.e.* the projected area diameter (*d*), defined as the diameter of a circle having the same area as the particles, is given by:

$$d = 2(A/\pi)^{1/2} \tag{2.3}$$

where *A* is the mean projected area of particles (Luerkens, 1991).

2. 3. RESULTS AND DISCUSSION

2.3.1. Pre-dissolution galena nanocrystals

2.3.1.1. XRD crystal structure and particle size

Powder X-ray diffraction (XRD) patterns of the nanocrystals (Fig. 2.1) revealed that only galena was present. The average crystallite diameter, d, was estimated from the broadening of the XRD peak widths by the Scherrer formula:

$$d = \frac{K\lambda}{\beta \cos\theta} \tag{2.4}$$

where λ is the wavelength of the radiation, β is the integral width of the Bragg reflection at 2θ, and *K* is the Scherrer constant which depends on factors such as the geometry of the crystallites (Langford and Wilson, 1978). Since TEM images (Fig. 2.2a) show that PbS nanocrystals exhibit nearly cubic shape, a *K* of 0.94 was used (Scherrer, 1918). Using Eqn. 2.4, the average particle diameter of our nanocrystals was calculated to be about 16 nm. The average diameter determined from TEM images is 14.4 ± 1 nm, in good agreement with the XRD result.

2.3.1.2. Chemical composition of nanocrystals

The information depth of the XPS method (essentially the depth of analysis) is about three times the inelastic mean free path (λ) of the photoelectrons being used in the

analysis. The value of λ is typically 2.5-3 nm for photoelectrons used to analyze PbS using AlKα excitation (Tanuma et al., 1991; Laajalehto et al., 1997). Therefore, XPS provides information from nearly the whole nanocrystal. The survey scans (Fig. 2.3) show not only Pb and S, but also C and O. Generally, the C and O signals can be assigned to surface contaminants and oxidation species, resulting from the exposure to ambient air or storage solution. However, compared to the natural galena (Fig. 2.3b), the C signal of the unwashed sample (Fig. 2.3a) is much stronger. The relative atomic ratio, represented by I_C: I_{Pb} in Table 1, of the unwashed sample is much larger than this ratio for natural galena. This indicates that the C signal on the unwashed sample is due to more than normal adventitious hydrocarbon contamination. In the detailed C1s spectra (Fig. 2.4), the components at 284.5 eV and at about 286.6 eV are generally due to hydrocarbon and oxidized hydrocarbon contamination, respectively. However, the peak at 286.6 eV in the unwashed sample has a very high intensity; it may be C-N species from OLA (Moulder et al., 1995). The washed sample has similar C 1s spectra and I_C: I_{Pb} ratios as those for natural galena. Hence, the washing procedure is necessary for obtaining 'clean' surfaces on galena nanocrystals, and also required for dissolution experiments.

The Pb 4f spectra (Fig. 2.5) of galena nanocrystals are similar to that of natural galena. All Pb 4f doublet spectra are composed of two peaks (i.e. $Pb4f_{5/2}$ and $Pb4f_{7/2}$). In $Pb4f_{7/2}$ spectra, the strong emission at 137.3 - 137.5 eV (Table 1) can be assigned to PbS. The other component at a binding energy near 138.5 eV can be attributed to lead-containing oxidation species which have been observed on both fresh and oxidized galena surfaces (Laajalehto et al., 1993; De Giudici et al., 2005). It is worth noting that the intensity of this oxidation species in post-dissolution nanocrystals did not increase noticeably. The Pb 4f signal assigned to $PbCl_2$ at 140.0 eV (De Giudici et al., 2005) is not detected in all samples. The absence of Cl photoemission lines supports this result. Therefore, no detectable $PbCl_2$ or other Pb-containing products are on the surface of the post-dissolution nanocrystals.

In the S 2p region of all samples, there is the S 2p spin orbit split doublet with peaks near 160.8 eV and 162.0 eV, which can be attributed to PbS (Fig. 2.6). It is possible that there would be some metastable species of S present, such as polysulphides, thio-sulphates, and/or sulphites on the post-dissolution galena surface (De Giudici et al.,

2005). However, in all samples there were no apparent S peaks at higher binding energies (164.0 - 170.0 eV) corresponding to these species. It is difficult to identify these species from XPS spectra because these phases could be unstable and present in very small amounts. It is known that the continuous low-intensity peaks formed by these phases are not easy to separate from a noisy background (Becker and Hochella, 1996). Finally, the presence of sulfate can be ruled out in all samples because there is no signal at 169.5 eV, and the lack of any obvious peak at 164.0 eV suggests that there cannot be much elemental sulfur forming on the post-dissolution samples. The peak at the lowest binding energy value in Fig. 2.6 was assigned to the Pb 5s signal (De Giudici et al., 2005).

The O1s signal (in Fig. 2.7) changed after dissolution. For the natural galena, there was only one component at 531.0 eV, probably associated with PbO (Fornasiero et al., 1994 and references therein). Although the binding energies of O 1s in $PbSO_4$ and $PbCO_3$ are also in this range, they could be ruled out due to the absence of corresponding S and C peaks. On the pre-dissolution nanocrystals, besides the component at 531.0 eV, an additional component at 532.2 eV was present. This peak can be assigned to Pb-OH bonds in oxyhydrated or hydrated species (De Giudici et al., 2005), which can be due to the washing procedure. In the post-dissolution sample, only the component at 532.2 eV is present. A potential explanation for this change is that PbO is dissolved away in the acid solution. Moreover, the ratios of I_o:I_{Pb} increased after dissolution. However, it can be seen from the Pb4f that the percentage of lead-containing oxidation species at 138.5 eV do not increase in the post-dissolution sample. Therefore, the component at 532.0 eV cannot totally be assigned to Pb-OH bonds. Absorbed H_2O may also contribute to it. The XPS results of post-dissolution nanocrystals do not show the formation of any surface complex.

2.3.1.3. Pre-dissolution crystal structure and morphology observed by HRTEM

The three-dimensional faceting morphology of galena nanocrystals was analyzed using HRTEM. Fig. 2.8a and 8c are representative HRTEM images of a PbS nanocrystal viewed along the <100> and <110> orientations, respectively. The <100> projection (Fig. 2.8a) shows a set of large {100} faces forming a square and a set of relatively small {110} faces at the corners of the square. In the <110> projection (Fig. 2.8c), besides {100} and

{110} faces, small {111} faces are observed. By integrating the projected images from these two orientations, we constructed a three-dimensional model of the galena nanocrystals, as schematically shown in Fig. 2.9b. In brief, PbS nanocrystals are terminated by six primary {100} faces, eight small {111} faces, and twelve small {110} faces, forming a cuboctahedral shape. A similar truncated cubic shape, exhibiting six primary {100} faces and eight minor {111} faces, has been reported for synthetic galena nanocrystals (Lee et al., 2002) (Although not reported by Lee et al. (2002), {110} faces are observed in their images). It is difficult to observe the higher-index crystalline faces by HRTEM, because the spacings of lattice fringes on these faces are too small to be resolved.

2.3.2. Shape and Size Evolution of Post-dissolution PbS Nanocrystals

2.3.2.1. Shape evolution

To quantitatively describe particle shape, ImageJ was used to measure a set of shape descriptors, including roundness and aspect ratio, described in equations (2.5) and (2.6) (Russ, 2002). These descriptors are dimensionless and do not depend upon particle size.

$$Roundness = \frac{4 \cdot Area}{\pi \cdot Maximum \quad Diameter^2} \tag{2.5}$$

$$Aspect \quad Ratio = \frac{Maximum \quad Diameter}{Minimum \quad Diameter} \tag{2.6}$$

These two independent shape descriptors characterize different aspects of particle morphology. Roundness is largely sensitive to the sharpness of angular protrusions from the particle, giving low values for rough particles and higher values for smooth ones (Bowman et al., 2001). Aspect ratio varies with overall elongation, but not with surface roughness. The similar values of shape descriptors for the unwashed and washed nanocrystals indicate washing did not change the particle morphology significantly (data not shown), although the TEM images (Fig. 2.2a and 2.2b) suggest that some of the washed particles are more rounded. Fig. 2.10 shows the mean shape descriptors of PbS nanocrystals before and after dissolution measured from TEM images. It can be seen

from fig. 2.10 that roundness decreases and aspect ratio increases with the progress of dissolution. This means that there is increased surface roughness or angularity and anisotropic etching on post-dissolution nanocrystals. This change can directly be seen from the typical bright-field TEM images of post-dissolution particles (Fig. 2.2c and 2.2d). The morphology change of nanocrystals in dissolution will be discussed further, together with HRTEM results, in section 2.3.2.3.

2.3.2.2. Statistical analysis of size evolution

Given the anisotropic shapes of the post-dissolution nanocrystals, it is more suitable to use the projected area, rather than the length along a specific orientation, to describe the size evolution. Also, PbS dissolution at pH 3 is a surface-controlled reaction (Awakura et al., 1980), so the dissolution rate is directly related to the rate of volume change. In this work, the dissolution reaction is far from equilibrium, so the dissolution rate, *R*, should be nearly constant at constant pH and temperature (Lasaga, 1998). Therefore, the particle lifetime model can be used to calculate the diameter of dissolving particles (d) at any time (t) by the following equation (Lasaga, 1998):

$$d = d_0 - 2R \cdot V_m \cdot (t - t_0) \tag{2.7}$$

which can be rearranged to find the dissolution rate, R (mol · m^{-2} · s^{-1}),

$$R = \frac{1}{2V_m}\left(\frac{\Delta d}{\Delta t}\right) \tag{2.8}$$

where V_m is the molar volume of the mineral (cm^3 · mol^{-1}). d_0 is the original diameter of the particles. The diameter, d, of each PbS nanocrystal was calculated from its projected area according to Eqn. 2.3. Fig. 2.11 shows the mean diameter of PbS nanocrystals with dissolution time. ($\Delta d/\Delta t$) was obtained by linear regression of the data in Fig. 2.11. The average dissolution rate of PbS nanocrystals along all crystallographic directions calculated by Eqn. 2.8 is 4.4 x 10^{-9} mol · m^{-2} · s^{-1}.

This rate is faster than what has been calculated from comparable bulk galena data. For example, Acero et al. (2007) studied the steady-state dissolution rates of galena powder (between 10 and 100 μm) in acidic solution using flow-through experiments. They observed that the galena dissolution rate is independent of dissolved oxygen

concentrations when the pH is below 2. Therefore, the rate law for pH < 2 may reflect the rate of non-oxidative dissolution. The dissolution rate is calculated to be 9.5 x 10^{-12} mol · m^{-2} · s^{-1} at pH = 3 and 25°C according to this rate law. This rate was based on the specific surface area determined by BET (Brunauer-Emmett-Teller) method. However, in our study, the surface area was calculated by a geometric method. According to the particle sizes reported in Acero et al.(2007), the geometric surface area, A_{geo}, is calculated to be 1/9 times the BET specific surface area, A_{BET} (see Appendix A). Consequently, the rate normalized by geometric surface area, R_{geo}, should be 9 times the rate by BET surface area, R_{BET}. Therefore, R_{geo} is 8.6 x 10^{-11} mol · m^{-2} · s^{-1}. It is much slower than the rate of galena nanocrystals measured in this study. The rate law for pH > 2 in Acero et al. (2007) includes the term, $a_{O_2(aq)}^{0.30\pm0.03}$, reflecting the effect of the dissolved oxygen (DO). R_{BET}, calculated according to this rate law, is 2.7 x 10^{-10} mol · m^{-2} · s^{-1} ($P_{O_2} = 0.21$ atm), and consequently R_{geo} is 2.4 x 10^{-9} mol · m^{-2} · s^{-1}. The rate, R_{geo}, seems similar to the rate of galena nanocrystals. However, it can be seen from the rate law for pH>2 that the dissolved oxygen accelerates the dissolution reaction. The actual rate of the non-oxidative dissolution should be slower than 2.4 x 10^{-9} mol · m^{-2} · s^{-1}, and also slower than the rate of galena nanocrystals. Another dissolution study of galena (150-180 μm) in the presence of 1 M NaCl solutions was reported by Zhang et al. (2004). Although NaCl solutions would accelerate the dissolution, the calculated rate (R_{geo}), 2.2 x 10^{-10} mol · m^{-2} · s^{-1}, is still slower than the rate in this work.

This difference in dissolution rate may be attributed to the small size of nanocrystals. As predicted by the modified Kelvin equation (Eqn. 2.1), nanocrystals may have much higher solubility than their bulk counterpart. Although, in this work, it is the surface area normalized rates, not solubilites, that are measured and compared, the Kelvin equation indicate that the dissolution is more thermodynamically favored on nanocrystals relative to bulk materials. Moreover, between nanoscaled and bulk minerals with the same total surface area, nanocrystals have a larger fraction of the atoms at edges and corners than the bulk ones. Atoms at these sites are more active in the dissolution than ones on flat surfaces. Therefore, the proportion of reactive surface area per volume on nanocrystals is actually larger than that on the bulk material. However, it is impossible to use the active surface area to normalize the dissolution rate, because this area is difficult

to precisely quantify and also varies during the dissolution process. Further, ground natural galena powders commonly exhibit {100} faces because galena easily cleaves on this plane, but the synthetic galena nanocrystals exhibit {111} and {110} faces besides {100} faces. HRTEM images (see section 3.2.3.1) showed that {111} and {110} faces dissolved faster than {100} faces (see below). Therefore, the different morphology may also contribute to the faster dissolution of nanocrystals.

2.3.2.3. HRTEM observations of nanocrystal morphology evolution

HRTEM was used to study the morphology evolution of nanocrystals as dissolution progressed. Differences were observed between the morphology evolutions of isolated nanocrystals versus nanocrystals adjacent to other nanocrystals in clusters.

Isolated nanocrystals. Relative dissolution rates of different crystal faces were examined with HRTEM and found to vary. In Fig. 2.8a and 2.8b, representative images of isolated PbS nanocrystals along the <100> zone axis before and after three hours of dissolution are shown. Previous to dissolution, the {100} faces are larger than the {110} faces, giving the particle a nearly square projection. After dissolution, the area of the {110} faces increases compared to {100} faces.

It is well-known that the area increase for a given crystal face during dissolution is proportional to its dissolution rate. Hence, qualitatively it can be seen in Fig. 2.8b that the dissolution rate for {110} faces is greater than that for the {100} faces. This phenomenon can be quantitatively measured as well by measuring the ratio of the particle length along the <100> orientation and the <110> orientation, $R = d_{100} / d_{110}$ (as shown in Fig. 2.9a). A higher dissolution rate for the {110} faces means that R should increase after dissolution. Fig. 2.9a shows plots of the ratios measured on nanocrystals before dissolution and after 2-hr dissolution, respectively. The mean ratio of pre-dissolution nanocrystals is 0.91, but that of 2-hr dissolution nanocrystals is 0.94. A t-test for comparing the means of these two samples yields a probability of ~ 0.01 that means there is a 99% chance of the means being significantly different. The increase in R demonstrates that the {110} faces dissolve more quickly than the {100} faces.

Varying dissolution rates could also be observed for the {111} faces versus the {110} and {100} faces. Representative HRTEM images of pre- and post-dissolution particles viewed along the <110> zone axis are shown in Fig. 2.8c and d. It can be seen from the images that {111} faces become larger than other faces after dissolution. However, this observation cannot be confirmed statistically, because there are not many nanocrystals aligned along the <110> orientation ({111} faces cannot be imaged in the <100> orientation). Therefore, the three-dimensional morphology change of PbS nanocrystals in dissolution can be schematically shown as Fig. 2.9b.

This orientation-dependent dissolution rate may be explained by the atomic structures of these surfaces. Each Pb^{2+} ion is surrounded by five nearest neighbor sulfur ions on {100} faces, four on {110} faces, and three on {111} faces. The rate of removal of an atom with n bonds on the surface (k_n^-) depends on the combined probability of all n bonds breaking as shown in the following equation (Lasaga and Luttge, 2004):

$$k_n^- = \nu e^{-n\Phi/\kappa T} \tag{2.9}$$

where ν is the frequency (pre-exponential factor) of the breaking of the bonds (s^{-1}); Φ is the energy for breaking one bond; κ is the Boltzmann constant, and T is temperature in Kelvin. The coordination number of ions on {100} faces is more than that on {110} and {111} faces, which may result in the relatively slow dissolution rate on {100} faces. It has been recently argued, based on thermodynamic arguments and experimental observations, that for small crystals such dissolution rate differences will have a significant impact on the fundamental characteristics of mineral solubility (Fan et al., 2006).

Furthermore, crystal defects become apparent on some post-dissolution nanocrystals. In the HRTEM images of pre-dissolution nanocrystals, crystal defects are rarely observed. However, steps, as shown in Fig. 2.12, are present on some post-dissolution nanocrystals. These steps may originate and propagate-from the particle edges or corners. Dissolution preferentially occurs at lattice defects, and proceeds along the defects where strain is concentrated. Therefore, crystal defects may become “exposed” as dissolution progresses. The small values of roundness on post-dissolution nanocrystals in

Fig. 2.10 statistically show the increase of surface irregularity and roughness. This is in agreement with the HRTEM images.

Particle clusters. When a drop of the nanocrystal solution dries on a TEM grid, rapid evaporation may segregate particles near the liquid-air interface, and an attractive interaction between the particles and liquid-air interfaces may also localize them on the interface (Bigioni et al., 2006). Consequently, particle clusters can be generated on the TEM grid. As shown in Fig. 2.13a, PbS nanocrystals are vclose to each other. The interparticle spacing between adjacent PbS nanocrystals is as small as 1 to 2 nm. This kind of nano-scaled interparticle spacing is easily formed in nanocrystal clusters because of the inherent size of these particles and their crystal shapes. The confined space may affect the dissolution of nanocrystals. For example, Fig. 2.13b shows a post-dissolution nanocrystal (P_1) which is adjacent to two particles (P_2 and P_3). The spacing between P_1 and P_3 is approximately 2 - 3 nm, and that between P_1 and P_2 is approximately 1 nm or less. The partly dissolved nanocrystal, P_1, presents an asymmetric shape. The {110} faces on its left side of the crystal in the image are larger than {110} faces on the right side. It can be seen that the faces on the left side are open to the bulk solution, but the faces on the right side are close to other particles. The slower dissolution rate on faces closely adjacent to other particles may be due to the abnormal properties of aqueous solution in the confined space. A variety of studies have suggested or shown that the liquid confined in nanospace exhibit properties different from the bulk, such as increased viscosity (e.g.Derjaguin and Churaev, 1986; Hochella and Banfield, 1995; Hibara et al., 2002; Tsukahara et al., 2007). The diffusion of acidic solution into the nanospaces between two adjacent nanocrystals may be retarded or inhibited. As a result, the faces exposed to the confined space may dissolve more slowly than ones exposed to bulk solution. The asymmetric dissolution is not unusual on post-dissolution PbS nanocrystals. This may contribute to the increase of mean aspect ratio on the post-dissolution nanocrystals. Furthermore, this dissolution inhibition caused by nanospace between nanocrystals suggests that aggregation may affect the overall dissolution rate. Nevertheless, the measured dissolution rate of galena nanocrystals is faster than that of bulk galena.

When the inter-particle spacing decreases further, approaching zero, oriented attachment happens between adjacent nanocrystals. Fig. 2.14a shows two attached, pre-dissolution nanocrystals. The Fast Fourier Transform (FFT) patterns of the upper particle (Fig. 2.14b) and the lower particle (Fig. 2.14c) are similar, showing that the two particles are in almost the same orientation. Moreover, at the interface between these two nanocrystals, the lattice fringes are continuous without obvious defects or dimples. This has been examined by changing defocus values during HRTEM imaging. Therefore, the nanocrystals in Fig. 2.14a could have been formed by oriented attachment. The oriented attachment may have been generated during nanocrystal washing, or during the deposition of the nanocrystals on TEM grids. Chemical bonds are formed at the interface between attached particles, in order to reduce the total energy by eliminating the solid-liquid interface (Penn and Banfield, 1998).

Fig. 2.14d shows a group of attached nanocrystals after dissolution. The high magnification images of the interfaces between the attached nanocrystals (Fig. 2.14e and 2.14f) show a continuous crystal lattice pattern without obvious crystal defects. In Fig. 2.14d, the nanocrystals, especially the middle and the left ones, are elongated relative to the pre-dissolution nanocrystals as in Fig. 2.14a. This uneven etching may result from the faster etching of crystal faces exposed to solution, as opposed to the faces attached to other nanocrystals. The high density of corners and edges at the interfaces where nanocrystals attach to each other may also be a source of active sites for dissolution, consequently flattening faces parallel to the axis along which the nanocrystals are attached. At the actual attachment points between nanocrystals, no sign of dissolution is readily apparent.

2.4. IMPLICATIONS

The morphology evolution of PbS nanocrystals in dissolution was observed by HRTEM. Differences in etching rates for crystal faces matched what might be expected from our knowledge of bulk crystals. Faces with lower coordination numbers, namely the {110} and {111} faces, were etched more quickly than the {100} faces ({111} data

not shown). The development of steps on nanocrystals in dissolution was also observed by HRTEM.

In this study, dissolution processes in confined, nanometer spaces between minerals is directly observed. HRTEM images reveal that, on the same PbS nanocrystal, the faces adjacent to other nanocrystals dissolved much slower than the faces exposed to the bulk solution. This difference in dissolution rates may be related to the altered properties and/or movement of aqueous solution in confined spaces. Such results may be helpful in understanding weathering reactions happening in confined spaces, for example, in the inter-granular space between fine grains or in fracture systems within individual grains.

It was found that PbS nanocrystals dissolve faster than bulk galena under comparable experimental conditions in deoxygenated hydrochloric acid solutions (pH = 3) at room temperature. This result agrees with the prediction (Eqn. 2.1) that nanocrystals are more soluble than larger crystals. This behavior may be due to their small size and higher reactive surface area per volume. Also, it may be partly attributed to the presence of more active crystal faces. The measurement method in this study could be applicable to most monodisperse nanocrystals and effectively reduces the effect of aggregation in dissolution experiments. However, this method is not applicable to nanocrystals that have a broad size/shape distribution or strong bonds between surfactant molecules and their surfaces.

Nanominerals and mineral nanoparticles are ubiquitous throughout nature. The transportation and release of toxic heavy metals from nanominerals in Earth's surface environment is an important factor in the well-being of the environment (Hochella et al., 2008). Solubility, or dissolution rate, of nano-scaled minerals is a critical property for predicting the fate of minerals and dissolved species in the environment. This study shows that PbS nanocrystals may dissolve significantly faster than their bulk counterparts. PbS nanocrystals should not survive as long as bulk galena in the environment, which has implications for their transport and bioavailability.

Acknowledgements. Grants from the U.S. Department of Energy (DE-FG02-06ER15786) and the Institute for Critical Technology and Applied Science at Virginia Tech provided major financial support for this study. We thank Dr. B. Shen for helpful discussions.

APPENDIX A: CALCULATION OF GEOMETRIC SURFACE AREA (A_{geo}) AND A_{geo} NORMALIZED DISSOLUTION RATE (R_{geo})

The geometric specific surface area, A_{geo}, was calculated by assuming that particles are smooth spheres with an effective spherical diameter (d_e) and the density of galena (ρ)

$$A_{geo} = \frac{\pi (d_e)^2}{(\pi/6)(d_e)^3 \rho} = \frac{6}{d_e \rho} \quad \text{(A. 1)}$$

Equation A1 also holds if the particles are smooth cubes (Tester et al., 1994). The effective spherical diameter (d_e) was calculated based on the maximum (d_{max}) and minimum (d_{min}) particle sizes

$$d_e = \frac{d_{max} - d_{min}}{\ln(\frac{d_{max}}{d_{min}})} \quad \text{(A. 2)}$$

In the study of Acero et al. (2007), particle sizes are between 10 and 100 μm. The effective diameter calculated by Eqn. A. 2 is 39.1 μm. Consequently, A_{geo} is 0.02 $m^2 \cdot g^{-1}$, according to Eqn. A. 1. The specific surface area determined by the BET method, A_{BET}, was 0.18 $m^2 \cdot g^{-1}$. Therefore, R_{geo} = 1/9 R_{BET}. Similarly, in the study of Zhang et al. (2004), the sizes of galena particles are 150-180 μm. The ratio of A_{BET} to A_{geo} is 0.78. R_{BET} calculated from the rate law in the paper is 2.9 x 10^{-10} mol $\cdot$ m^{-2} $\cdot$ s^{-1}. Therefore, R_{geo} is 2.2 x 10^{-10} mol $\cdot$ m^{-2} $\cdot$ s^{-1}.

Table 2.1. Binding energies and peak area ratios (I_C:I_{Pb} and I_O:I_{Pb}) of various XPS peaks on natural and synthetic galena samples

Galena sample	C 1s	O 1s	Pb $4f_{7/2}$	$I_C : I_{Pb}$	$I_O : I_{Pb}$
Natural	284.5	531.0	137.3	0.076	0.094
	286.3		138.4		
Unwashed	284.5	531.8	137.3	1.137	0.451
	286.0	533.3	138.2		
			139.1		
Washed	284.5	531.0	137.5	0.032	0.030
	286.7	532.3	138.5		
Post-dissolution	284.5	532.0	137.5	0.115	0.146
	286.6		138.6		

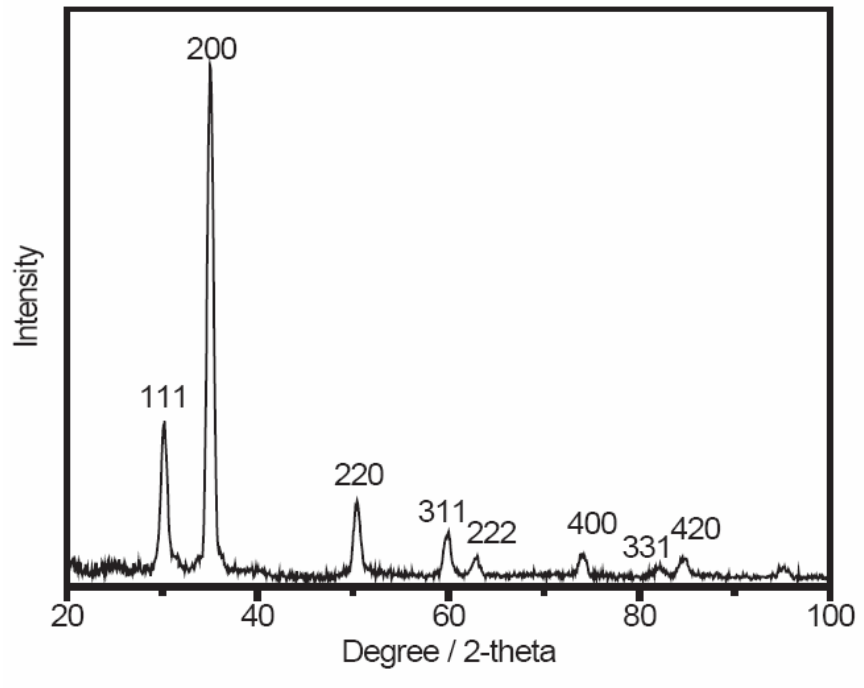

Figure 2.1. X-ray diffraction pattern of PbS nanocrystals

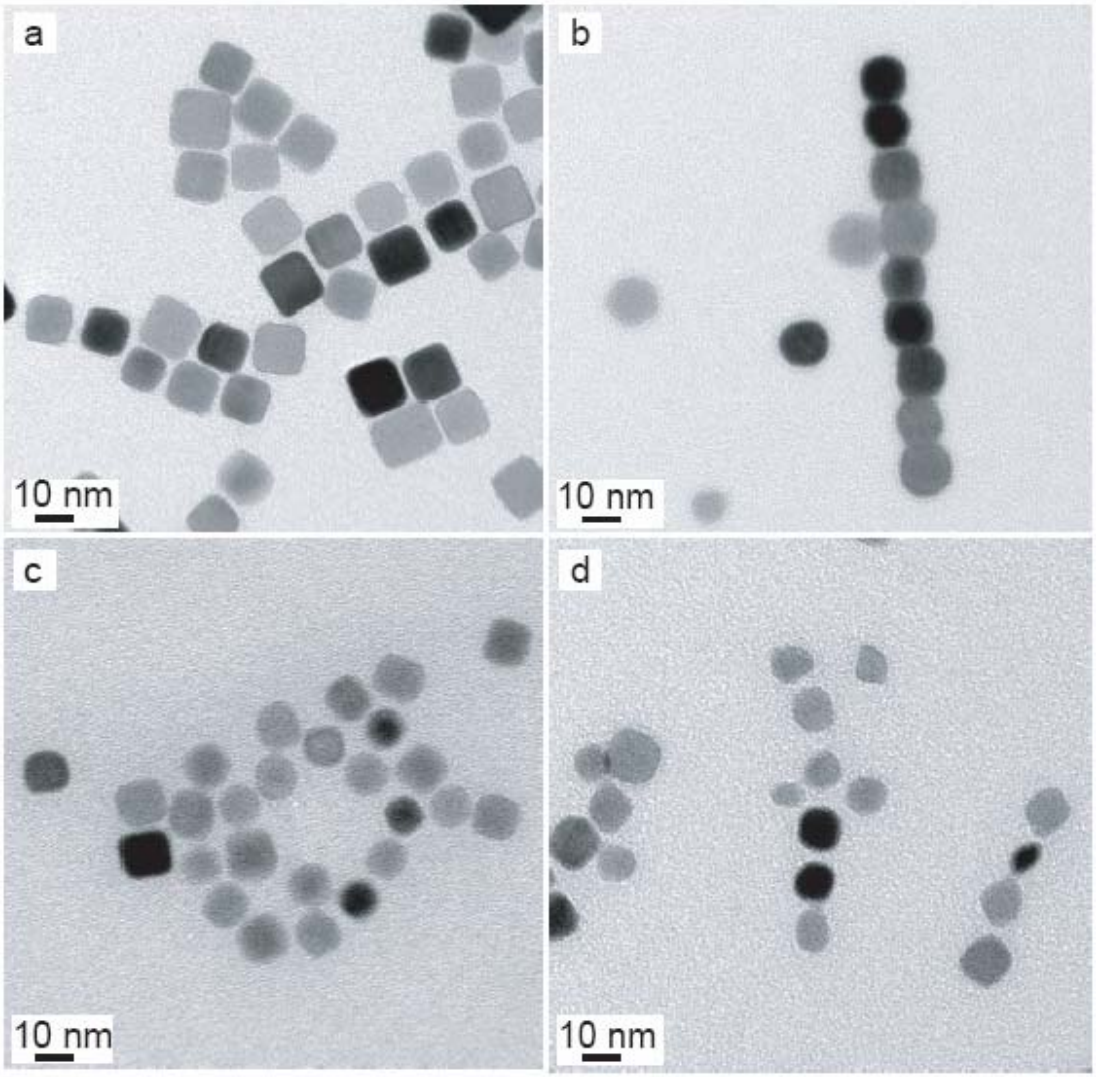

Figure 2.2. Bright field TEM images of PbS nanocrystals (a) before wash, (b) after wash, (c) after wash and 2-hour-dissolution, as well as (d) after wash and 3-hour-dissolution. Scale bar is 10 nm.

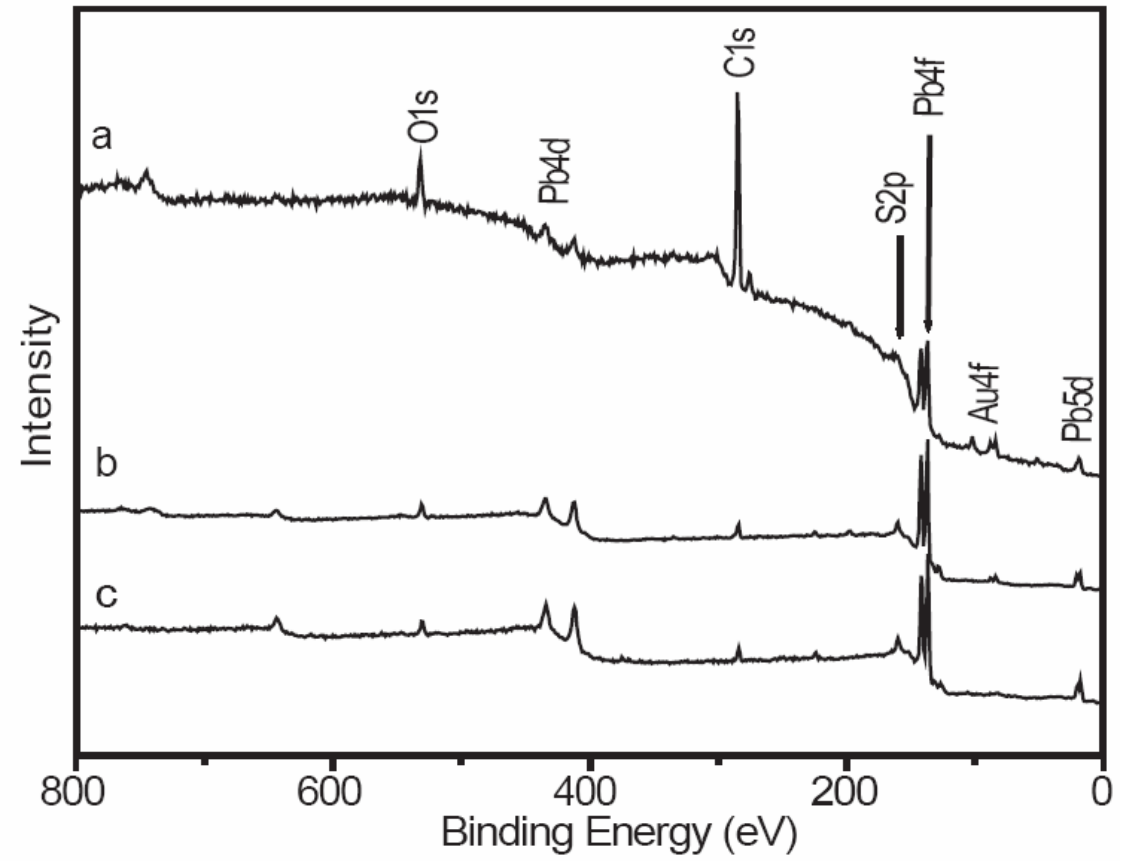

Figure 2.3. Normalized XPS survey scans for natural and synthetic galena samples: (a) synthetic galena before washing, (b) fresh surfaces of natural galena exposed by grinding after exposure to air for two weeks, (c) synthetic galena after washing.

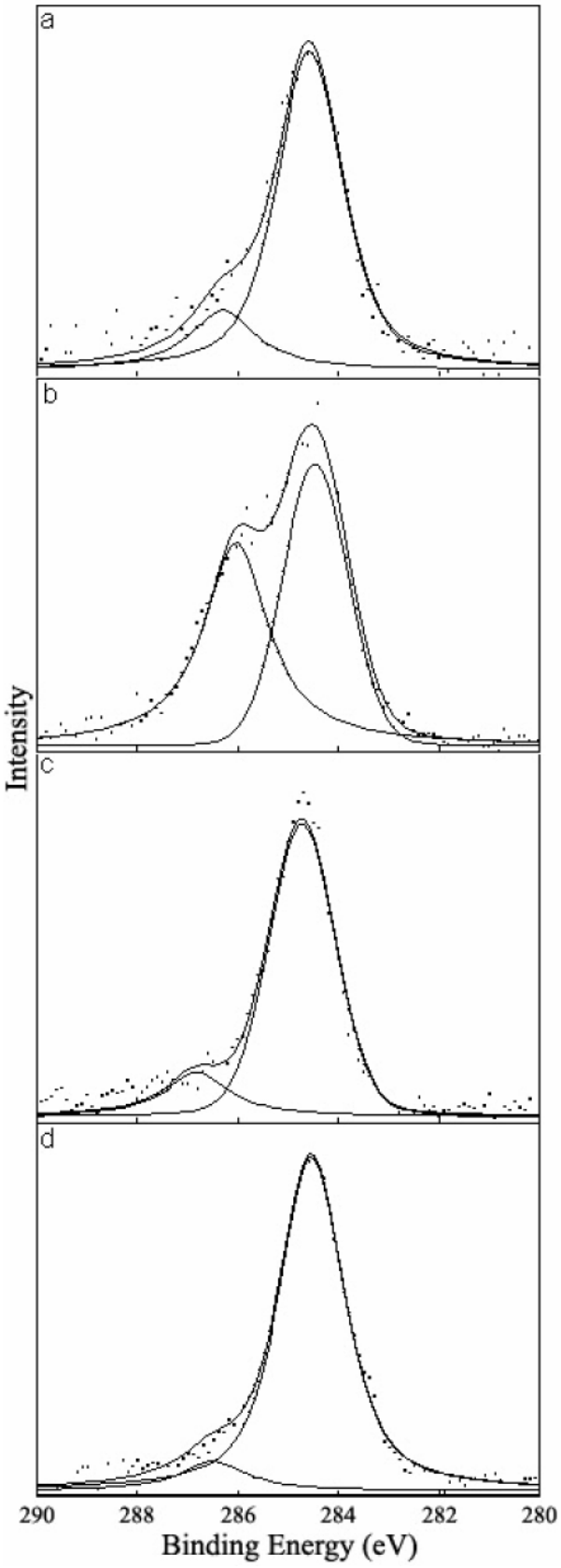

Figure 2.4. C1s XPS spectra for: (a) natural galena, (b) synthetic galena nanocrystals without wash, (c) washed galena nanocrystals before dissolution, (d) washed galena nanocrystals after dissolution.

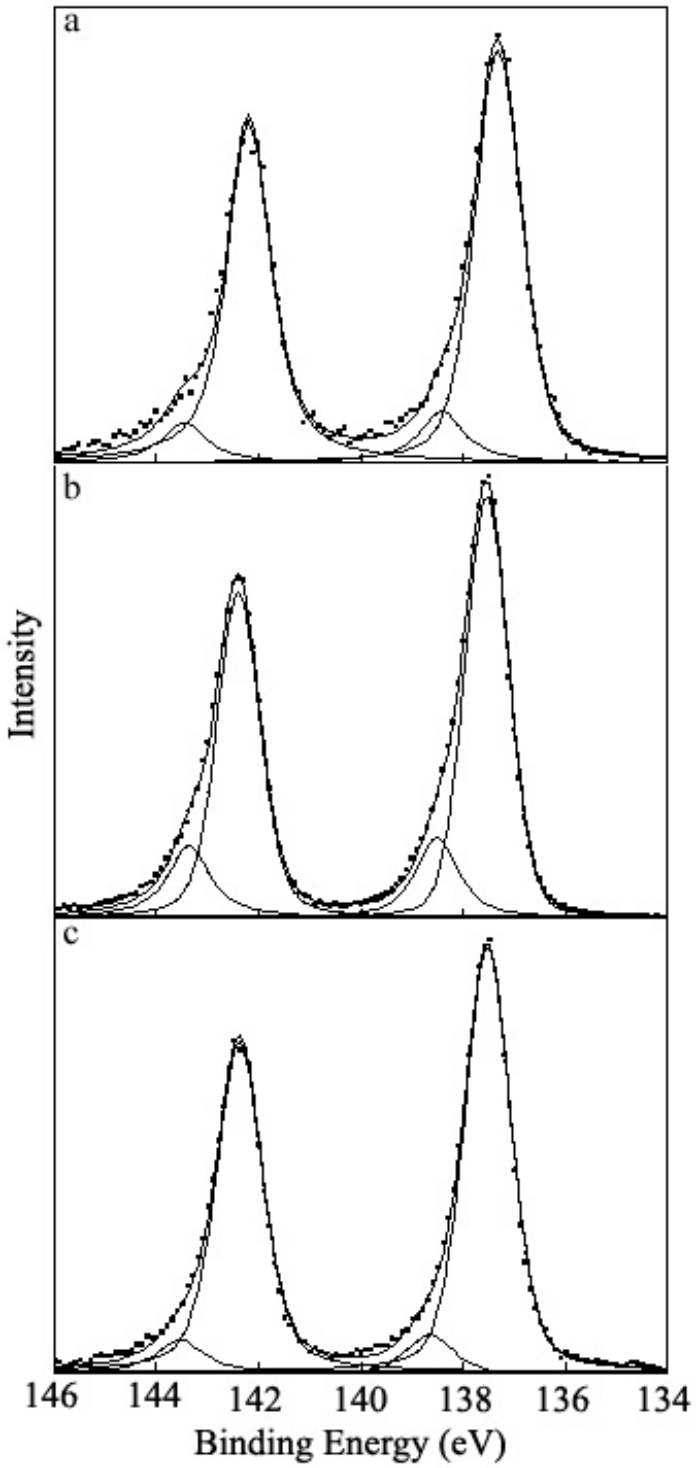

Figure 2.5. Pb4f XPS spectra for: (a) natural galena, (b) washed galena nanocrystals before dissolution, (c) washed galena nanocrystals after dissolution.

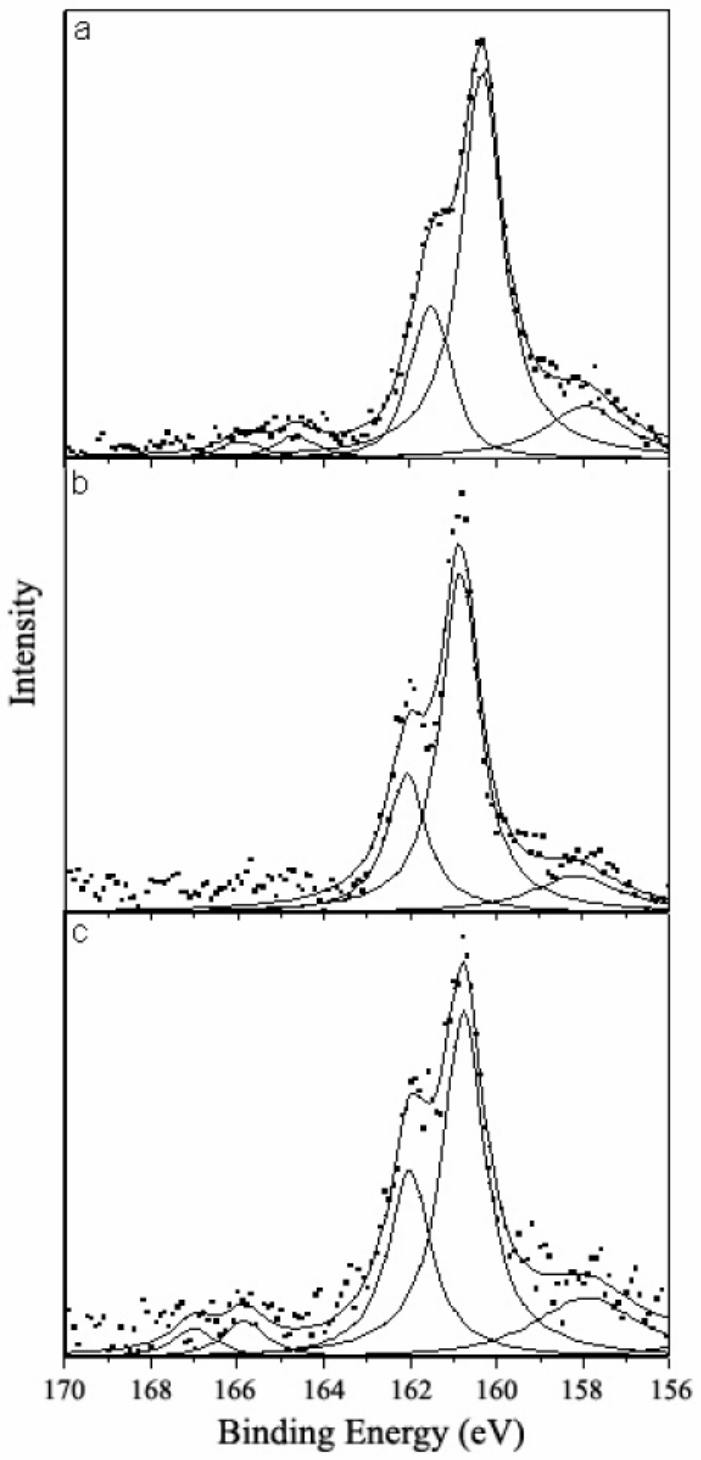

Figure 2.6. S2p XPS spectra for: (a) natural galena, (b) washed galena nanocrystals before dissolution, (c) washed galena nanocrystals after dissolution.

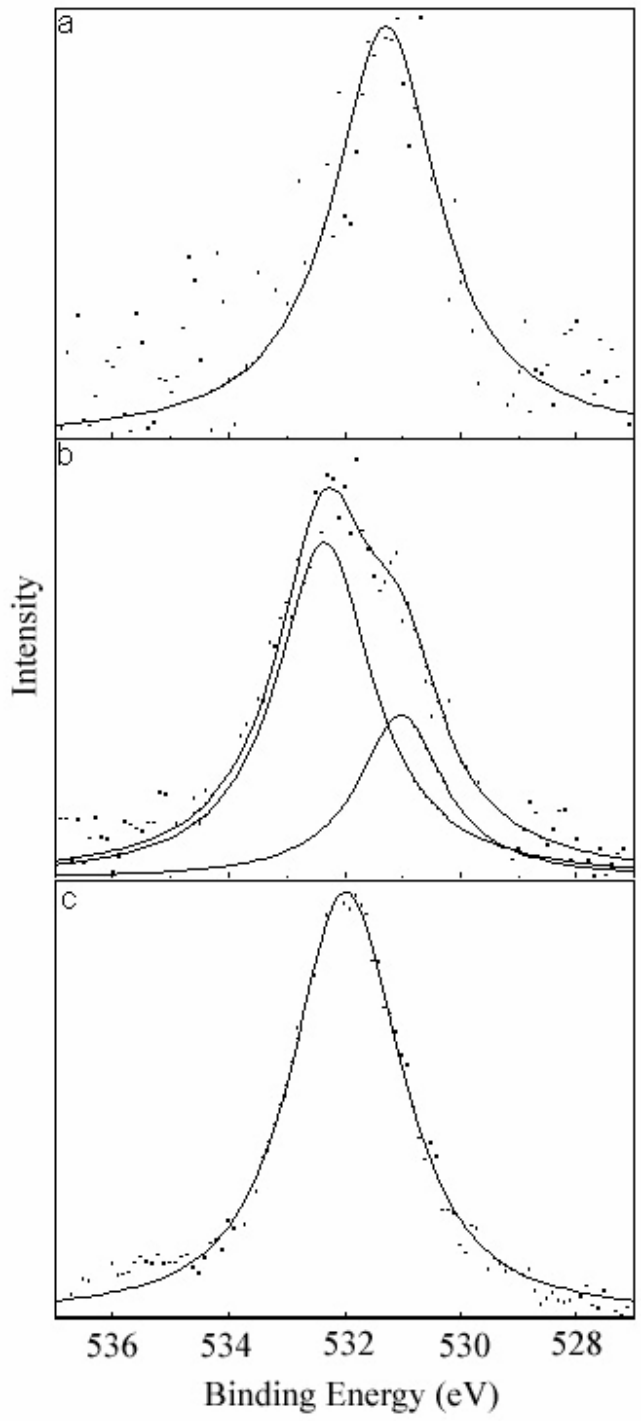

Figure 2.7. O1s XPS spectra for: (a) natural galena, (b) washed galena nanocrystals before dissolution, (c) washed galena nanocrystals after dissolution.

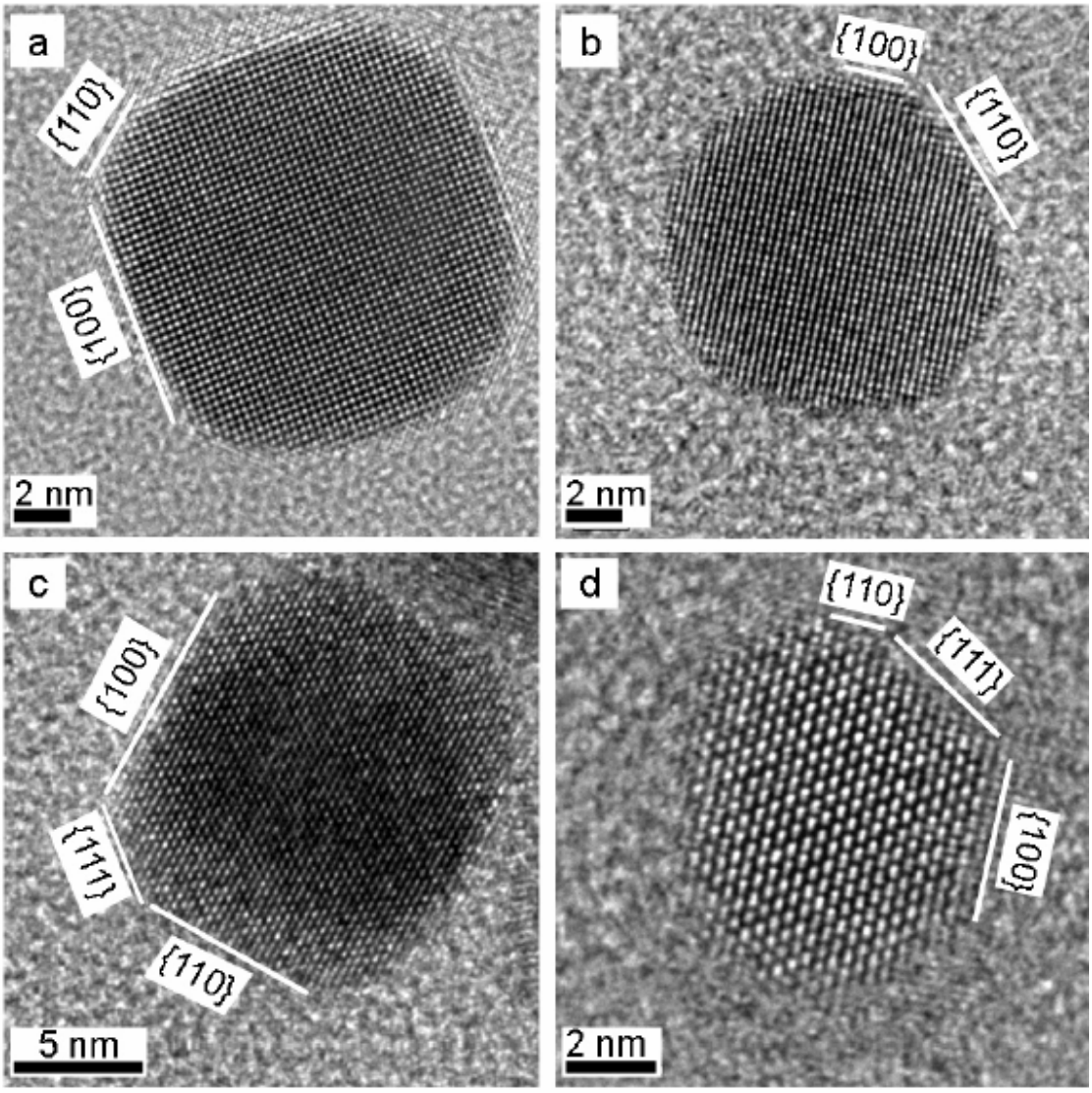

Figure 2.8. HRTEM images of isolated PbS nanocrystals before dissolution (a and c), and after 3-hour-dissolution (b and d). (a) and (b) are viewed along <100> zone axis. (c) and (d) are viewed along <110> zone axis . {110} and {111} faces developed faster relative to {100} faces.

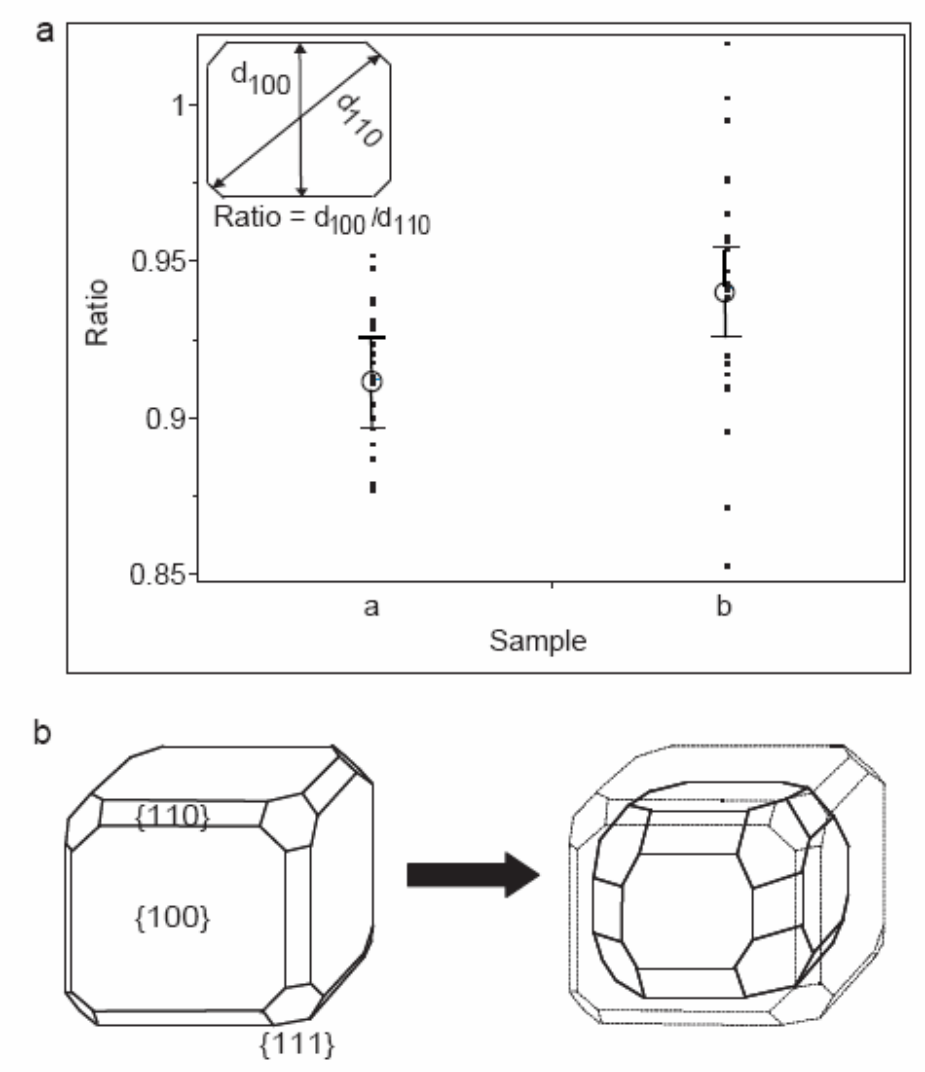

Figure 2.9. (a) Plots of the ratio of particle width in <100> orientation to the width in <110> orientation, as schematically depicted in the insert. Sample a is the washed particles before dissolution, and sample b is the particles after 2-hr dissolution. The dots represent the raw data and the circles are the mean values. The vertical bars in the plot represent 95% confidence intervals for the mean. (b) Schematic drawing of typical morphology change of PbS nanocrystal upon dissolution.

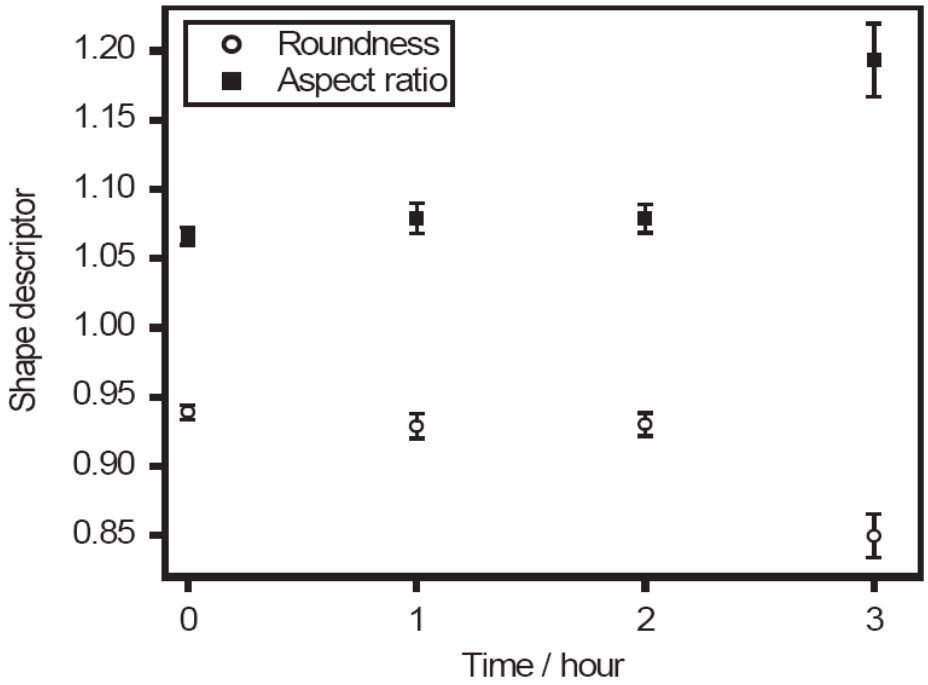

Figure 2.10. Variation in shape descriptors of PbS nanocrytals as a function of dissolution time. Solid squares and circles are the mean values of aspect ratio and roundness, respectively. The vertical bars in the plot represent 95% confidence intervals for the mean.

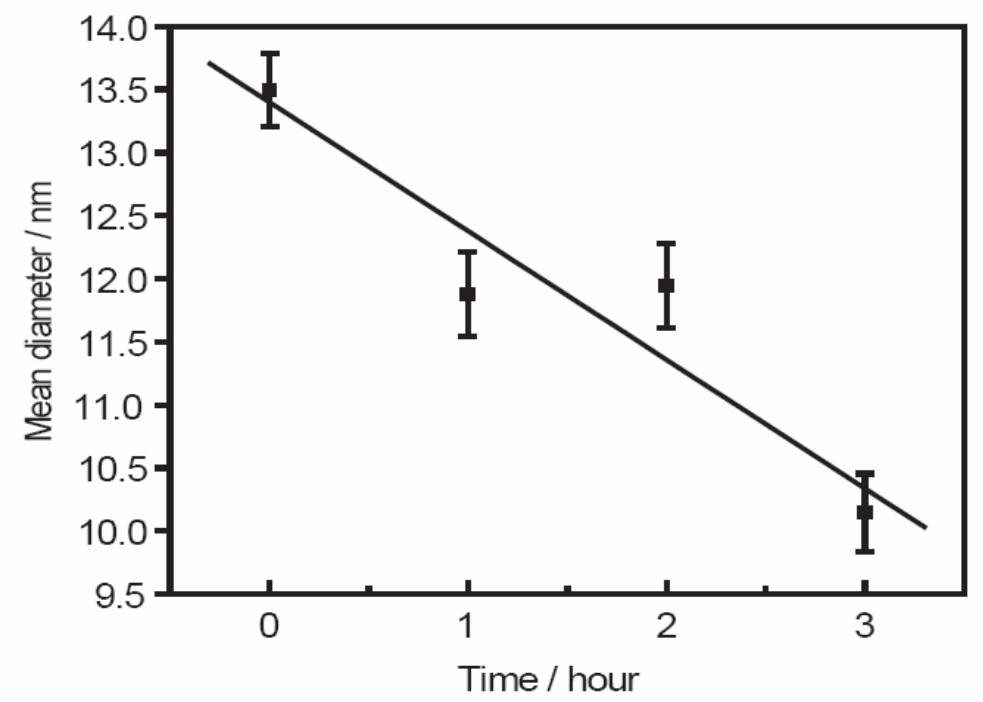

Figure 2.11. Mean diameter of galena nanocrystals dependence on dissolution time at pH 3 and 25°C. The solid line represents the linear regression of all data. ($\Delta d/\Delta t$) = -1.020 nm/hr.

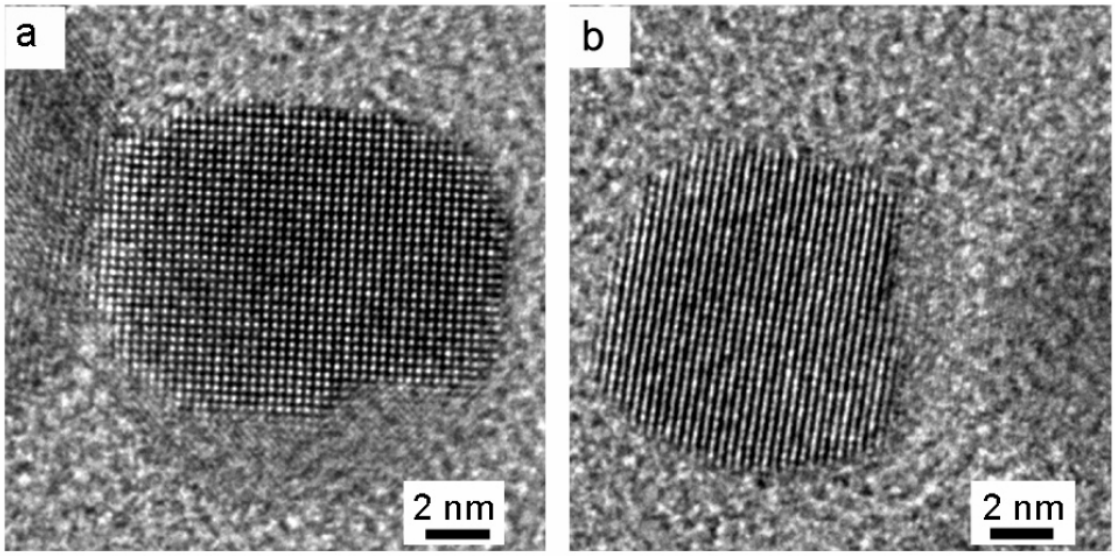

Figure 2.12. Two examples of steps on galena nanocrystals after dissolution.

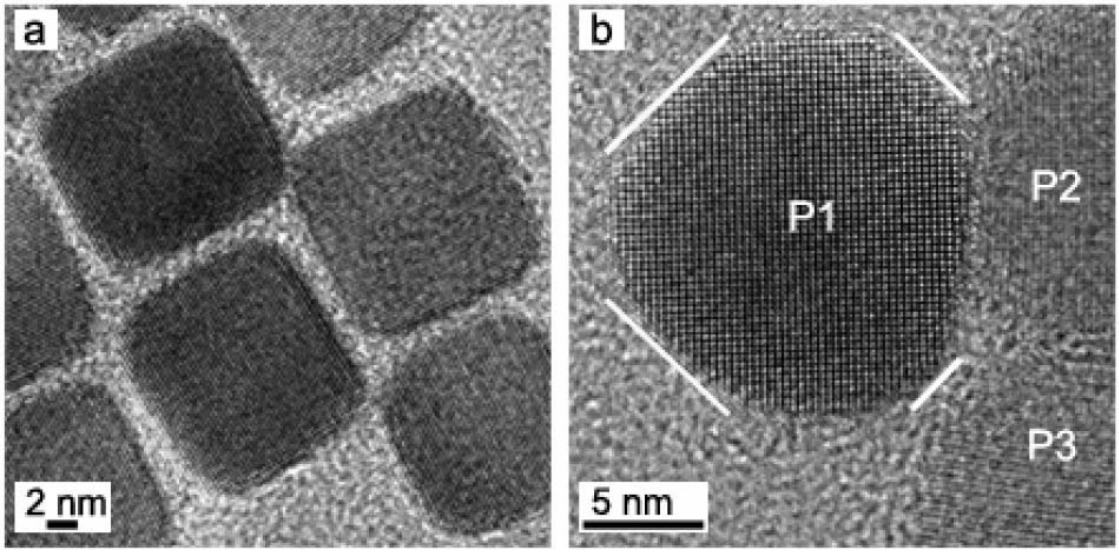

Figure 2.13. (a) HRTEM image of pre-dissolution PbS nanocrystal cluster. The inter-particle spacing is nanoscaled. (b) HRTEM image of the post-dissolution PbS nanocrystal, P_1, adjacent to two nanocrystals, P_2 and P_3. {110} faces on the left side, open to bulk solution, are dissolved faster than the equivalent faces on the right side, close to other particles.

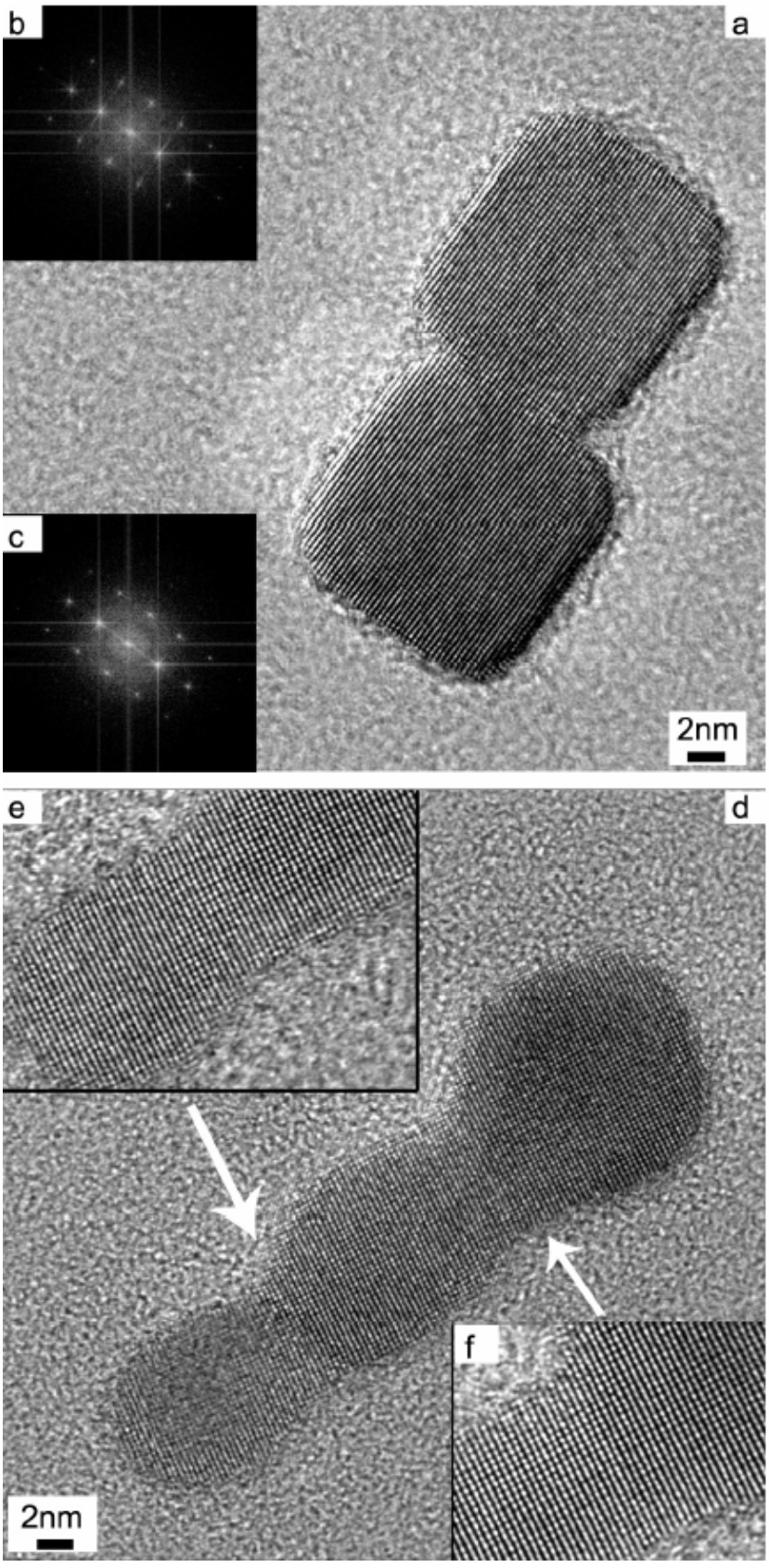

Figure 2.14. HRTEM image of PbS nanocrystal formed by oriented attachment. (a) is a pre-dissolution nanocrystal. (b) and (c) are the Fast Fourier Transform (FFT) pattern of the upper and the lower primary building blocks, respectively. (d) is a post-dissolution nanocrystal. (e) and (f) are high-magnification images of the interfaces between primary building blocks.

REFERENCES

Acero, P., Cama, J., and Ayora, C., 2007. Rate law for galena dissolution in acidic environment. *Chemical Geology* **245**, 219-229.

Awakura, Y., Kamei, S., and Majima, H., 1980. A Kinetic-Study of Non-Oxidative Dissolution of Galena in Aqueous Acid-Solution. *Metall. Mater. Trans. B* **11**, 377-381.

Banfield, J. F. and Zhang, H. Z., 2001. Nanoparticles in the environment, *Nanoparticles and the Environment*. Mineralogical Society of America, Washintong, D.C., USA.

Becker, U. and Hochella, M. F., 1996. The calculation of STM images, STS spectra, and XPS peak shifts for galena: New tools for understanding mineral surface chemistry. *Geochim. Cosmochim. Acta* **60**, 2413-2426.

Bigioni, T. P., Lin, X. M., Nguyen, T. T., Corwin, E. I., Witten, T. A., and Jaeger, H. M., 2006. Kinetically driven self assembly of highly ordered nanoparticle monolayers. *Nat. Mater.* **5**, 265-270.

Bowman, E. T., Soga, K., and Drummond, W., 2001. Particle shape characterisation using Fourier descriptor analysis. *Geotechnique* **51**, 545-554.

Bright, D. S., 2004. Digital image processing with NIH image (Mac) / Scion image (PC) / ImageJ. U. S. National Institute of Standards and Technology Gaithersburg, Maryland.

Cademartiri, L., Bertolotti, J., Sapienza, R., Wiersma, D. S., von Freymann, G., and Ozin, G. A., 2006. Multigram scale, solventless, and diffusion-controlled route to highly monodisperse PbS nanocrystals. *J. Phys. Chem. B* **110**, 671-673.

De Giudici, G., Rossi, A., Fanfani, L., and Lattanzi, P., 2005. Mechanisms of galena dissolution in oxygen-saturated solutions: Evaluation of pH effect on apparent activation energies and mineral-water interface. *Geochim. Cosmochim. Acta* **69**, 2321-2331.

Derjaguin, B. V. and Churaev, N. V., 1986. Properties of water layers adjacent to interfaces. In: Croxton, C. A. (Ed.),*Fluid interfacial phenomena*. Wiley, New York.

Fan, C., Chen, Y., Chen, Y., Ji, J., and Teng, H., 2006. Relationship between solubility and solubility product: the roles of crystal sizes and crystallographic directions. *Geochim. Cosmochim. Acta* **70**, 3820-3829

Fornasiero, D., Li, F. S., Ralston, J., and Smart, R. S. C., 1994. Oxidation of Galena Surfaces .1. X-Ray Photoelectron Spectroscopic and Dissolution Kinetics Studies. *J. Colloid and Interface Sci.* **164**, 333-344.

Gerson, A. R. and O'dea, A. R., 2003. A quantum chemical investigation of the oxidation and dissolution mechanisms of Galena. *Geochim. Cosmochim. Acta* **67**, 813-822.

Hibara, A., Saito, T., Kim, H. B., Tokeshi, M., Ooi, T., Nakao, M., and Kitamori, T., 2002. Nanochannels on a fused-silica microchip and liquid properties investigation by time-resolved fluorescence measurements. *Anal. Chemi.* **74**, 6170-6176.

Hochella, M. F. and Banfield, J. F., 1995. *Chemical weathering of silicates in nature; a microscopic perspective with theoretical considerations.* . Mineralogical Society of America, Washintong, D.C., U.S.A. .

Hochella, M. F., Lower, S. K., Maurice, P. A., Penn, R. L., Sahai, N., Sparks, D. L., and Twining, B. S., 2008. Nanominerals, mineral nanoparticles, and Earth systems. *Science* **319**, 1631-1635.

Joo, J., Na, H. B., Yu, T., Yu, J. H., Kim, Y. W., Wu, F. X., Zhang, J. Z., and Hyeon, T., 2003. Generalized and facile synthesis of semiconducting metal sulfide nanocrystals. *J. Am. Chem. Soc.* **125**, 11100-11105.

Laajalehto, K., Kartio, I., and Suoninen, E., 1997. XPS and SR-XPS techniques applied to sulphide mineral surfaces. *Int. J. Miner. Process.* **51**, 163-170.

Laajalehto, K., Smart, R. S., Ralston, J., and Suoninen, E., 1993. Stm and Xps Investigation of Reaction of Galena in Air. *Appl. Surf. Sci.* **64**, 29-39.

Langford, J. I. and Wilson, A. J. C., 1978. Scherrer after 60 Years - Survey and Some New Results in Determination of Crystallite Size. *J. Appl. Crystallogr.* **11**, 102-113.

Lasaga, A. C., 1998. *Kinetic theory in the earth sciences*. Princeton University Press, Princeton, N.J.

Lasaga, A. C. and Luttge, A., 2004. Mineralogical approaches to fundamental crystal dissolution kinetics. *Am. Mineral.* **89**, 527-540.

Lee, S. M., Jun, Y. W., Cho, S. N., and Cheon, J., 2002. Single-crystalline star-shaped nanocrystals and their evolution: Programming the geometry of nano-building blocks. *J. Am. Chem. Soc.* **124**, 11244-11245.

Luerkens, D. W., 1991. *Theory and application of morphological analysis: fine particles and surfaces*. CRC press, Boca Raton, Florida.

Madden, A. S. and Hochella, M. F., 2005. A test of geochemical reactivity as a function of mineral size: Manganese oxidation promoted by hematite nanoparticles. *Geochim. Cosmochim. Acta* **69**, 389-398.

Madden, A. S., Hochella, M. F., and Luxton, T. P., 2006. Insights for size-dependent reactivity of hematite nanomineral surfaces through Cu2+ sorption. *Geochim. Cosmochim. Acta* **70**, 4095-4104.

Meulenkamp, E. A., 1998. Size dependence of the dissolution of ZnO nanoparticles. *J. Phys. Chem. B* **102**, 7764-7769.

Moulder, J. F., Stickle, W. F., Sobol, P. E., and Bomben, K. D., 1995. *Handbook of X-ray photoelectron spectroscopy*. Physical Electronics, Inc.

Penn, R. L. and Banfield, J. F., 1998. Imperfect oriented attachment: Dislocation generation in defect-free nanocrystals. *Science* **281**, 969-971.

Rasband, W. S., 1997-2007. ImageJ. U. S. National Institutes of Health, Bethesda, Maryland, USA.

Roelofs, F. and Vogelsberger, W., 2006. Dissolution kinetics of nanodispersed gamma-alumina in aqueous solution at different pH: Unusual kinetic size effect and formation of a new phase. *Journal of Colloid and Interface Science* **303**, 450-459.

Russ, J. C., 2002. *The image processing handbook* CRC press, Boca Raton, Florida.

Scherrer, p., 1918. *Nachr. Ges. Wiss. Gottingen, Math-phys, KL* **26**, 98.

Stöber, W. and Arnold, M., 1961. *Anomalien bei* der Ablösung von Kieselsäure von der Oberfläche feinkörniger Siliziumdioxydpulver. *Kolloid Z.* **174**, 20-27.

Tang, R. K., Nancollas, G. H., and Orme, C. A., 2001. Mechanism of dissolution of sparingly soluble electrolytes. *J. Am. Chem. Soc.* **123**, 5437-5443.

Tanuma, S., Powell, C. J., and Penn, D. R., 1991. Calculations of Electron Inelastic Mean Free Paths .3. Data for 15 Inorganic-Compounds over the 50-2000-Ev Range. *Surf. Interface Anal.* **17**, 927-939.

Tester, J. W., Worley, W. G., Robinson, B. A., Grigsby, C. O., and Feerer, J. L., 1994. Correlating Quartz Dissolution Kinetics in Pure Water from 25-Degrees-C to 625-Degrees-C. *Geochimica Et Cosmochimica Acta* **58**, 2407-2420.

Tsukahara, T., Hibara, A., Ikeda, Y., and Kitamori, T., 2007. NMR study of water molecules confined in extended nanospaces. *Angew. Chem., Int. Ed. Engl.* **46**, 1180-1183.

Zhang, S., Li, J. P., Wang, Y. R., and Hu, G. Q., 2004. Dissolution kinetics of galena in acid NaCl solutions at 25-75 degrees C. *Applied Geochemistry* **19**, 835-841.

Chapter 3 - Influence of size and aggregation on the non-oxidative dissolution of galena (PbS)

Juan Liu and Michael F. Hochella, Jr.

Center for NanoBioEarth, Department of Geosciences, Virginia Tech, Blacksburg, VA 24061, USA

(Written in the format and style of *Science*; for possible submission there.)

A report from the National Research Council of the U.S. National Academy of Sciences (NAS), released in December 2008, finds "serious weaknesses" in the U.S. federal government's plan to address the potential health and environmental risks posed by the manufactured nanomaterials that are being increasingly used in medical treatments, food additives, advanced electronics and batteries, skin-care products, and many other revolutionary materials, products, and processes (*1*). The report makes it very clear that there is a large gap between, for example, the benefits of nanotechnology in developing therapies for disease, and the very real potential risks of nanomaterial exposure to humans and the environment. At the same time, naturally occurring nanoparticles are ubiquitous in the hydrosphere, atmosphere, and soil environments as a result of mineral weathering, microbial activity, nucleation/crystallization processes, and anthropogenic activities, etc. (*2*). Perhaps it is not surprising that there are a number of the same, or very similar nanomaterials that are both synthesized and studied for/used in commercial applications, as well as found naturally in the environment, playing important roles in geo- and biochemical processes. These nanomaterials provide a valuable link between the fields of nanogeoscience (*2*) and the study of the environmental implications of nanotechnology (*2*), these two areas of study being highly complimentary. One such material is nanoparticulate lead sulfide (PbS) which has been synthesized by materials scientists (*3*), and which can also be found in nature as small grains of the mineral galena (*4*). In order to better understand these types of nanomaterials, many efforts have been made to investigate their size-dependent

properties (*4-8*), because they may behave quite differently relative to bulk materials. Specifically, the understanding of size-dependent dissolution of nanoparticles is one of the keys to assessing potential impacts on the environment and human health, and is also very important for developing industrial applications of nanomaterials (*10*) and essential for the development of nanoparticles in the field of drug delivery (*9*). A modified Kelvin equation (Eq. 1) has long been used to describe the thermodynamic prediction that solubility is expected to exponentially increase as the grain size decreases into the nano-range according to:

$$\frac{S}{S_0} = \exp[\frac{2\gamma \overline{V}}{RTr}] \tag{3.1}$$

where S is the solubility (in mol · kg^{-1}) of fine grains with inscribed radius r in m, and S_0 is the solubility of the bulk material. $\overline{V}$ is molecular volume in $m^3 \cdot mol^{-1}$, γ is the surface free energy in mJ · m^{-2}, R is the gas constant in nJ · mol^{-1} · K^{-1}, and T is the temperature in K. However, so far few data of nanoparticles dissolution experiments have been reported to support this theoretic prediction, and the range of validity of this equation has been questioned based on theory and experiment (*10*). Moreover, most current dissolution studies of nanoparticles actually measured the dissolution rates of nanoparticles that were aggregated to some extent in solution (*11, 12*), which will effect the apparent dissolution rate. The aggregation state was not characterized in these studies, which makes it difficult to interpret data and evaluate the size effect alone.

In natural aquatic systems, a large portion of colloids and nanoparticles exist in aggregates (*13*). Aggregates that are smaller than a critical size could be stable and highly mobile in waters (*14*). Engineered nanoparticles that are produced and used as dry powders usually remain in an aggregated state even after exposed to an aqueous environment (*15*). Aggregation is expected to hinder dissolution by introducing kinetic hindrance to the diffusion process (*16*). However, no previous experimental studies have been conducted to compare dissolution reactivity of aggregated and non-aggregated nanoparticles. It is important to determine whether the observed dissolution of aggregated nanoparticles is dominated by inherent particle size effect or by the aggregation effect.

Non-oxidative dissolution of dispersed galena (PbS) nanoparticles in acidic solution has been reported in our previous paper (*4*). In order to eliminate aggregation as

a factor, nanoparticles were attached on the surface of a TEM (Transmission Electron Microscopy) grid, and the dissolution rates were directly measured via monitoring the size change of nanoparticles using TEM. The geometric surface area (A_{geo}) normalized rate of dispersed galena nanoparticles in deoxygenated HCl solution (pH=3) was measured to be 4.4 x 10^{-9} mol m^{-2} s^{-1} (*4*). The present study aims to investigate the influence of particle size and aggregation state on the dissolution of galena nanoparticles, and to determine which of these two effects is more pronounced in galena nanoparticle dissolution.

The synthetic galena nanocrystals, as shown in Fig. 3.1a and 3.1b, are nearly mono-dispersed with an equivalent diameter of 14.4 ± 1 nm (1 is standard deviation) and a truncated-cubic shape. The capping groups on nanocrystals could be removed by repeatedly washing using isopropyl alcohol, and no unwanted contaminants were generated after washing (*4*). To assess the size effect on dissolution, galena microcrystals with the similar shape as the nanocrystals were synthesized via a hydrothermal method (*17*). The representative scanning electron microscopy (SEM) image (Fig. 3.1c and 3.1d) shows that the microcrystals mostly are cubic with the equivalent diameter is 3.1 ± 0.8 μm (0.8 is standard deviation). The XRD patterns of the microcrystals were highly consistent with galena. Galena microcrystals were dissolved under similar conditions compared to the nanocrystals, but using wet chemical method. Fig. 3.2a shows the change of the dissolved Pb^{2+} concentration as a function of dissolution time in deoxygenated HCl (pH =3) solution at 25 °C over 16 h. All data can be well fit using a linear function. The increasing rate of Pb^{2+} ions, $\Delta C_{Pb}/\Delta t$, determined from the slope of the line is 0.01865 mg L^{-1} h^{-1}. Assuming the microcrystals are uniform smooth cubes with an equivalent diameter of 3.1 μm, the geometric specific surface area (SSA) of microcrystals is 0.26 m^2 g^{-1}. The geometric surface area (A_{geo}) normalized dissolution rate can be calculated by

$$r = \frac{V}{S}\left(\frac{\Delta C_{Pb}}{\Delta t}\right) \tag{3.2}$$

where V is the volume of the acid solution, and S is the total surface area of galena particles. For 0.05 g galena microcrystals dissolved in 0.4 L HCl solution, the A_{geo} normalized dissolution rate is 7.7 x 10^{-10} mol m^{-2} s^{-1}. Therefore, the rate of galena

microcrystals is one order of magnitude slower than the rate of dispersed nanocrystals (Table 1).

The faster dissolution of nanoparticles may be attributed to the following reasons: first, as suggested by the modified Kelvin equation (Eq. 1), dissolution is more thermodynamically favored on nanocrystals relative to bulk materials. Particles with a smaller radius of positive curvature (convex) are energetically unfavorable (*18*). Thus, the fine particles are subject to preferential dissolution. Second, transport of solvated molecules from particle surface to bulk solution is faster on nanoparticles than on bulk materials, because diffusion layer thickness has been experimentally found to decrease with particle size (*19*). The faster transport, as an important step in dissolution, may lead to the relatively faster dissolution rate. Third, different surface reactivity of nanoparticles and microcrystals can also influence dissolution rate. Even with the same total surface area, nanocrystals have a larger fraction of atoms at edges and corners than the bulk particles. Atoms at these sites have higher reactivity than ones on flat surfaces and could dissolve more quickly. Therefore, the more active sites on nanocrystals may also contribute to the faster dissolution.

To assess the aggregation effect, dissolution rate of aggregated galena nanoparticles was measured under the same conditions for microcrystals and dispersed nanoparticles. After removing the capping groups, the synthetic galena nanoparticles quickly aggregated, and the resulting aggregates were collected by centrifugation. For dissolution experiments, the precipitates were sonicated in a small volume of HCl solution (pH =3) to form a suspension of aggregates, and then added the suspension to a batch reactor with oxygenated acid solution. The size of aggregates in the suspension was measured by dynamic light scattering (DLS). The mean hydrodynamic diameter of aggregates in HCl at pH 3 is 240 nm, and the result was quite stable over the 3h measurement. However, in SEM images of aggregates, the size of the aggregates varies from hundreds of nanometers to several microns. The larger size observed by SEM could be due to the further agglomeration during drying samples. The representative SEM and TEM images (Fig. 3.3a and 3.3b) reveals that the aggregates have a rough surface and large porosity, so it is difficult to use a simple model to calculate the geometric SSA of nanoparticle aggregates. Alternatively, the BET (Brunauer-Emmett-Teller) method was

used to measure the SSA of aggregates which is 10.7067 ± 0.0329 m^2 g^{-1}. In order to investigate the effect of filtration on the measured dissolution rates, filters with two different pore sizes were separately used for sampling in this study. One is a syringe filter with a pore size of 0.1 μm, and the other one is a centrifugal tube (Amicon Ultra-4, Milipore) with a cut-off of 100k NMWL (nominal molecular weight limit) which approximately equals 6.2 nm. Fig. 3.2b shows the concentration changes of dissolved Pb^{2+} ions as a function of time using these two kinds of filters. The slopes of the linear fits for the two sets of data are very similar, so there are no significant amount of primary nanoparticles or small aggregates formed as a result of dissolution. Using $\Delta C_{Pb}/\Delta t$ = 0.4926 mg L^{-1} h^{-1} and A_{BET} = 11.7067 m^2 g^{-1}, the surface area-normalized dissolution rate is 4.7 x 10^{-10} mol m^{-2} s^{-1}. This rate is in the same order of magnitude as the rate of microcrystals, but one order of magnitude smaller than that of dispersed nanoparticles (as shown in Table 1).

The slow dissolution of nanoparticle aggregates may be related to the dissolution inhibition in nanoscaled interparticle space. The high-resolution TEM image (Fig. 3.3c) of the nanoparticle cluster shows that the nanoscaled interparticle spacing, as small as 1 to 2 nm, can be formed between two adjacent nanoparticles. It has been found that dissolution on surfaces that were closely adjacent to other nanoparticles is considerably slower than the faces to bulk solution (*4*). The dissolution inhibition in confined space may be due to the abnormal fluid properties of nanospaces. It has been experimentally shown that viscosity of aqueous solution is larger in confined space than in open space (*20-22*). According to Strokes-Einstein relation, increased viscosity may result in decrease of diffusion coefficient (D). The dissolution rate constant, *k*, depends on the diffusion coefficient (D) of solute molecules as shown:

$$k = \frac{A \times D}{V \times h} \tag{3.3}$$

where *A* is the surface area of solutes, *V* is the volume of solution, and *h* is the thickness of diffusion layer. This relation indicates that the reduced D may lead to the smaller *k*, i.e. the slower dissolution. Another potential explanation for the dissolution inhibition in confined space could be the overlap of the diffusion layers on the surface of two adjacent nanoparticles. In particle dissolution, molecules of dissolving solid transport from the

particle surface to the bulk solution through a diffusion layer. The diffusion layer has the higher concentration of solvated molecules than that of bulk solution, so dissolution can be driven by the material transport due to this concentration gradient. If the interparticle spacing is smaller than the total thickness of the diffusion layers on two adjacent nanoparticles, their diffusion layers may be overlapped. In this situation, the concentration gradient between the diffusion layer and the bulk solution is lacking and consequently the driving force for dissolution will disappear. Moreover, the diffusion of acid solution and solute molecules is reduced in the dense diffusion layers. Aggregation turns a large portion of external surface on nanoparticles into internal surface in aggregates. Correspondingly, the transport mechanism on these surfaces switches from fluid flow to diffusion (*23*), so the reduced diffusion in the confined space may substantially affect transport rate of ions onto and from the surfaces and consequently lead to slow dissolution.

In Table 3.1, it can be seen that, for galena microcrystals, geometric SSA is similar to BET SSA, but for nanoparticles geometric SSA is much larger. This result implies that nanoscale interparticle spacing or micropores may be common in nanoparticle aggregates. The absorption of N_2 molecules in the confined space is inhibited, resulting in the smaller BET SSA compared to geometric SSA. However, the pore size in microcrytal aggregates is generally large enough for N_2 adsorption because of their inherent large particle size. Aggregation effect for microcrystals dissolution is not as substantial as for nanocrystals. Therefore, it is reasonable to compare the dissolution rate of microcrystals to that of dispersed nanoparticles, though the microcrystals aggregated to some extent as shown in the SEM image (Fig. 3.1c). It is worth it to mention that the BET method only can measure SSA of dry powders, not SSA of aggregates in acid solution. Moreover, BET surface area probably includes a portion of inactive surface area for dissolution. However, so far BET method is still the most commonly used method for SSA measurement. New methods or models are needed to quantify SSA of aggregates in wet solution (*24*). Developing effective and accurate methods for characterizing properties and aggregation state of nanoparticle aggregates is also needed.

The higher dissolution reactivity of nanoparticles, compared to their bulk counterparts, implies that nanoparticels, especially toxic-metal containing nanoparticles, may be very reactive in the aquatic systems and have high tendency to release toxic metals into the environment. Therefore, special attention should be paid on the nanoparticle exposure in natural aquatic environment. On the other hand, the high reactivity of nanoparticles can be utilized in industrial applications, such as improving drug delivery efficiency using nanoparticles.

The reduced dissolution rate of nanoparticle aggregates indicates that the increased dissolution rate of individual particles due to the size effect can be counteracted by the aggregation effect. In environment remediation, inducing or promoting aggregation of nanoparticles could be used to reduce reactivity of toxic nanoparticles. When developing industrial applications of nanoscale materials, aggregation effect should be considered. In order to exert unique reactivity of nanomaterials in aqueous solutions, stabilization treatment may be required to prevent aggregation of nanomaterials. For assessing environmental risk or developing industrial applications of nanomaterials, it is not sufficient to only characterize the inherent properties of pure nanomaterials. The size effects of nanomaterials must be considered with the characteristics of the environment matrix that they are in. It is important to investigate how their properties change with external factors, such as their aggregation state, absorption of organic matter, interaction with organisms, etc.

References and Notes

1. N. R. Council, Ed. (The national academies press, Washington, D. C. , 2008).
2. M. R. Wiesner *et al.*, *Environ Sci Technol* **In press**, (2008).
3. J. Joo *et al.*, *J. Am. Chem. Soc.* **125**, 11100 (Sep 10, 2003).
4. J. Liu, D. M. Aruguete, J. R. Jinschek, J. D. Rimstidt, M. F. Hochella, Jr., *Geochim Cosmochim Ac* **72**, 5984 (2008).
5. A. S. Madden, M. F. Hochella, *Geochim. Cosmochim. Acta* **69**, 389 (Jan 15, 2005).
6. I. V. Chernyshova, M. F. Hochella, A. S. Madden, *Phys Chem Chem Phys* **9**, 1736 (2007).
7. P. J. Vikesland, A. M. Heathcock, R. L. Rebodos, K. E. Makus, *Environ Sci Technol* **41**, 5277 (Aug 1, 2007).
8. H. Z. Zhang, B. Gilbert, F. Huang, J. F. Banfield, *Nature* **424**, 1025 (Aug 28, 2003).
9. R. H. Muller, C. Jacobs, O. Kayser, *Adv Drug Deliver Rev* **47**, 3 (Mar 23, 2001).
10. R. K. Tang, G. H. Nancollas, C. A. Orme, *J. Am. Chem. Soc.* **123**, 5437 (Jun 13, 2001).
11. E. A. Meulenkamp, *J. Phys. Chem. B* **102**, 7764 (Oct 1, 1998).
12. W. Vogelsberger, J. Schmidt, F. Roelofs, *Colloid Surface A* **324**, 51 (Jul 1, 2008).
13. J. R. Lead, K. J. Wilkinson, *Environ Chem* **3**, 159 (2006).
14. B. Gilbert, G. P. Lu, C. S. Kim, *J Colloid Interf Sci* **313**, 152 (Sep 1, 2007).
15. Y. Zhang, Y. S. Chen, P. Westerhoff, K. Hristovski, J. C. Crittenden, *Water Res* **42**, 2204 (Apr, 2008).
16. P. Borm *et al.*, *Toxicol Sci* **90**, 23 (Mar, 2006).
17. Y. H. Ni, X. W. Wei, H. M. Hong, X. Ma, *Mater Res Bull* **42**, 17 (Jan 18, 2007).
18. A. W. Adamson, A. P. Gast, *Physical chemistry of surfaces*. (Wiley, New York, 1997).
19. M. Bisrat, C. Nystrom, *Int J Pharm* **47**, 223 (Nov, 1988).
20. B. V. Derjaguin, N. V. Churaev, Eds., *Properties of water layers adjacent to interfaces*, (Wiley, New York, 1986), pp. 663-738.
21. A. Hibara *et al.*, *Anal. Chemi.* **74**, 6170 (Dec 15, 2002).
22. T. Tsukahara, A. Hibara, Y. Ikeda, T. Kitamori, *Angew. Chem., Int. Ed. Engl.* **46**, 1180 (2007).
23. M. F. Hochella, J. F. Banfield, *Chemical weathering of silicates in nature; a microscopic perspective with theoretical considerations.* . W. A.F., B. S. L., Eds., Rev Mineral (Mineralogical Society of America, Washintong, D.C., U.S.A. , 1995), vol. 31, pp. 384.
24. D. M. Cwiertny, R. M. Handler, M. V. Schaefer, V. H. Grassian, M. M. Scherer, *Geochim Cosmochim Ac* **72**, 1365 (Mar 1, 2008).

25 Grants from the U.S. Department of Energy (DE-FG02-06ER15786) and the Institute for Critical Technology and Applied Science at Virginia Tech provided major financial support for this study

Table 3.1. Size, geometric SSA (A_{geo}), BET SSA (A_{BET}), geometric surface area normalized dissolution rate (R_{geo}), and BET surface area normalized dissolution rate (R_{BET}) of primary nanocrystals, microcrystals, and nanocrytal aggregates

	Average size	A_{geo} ($m^2\ g^{-1}$)	A_{BET} ($m^2\ g^{-1}$)	R_{geo} (mol $m^{-2}\ s^{-1}$)	R_{BET} (mol $m^{-2}\ s^{-1}$)
Nanocrystals	14.4 ± 1 nm	55.0	—	4.4×10^{-9}	—
Microcrystals	3.1 ± 0.8 μm	0.26	0.2854 ± 0.0017	7.7×10^{-10}	7.0×10^{-10}
Aggregates	240 nm	—	11.7067 ± 0.0329	—	4.7×10^{-10}

Supporting online material

Galena Synthesis.

Synthesis and purification of galena nanocrystals were described in detail in Liu et al. (*4*). Basically, galena nanocrystals were synthesized by the reaction of $PbCl_2$ and elemental sulfur in oleylamine (OLA) under inert atmosphere (*3*). Synthetic galena nanocrystals are totally or partially coated by OLA ligands, which stabilize nanocrystals in hexanes. These capping groups were removed before any dissolution experiments by repeatedly washing nanocrystals using isopropyl alcohol. Uncoated nanocrystals can quickly aggregate in aqueous solution, and the aggregates can be collected by centrifugation.

Galena microcrysals were synthesized by a hydrothermal method (*17*). All reagents were purchased from Sigma-Aldrich and used without further purification. The procedure is as follows: 1 mmol $(CH_3COO)_2Pb$ and 4 mmol $Na_2S_2O_3$ were dissolved in 9.2 mL deionized water, respectively. The solutions were transferred into a 23 mL Parr* acid digestion bomb with an inserted PTFE sample cup. Then, the system was closed tightly and heated in an oven to 150 °C for 20 hours. Black precipitates were collected, washed with deionized water several times, and dried in air at 50 °C.

Particle Characterization.

The crystal phases of the synthetic nanocrystals and microcrystals were identified by a Pan Analytical X'PERT-Pro X-ray powder diffractometer, equipped with a Co Kα source. Samples were mounted on a zero-background sample holder. Diffraction patterns were collected in the 2θ range of 20-100° using a step size of 0.067°.

Size and morphology of primary nanocrystals and aggregates were observed by a Philips EM420 Transmission Electron Microscope operated in bright field mode at 100 KeV. For primary nanocrystal analysis, sample was prepared by dipping a carbon-coated 400-mesh copper TEM grid into the nanocrystal suspension and then drying the grid in air. For nanocrystal aggregate analysis, aggregates were sonicated in hexanes until no aggregates can be seen in the suspension. A drop of this suspension was then applied to a TEM grid.

Dynamic light scattering (DLS) was used to measure the size of nanocrystal aggregates in hydrochloric acid solutions. All measurements were made with a Malvern Zetasizer 3000 HS. Suspensions for the DLS analysis were prepared by sonicating dry aggregated nanocrystals in HCl solution at pH 3 for 1 min. Three repeats for a single acquisition was chosen to ensure that the noise on the data was less than 0.1%. The lead concentration in the suspension for DLS was about 0.30 ppm. Diluting the suspension did not change the size of aggregates. The change of aggregate size as a function of time was monitored by DLS in three hours.

To complement DLS results, the size and aggregation characterization of nanoparticle aggregates were observed by high-resolution field emission scanning electron microscopy (FESEM) (LEO 1550, FEG at 5 kV). About 5 mg nanocrystal aggregates was sonicated in ~5 mL HCl solution (pH = 3) to form clear suspension. A drop of this suspension was applied to a piece of Boron-doped Silicon wafer that was attached onto a SEM sample stub, and then dried in air at 40°C. The nanocrystals aggregate samples were not coated before SEM measurements. In addition, SEM was

also used to observe the size and morphology of galena microcrystals. Microcrystal samples were coated by 5 nm Au film to increase the conductivity.

The particle size was determined by analyzing microscopic images via the image processing and analysis program, Image J. Particle diameter (size) of nanoparticles measured by analyzing TEM images is defined as the diameter of a circle having the same projected area as the particles. To determine the size, or effective diameter (d_e), of microcrystal, edge length (a) of cubic crystal in SEM images was measured, and then converted to d_e by the equation

$$d_e = 2\sqrt{\frac{a^2}{\pi}} \tag{S.1}$$

Because SEM images show microcrystals in three-dimension, only faces nearly parallel to the image are measured.

The specific surface area (SSA) of nanoparticle aggregates and microcrystals were determined via the BET (Brunauer-Emmett-Teller) method. Measurements were carried out on a TriStar II 3020 system (Micromertics Analytical Services) by determining the nitrogen adsorption-desorption isotherms at 77K. Before analysis, the samples were heated to 60°C for 16 h at a rate of 10°C/min under vacuum. BET SSA of microcrystals is 0.2854 ± 0.0017 m^2/g, and the value for nanoparticle aggregates is 10.7067 ± 0.0329 m^2/g. The geometric SSA, A_{geo}, of microcrystals was calculated by assuming that particles are smooth cubes according to

$$A_{geo} = \frac{6}{\rho \cdot d_e} \tag{S.2}$$

where ρ is the density of galena.

Dissolution Experiments

Dissolution experiments were performed in a glass reactor (~750 mL capacity) under constant mechanical stirring at 25 °C. 495 mL of hydrochloric acid solution (pH 3) were added to the chamber and purged with nitrogen for 30 minutes to remove dissolved O_2. Galena particles were dispersed in 5 mL HCl solution (pH 3) by sonication. Then, the chamber was quickly opened to add the 5 mL suspension, but otherwise was sealed. Nitrogen purging was maintained throughout the experiment and the pH was monitored constantly with a pH meter. Samples of 6 mL solutions were taken after certain intervals and immediately filtered. For the dissolution of microcrystals, the syringe filters with a pore size of 0.45 μm were used. In the dissolution of nanocrystals aggregates, filters with two different pore sizes were used, in order to evaluate the effect of filtration on the measured dissolution rate. One is the syringe filter with a pore size of 0.1μm, and the other one is the centrifugal tube (Amicon Ultra-4, Milipore) with a cut-off of 100k NMWL (nominal molecular weight limit), which equals the pore size of ~6.2 nm. Pb concentrations of the sampled solutions were measured using an inductively coupled plasama atomic emission spectrograph (ICP-AES). The detection limit for Pb is 0.016 ppm.

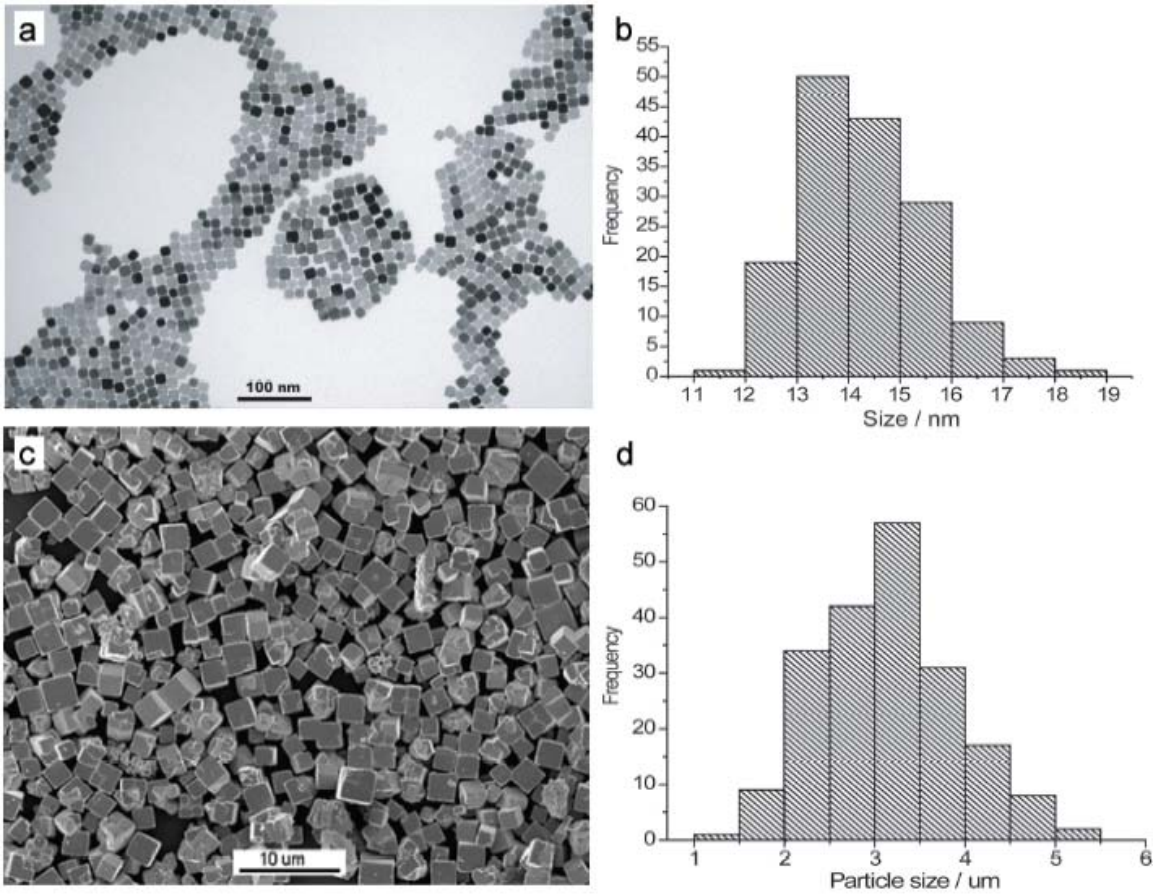

Figure 3.1. Comparison of nanoscale and microscale galena particles. (a) TEM images of galena nanocrystals. (b) the size distribution of nanocrystals. (c) SEM images of galena microcrystals. (d) the size distribution of microcrystals

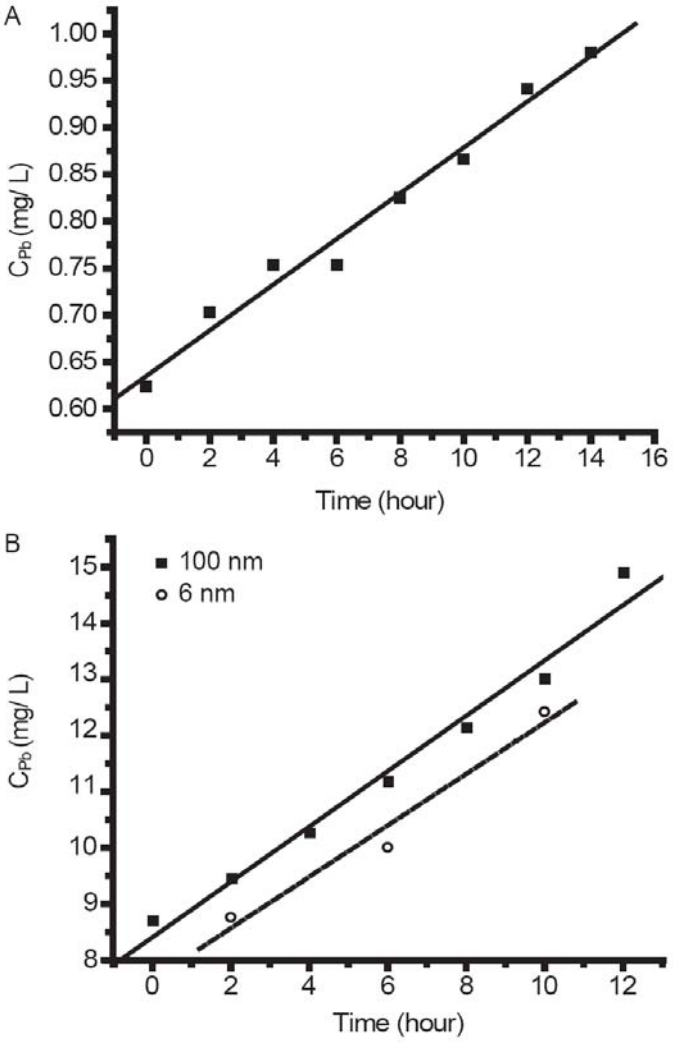

Figure 3.2. Lead concentration vs. time in the dissolution of galena particles in HCl solution at pH 3 and 25 °C. (a) galena microcrysals. The line is the linear fit of raw data. Its slope is $(\Delta C_{Pb}/\Delta t) = 0.01865$ mg L^{-1} h^{-1}. (b) nanocrystals aggregates using 100nm filter (■) and 6 nm filter (○), respectively. The slope of the solid line is $(\Delta C_{Pb}/\Delta t) = 0.4926$ mg L^{-1} h^{-1}; the slope of the dashed line is $(\Delta C_{Pb}/\Delta t) = 0.458$ mg L^{-1} h^{-1}.

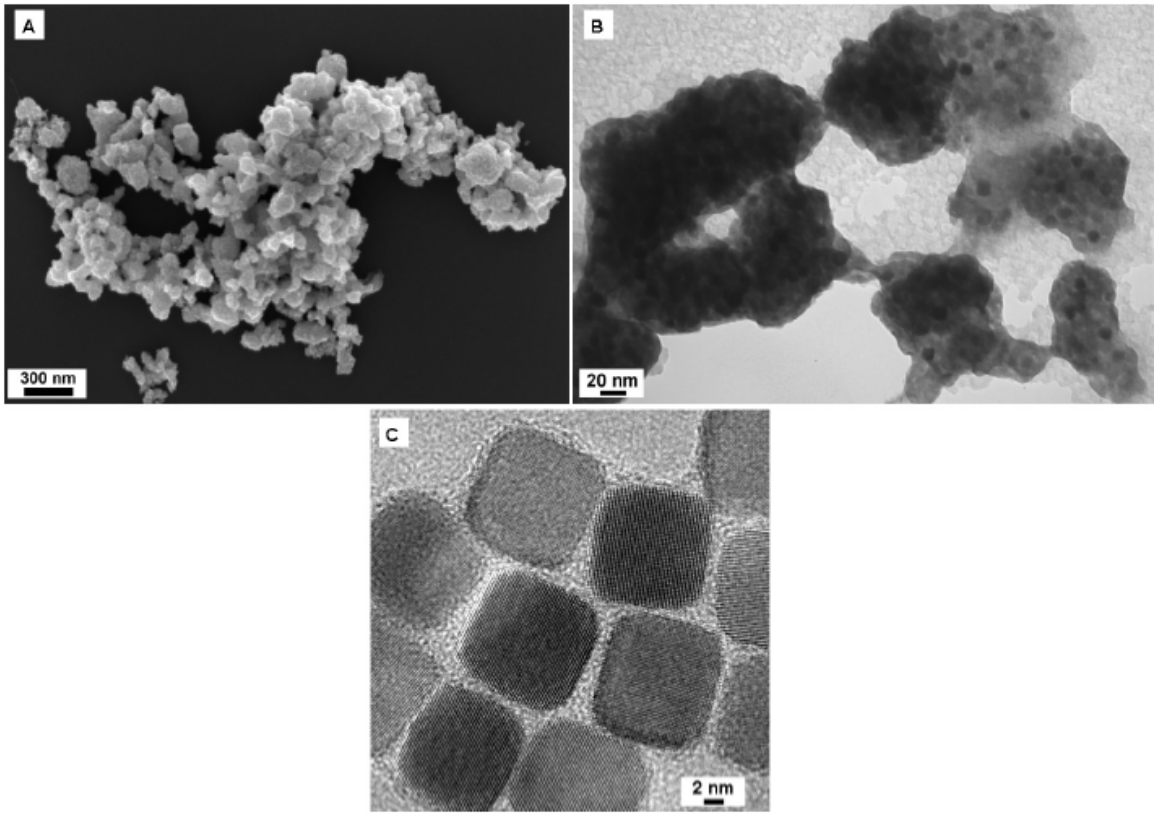

Figure 3.3. Representative SEM (a) and bight-field TEM (b) image of galena nanoparticle aggregates. (c) High-resolution TEM image of the nanoscale interparticle spacing in a nanoparticle cluster.

Appendix B - Size/shape-property relationships of non-carbonaceous inorganic nanoparticles: Towards an understanding of environmental implications

Deborah M. Aruguete*, Juan Liu, and Michael F. Hochella, Jr.

Department of Geosciences, Virginia Tech, Blacksburg, VA 24060, USA

IN PRESS
Environmental and Human Health Impacts of Nanotechnology

*corresponding author

Table of contents – Appendix B

1. Introduction 70
2. Inorganic nanoparticle anatomy 70
3. Redox chemistry of nanoparticles 71
3.1 Photoredox chemistry in semiconductor nanoparticles 72
3.2 Redox chemistry in other nanoparticle systems 74
3.2.1. Precious-metal nanoparticles 74
3.2.2. Zerovalent iron and iron oxides 75
4. Size effects in nanoparticle sorption processes 78
5. Nanoparticle fate: dissolution and solid-state cation movement 80
5.1. Basic energetic and kinetic considerations of nanoparticle dissolution 80
5.2. Effects of nanoparticle morphology 83
5.3 Effects of nanoparticle coatings and external substances 83
5.4 Case study: the dissolution of PbS nanoparticles 84
5.5. Solid-state cation movement in nanoparticles 86
6. Effect of nanoparticle aggregation on physical and chemical properties 88
7. Recommendations and outlook in gaining more understanding of environmental implications of nanoparticles 89
Acknowledgements 92
References 102

Table of figures – Appendix B

Figure B. 1. Flow diagram displaying variables in the "anatomy" of a colloidal inorganic nanoparticle……94

Figure B. 2. Position of the conduction and valence band edges versus the normal hydrogen electrode (NHE) for bulk and nanoparticulate MoS_2, plus redox potentials for environmentally- or biologically-relevant half reactions. Note that by varying size, the redox properties of MoS_2 are altered. For example, photoexcited 4.5 nm MoS_2 nanoparticles have holes with a redox potential more positive than 1.2-1.5 V, which means these holes can oxidize water and create hydroxyl radicals. The hydroxyl radicals can then degrade organic chemicals or potentially cause oxidative damage in biological systems. Also displayed are redox potentials for the carboxylation of acetate to pyruvate and for the reduction of AQDS, a synthetic analog of electron shuttle molecules important for bacterial respiration. Adapted with permission from T.R. Thurston and J.P. Wilcoxon (1999), Photooxidation of organic chemicals catalyzed by nanoscale MoS_2; Journal of Physical Chemistry B, 103, 11-17. Copyright (1999) American Chemical Society……....95

Figure B. 3. A. Schematic of valence and conduction band edges in a CdSe nanoparticle and their energetic alignment with a molecular ligand coating the particle. Mobile charge carriers (the hole and electron) are generated when a photon is absorbed by the nanoparticle, as shown. Holes can be transferred to the highest occupied molecular orbital (HOMO) of the ligand. Adapted from D.J. Milliron, A.P. Alivisatos, C. Pitois, C. Edder and J.M.J. Frechet (2003), Electroactive Surfactant Designed to Mediate Electron Transfer Between CdSe Nanocrystals and Organic Semiconductors; Advanced Materials, 15, 58-61. Copyright Wiley-VCH Verlag GmbH & Co. KGaA. Reproduced with permission. B. Schematic of a CdSe-ZnS core-shell nanoparticle and the corresponding band edges of the core and the shell. Adapted from B.O. Dabbousi, J. Rodriguez Viejo, F.V. Mikulec, J.R. Heine, H. Mattoussi, R. Ober, K.F. Jensen, and M.G. Bawendi, (1997), (CdSe)ZnS core-shell quantum dots: synthesis and characterization of a size series of highly luminescent nanocrystallites; Journal of Physical Chemistry B, 101, 9463-9475. Copyright (1997) American Chemical Society……..96

Figure B. 4. The deviation of the solubility of small grains of quartz relative to its bulk solubility (S/S_0) as a function of the size of the quartz grains being dissolved according to Eq. B. 2. The following values were used to produce this curve: T= 298 K, $\overline{V}$ = 22.68 $x10^{-6}$ m^3/mol, γ= 350 mJ/m^2. At a particle radius of 100 nm, the solubility is indistinguishable from the bulk value. By the time the particle radius is reduced to 1 nm, the predicted solubility is nearly three orders of magnitude higher. Reprinted from Earth and Planetary Science Letters, 203, M.F. Hochella, Jr., Nanoscience and technology: the next revolution in the Earth Sciences, Pages 593-605, Copyright (2002), with permission from Elsevier……..97

Figure B. 5. Reaction coordinate for the partial dissolution (etching) of a truncated cubooctahedral nanoparticle. For this system, the thermodynamically-favoured product is a spherical nanoparticle. In the absence of stabilizing coatings or ligands, formation of a spherical nanoparticle is kinetically favoured as well (the activation energy $\Delta G^{\dagger}_{nostab} < \Delta G^{\dagger}_{111}$). In the presence of compounds that stabilize the {100} and {110} faces, the activation energy to obtain a spherical nanoparticle increases. In this case, since this activation energy is greater than that necessary to form an octahedron (energy $\Delta G^{\dagger}_{stab} > \Delta G^{\dagger}_{111}$), formation of a sphere is no longer kinetically favoured. Etching the non-stabilized {111} faces is kinetically favoured. In the absence of enough thermal energy in the system, etching will result in an octahedral endproduct rather than a spherical one. Figure adapted from Y.W. Jun, J.S. Choi, and J.W. Cheon (2006), Shape control of semiconductor and metal oxide nanocrystals through nonhydrolytical colloidal routes; Angewandte Chemie, 45, 3414-3439. Copyright Wiley-VCH Verlag GmbH & Co. KGaA. Reproduced with permission……..…98

Figure B. 6. A. HRTEM images of a nanoparticle before dissolution (left) and a nanoparticle after 2 hours of dissolution (right). Note how the size of the {110} faces have increased. B. Schematic diagrams of the distances measured on particles to determine whether the change in {110} size is statistically significant. C. Distance ratios of d_{100}/d_{110} before and after dissolution, along with mean values and 95% confidence intervals. As the {110} face size increases after 2 hours of dissolution, the value of the ratio increases. Data in C. from Liu et.al. (2007)……..99

Figure B. 7. TEM images of (**A**) initial CdSe (diameter 4.2 nm), (**B**) Ag_2Se transformed from the forward cation exchange reaction, and (**C**) recovered CdSe nanocrystals from the reverse cation exchange reaction. (**D** to **F**) XRD patterns, fluorescence emission, and optical absorption spectra of initial CdSe (top diffractogram or spectrum), Ag_2Se (middle), and recovered CdSe (bottom) nanocrystals, respectively. In the recovered CdSe, the peak positions of the emission and absorption show a slight redshift from those of the initial CdSe, which becomes negligible for nanospheres larger than 6 nm in diameter. An additional fluorescence emission feature near 700 nm seen in the recovered CdSe (E) is due to the increased surface trap emission. Vertical lines in (E) and (F) are a guide for the comparison of peak positions. Figure and caption from D.H. Son, S.M. Hughes, Y.D. Yin, and A.P. Alivisatos (2004), Cation exchange reactions in ionic nanocrystals; Science, 306, 1009-1012. Reprinted with permission from AAAS…….100

Figure B. 8. Examples of shape change after cation exchange reactions. A and B: Conversion of nanorods to nanospheres when exchanging Ag for Cd. C and D: Conversion of solid cobalt nanospheres to hollow cobalt sulphide nanospheres, due to rapid diffusion of Co ions**.** A and B from D.H. Son, S.M. Hughes, Y.D. Yin, and A.P. Alivisatos (2004), Cation exchange reactions in ionic nanocrystals; Science, 306, 1009-1012. C and D from Y.D. Yin, R.M. Rioux, C.K. Erdonmez, S.M. Hughes, G.A. Somorjai, and A.P. Alivisatos (2004), Formation of hollow nanocrystals through the nanoscale Kirkendall effect, Science, 304, 711-714. Reprinted with permission from AAAS……...101

List of Tables – Appendix B

Table B.1. Summary of particle size-dependence adsorption studies……..93

1. Introduction

Non-carbonaceous inorganic nanoparticles, with dimensions from 1-100 nm, form one of the major classes of emerging synthetic nanomaterials. Such nanoparticles are already commercially used in products such as sunscreens, pigments, and anti-bacterial coatings and continue to be heavily researched for other applications. The environment is already being exposed to these nanoparticles, and this exposure will increase as more applications are developed.

Most nanoscience studies have been conducted under non-environmentally-relevant conditions, and, as a result, there is a dearth of data on the environmental fate and behaviour of inorganic nanoparticles; such data are what scientists and engineers need to predict the environmental impact of the nanoparticles. In many cases, environmentally relevant data may be available for their bulk counterparts (solids, generally larger particles, with dimensions > 100 nm). For example, environmentally relevant data for bulk titanium dioxide is much more abundant than for nanoparticles of the same material. However, scientists have made it clear that many of these nanoparticles have size- (and sometimes shape-) dependent properties which can be radically different from those of their bulk corresponding materials. Understanding the size-dependent differences between bulk and nanoscale properties is important for shaping future experiments in environmental nanoscience, as well as for the design of well-informed nanotechnology legislation.

In this review, we attempt to link what is currently known about the size-dependent behaviour of inorganic nanoparticles and how this knowledge might apply in environmental or natural systems. We review size and shape effects upon redox chemistry, sorption processes, and dissolution, and suggest what sorts of future studies are necessary to answer the following question:

How will nanoparticles behave differently from their bulk counterparts, and what might their environmental fate and impact be?

2. Inorganic nanoparticle anatomy

In environmental nanoscience, it is critical to understand that nanoparticles can display an astoundingly broad range of physical and chemical properties. This variety of properties generally results from differences in structure and composition between different nanoparticles. Therefore, to understand the behaviour of any given type of nanoparticle, one must know its structural and chemical characteristics.

We briefly review these characteristics here for inorganic nanoparticles. Commercial nanoparticles are composed of a core material and often a coating (although this is optional), as shown in Fig. B. 1. This core material can in theory be any solid inorganic substance, although those most under development for applications include metals (Au, Ag, Pd, and Pt) and semiconductors/insulators (metal sulphides, selenides, and oxides). The core material can vary in both size and shape and confers many of the nanoparticle's basic physical characteristics (*e.g.* optical and magnetic properties). Possible coatings include small molecular moieties (*e.g.* alkylthiols) (Kloepfer et al., 2005), polymers (Harris et al., 2003), biomolecules (Gao et al., 2005; Nie et al., 2007; Rhyner et al., 2006), and inorganic coatings (*e.g.* a ZnS film on a CdSe nanoparticle) (Dabbousi et al., 1997; Hines and Guyot-Sionnest, 1996). Such coatings commonly affect important nanoparticle properties, such as solubility in water (Pellegrino et al., 2004), resistance to chemical degradation (*e.g.* passivation of a particle to prevent oxidation) (Yu et al., 2007), and affinity for different biological tissues (Bruchez et al., 1998). The specific chemical behaviour of any given nanoparticle will depend strongly upon the core material composition, the size, the shape, the coating, and the aggregation state. As a part of nanotechnology products or devices, nanoparticles may be embedded in a particular matrix or on a substrate which can also influence nanoparticle behaviour.

The effects of matrices or substrates upon nanoparticle environmental behaviour merit more study, although it is still critical to understand the properties of the individual nanoparticles. The behaviour of the individual nanoparticles is likely to affect the properties of any composite material. Also, in the case of chemically- or biologically-labile matrices/substrates, "plain" nanoparticles may be released from the composite material.

3. Redox chemistry of nanoparticles

In nature, redox reactions are an important part of phenomena such as mineral weathering, bacterial respiration, and degradation of pollutants. Many nanoparticles are of interest for applications due to their ability to catalyze or directly participate in redox processes. Thus, if released into the environment, such nanoparticles may influence natural redox phenomena, including those within living organisms. Here we discuss the varied origin and nature of redox properties in nanoparticles.

3.1 Photoredox chemistry in semiconductor nanoparticles

When semiconductor materials absorb light of the proper energy, mobile charge carriers (electrons and holes) can be generated. If these charge carriers reach the surface of the semiconductor material, they may reduce or oxidize compounds on or near the surface, depending upon the redox potentials of the compounds. The size of the semiconductor material can affect many aspects of such redox processes.

Generally, if a semiconductor nanoparticle is below a certain critical size (which depends upon the parent semiconductor material), it can exhibit quantum size effects (Alivisatos, 1996). In such cases, the wavefunctions of the charge carriers extend over the entire particle. Therefore, the charge carriers will not have to diffuse to participate in reactions at the particle surface (Hagfeldt and Gratzel, 1995).

Quantum size effects result in the shifting of band edge energies (changes in electronic energy levels) (Alivisatos, 1996). This alters the redox potentials of charge carriers in a given nanoparticle with respect to the bulk. Therefore, a nanoparticle may be energetically able to participate in a particular redox reaction that is not possible for the corresponding bulk material. An excellent example of this phenomenon is provided by nanosized MoS_2 (Abrams and Wilcoxon, 2005; Thurston and Wilcoxon, 1999). In Fig. B. 2, the redox potential positions of the valence and conduction bands of bulk and nanoparticulate MoS_2 are shown. For comparison, the redox potentials of some environmentally- or biologically-relevant half reactions are included. These reactions include the generation of hydroxyl radicals (•OH) from H_2O. Hydroxyl radicals can play a major role in oxidative damage in biological systems (Imlay, 2003; Sayre et al., 2008),

as well as the degradation of organic compounds (Kamat and Meisel, 2002; Wilcoxon, 2000). Also included are the reduction of AQDS (9, 10-anthraquinone-2, 6-disulfonic acid) (Sund et al., 2007), a synthetic analog of electron-shuttling molecules used in bacterial respiration, and the reduction (carboxylation) of acetate to pyruvate (Becker and Deamer, 1986).

Size effects in the photocatalytic activity of MoS_2 have been demonstrated. It was shown that smaller MoS_2 nanoparticles (4.5 nm and below) could photocatalyze redox reactions that would degrade organic molecules, while larger nanoparticles (8-10 nm) could not (Abrams and Wilcoxon, 2005; Thurston and Wilcoxon, 1999; Wilcoxon, 2000). Results suggested that the size dependence of photocatalytic activity was due to the higher redox potential of the holes (see Fig. B. 2) in the smaller nanoparticles, which in turn could oxidize water and create reactive hydroxyl radicals.

Altering redox potentials in nanoparticles can also change other aspects of redox processes; in CdS nanoparticles, nitrate reduction rates were found to increase with decreased particle size (Korgel and Monbouquette, 1997). As kinetic phenomena can be important for many geochemical processes (Lasaga, 1998), such effects may alter the geochemical impact of nanoparticles.

We emphasize that not every type of semiconductor nanoparticle displays quantum size effects. Their manifestation depends both upon the composition of the nanoparticle and its size. Interestingly enough, even in the absence of quantum size effects, nanoparticle size may affect the kinetics of redox processes. For example, size can alter the average transit time for a charge carrier to diffuse from a nanoparticle's interior to its surface (Hagfeldt and Gratzel, 1995).

The redox reactivity of an inorganic semiconductor nanoparticle is not only determined by its core material, but its coatings. Some coatings may enhance charge carrier transport out of the nanoparticle. For example, an electroactive ligand coating was developed for CdSe nanoparticles to improve their performance in electronic devices, such as photovoltaic cells (Milliron et al., 2003). The energy level alignment of the ligand coating molecules with the band edges of the CdSe nanoparticles favoured the transfer of charge carriers (holes) from photoexcited CdSe nanoparticles to the ligands. Adding a layer of ZnS onto CdSe, on the other hand, can help to confine charge carriers, because of

the energetic positions of ZnS band edges with respect to those of CdSe (Dabbousi et al., 1997; Hines and Guyot-Sionnest, 1996). Fig. B. 3 displays energy level schematics for such systems. It is evident that coatings must be considered carefully when predicting the environmental chemistry of a nanoparticle.

3.2 Redox chemistry in other nanoparticle systems

3.2.1. Precious-metal nanoparticles

The properties and applications of precious-metal nanoparticles (Au, Ag, Pt, and Pd) are a very popular subject of study in nanoscience; materials such as Pt have long been utilized for commercial catalysis. Here we will focus upon gold as our primary example, as its behaviour arguably has many commonalities with other precious-metal nanoparticles. Nanoparticulate gold is also particularly relevant as it is popular for application in nanomedicine, biolabeling, and sensing (El-Sayed et al., 2007; El-Sayed et al., 2005; Hayat, 1989; Huang et al., 2007a; Huang et al., 2006; Huang et al., 2007b; Oyelere et al., 2007; Sonnichsen and Alivisatos, 2005).

Unlike materials such as platinum, gold in bulk form is chemically fairly inert. Nevertheless, in nanoparticulate form, it can display significant catalytic activity, both in solution and on solid supports. Gold nanoparticles can participate in many redox reactions. These include reactions of potential environmental interest, such as the oxidation of carbon monoxide (Ketchie et al., 2007; Valden et al., 1998) and the degradation of organic pollutants (Deng et al., 2005; Deng et al., 2007; Panigrahi et al., 2007). Precious-metal nanoparticles can behave as electron transfer mediators between molecules or other species (*e.g.* between semiconductor nanocrystals and molecules) (Cozzoli et al., 2004; Kiwi and Gratzel, 1979; Miller et al., 1981). Some reported reaction rates (Deng et al., 2007; Ketchie et al., 2007) are comparable to the rates for reactions promoted by commonly studied platinum catalysts (Somorjai, 1994).

Size dependence of catalytic redox behaviour has been observed in colloidal gold reactions in aqueous solutions. Reports of such behaviour in the literature vary widely. For example, Sau and co-workers examined the gold nanoparticle catalysis of eosin dye reduction with $NaBH_4$, and found two distinct size dependence regimes (Sau et al., 2001).

Surface area-normalized rates decreased for nanoparticle diameters from 10-15 nm, then increased from 15 nm to 46 nm. In a different study monitoring the hydrogenation of anthracene, a polycyclic aromatic hydrocarbon pollutant, nanoparticles ranging from 4.1 nm – 24.7 nm displayed an increasing turnover frequency (number of anthracenes reduced per surface atom per second) with decreasing size (Deng et al., 2005; Deng et al., 2007). Similar variation in catalytic redox properties has been observed for other gold and precious-metal nanoparticle systems (Deng et al., 2005; Deng et al., 2007; Duan et al., 2007; Sharma et al., 2003).

The reported variation in size-dependent properties complicates attempts to predict the behaviour of precious metal nanoparticles in the environment. Nevertheless, additional studies can potentially rectify this problem. Studies on platinum nanoparticle catalysis indicate that nanoparticle morphology could be important in determining reaction rates (Narayanan and El-Sayed, 2005). In the aforementioned studies on colloidal precious-metal nanoparticle catalysis, mostly size characterization is reported. It is possible that preparations leading to batches with different particle sizes also yield slightly different morphologies; thus some of the variation in catalytic activity attributed to size effects might actually be due to differences in particle shape. Hence, future studies of catalytic behaviour should include more control and characterization of morphology. Also, from study to study, and even within studies, the surface coatings vary, which may strongly affect the catalytic properties. More systematic comparisons of the catalytic properties of nanoparticles with different coatings would be very helpful. It will also be important to better understand how the effect of size upon a redox reaction depends upon the particular energetics of that system.

3.2.2. Zerovalent iron and iron oxides

3.2.2.1. *Iron*

For years, zerovalent iron (ZVI), or metallic iron, has been studied for the remediation of groundwater systems (Lo et al., 2007). As the standard reduction potential for the (Fe/Fe^{2+}) redox reaction is -0.44 V (Atkins, 1998), metallic iron is able to reduce and transform many substances, including Cr^{6+}, Pb^{2+}, and halogenated organic pollutants.

Nanoparticulate ZVI or nZVI (including mixtures of nZVI plus an activating metal, *e.g.* Pd) have been investigated for use in environmental clean-up efforts (Schrick et al., 2002; Tratnyek and Johnson, 2006; Zhang, 2003; Zhang et al., 1998). nZVI is attractive for this application due to its higher specific surface area, as ZVI reductive transformation rates have been shown to be proportional to surface area (Johnson et al., 1996). Also, nZVI can be directly injected into contaminated sites, allowing for flexibility in its application (Li et al., 2006a; Li et al., 2006c).

Those interested in optimizing the performance of nZVI have begun to examine how physical characteristics such as nanoparticle size affect reactivity. Results have varied. For example, nZVI has been shown to reduce polychlorinated biphenyls (Lowry and Johnson, 2004), while microscale ZVI cannot. However, size effects (independent of surface area) are not always as pronounced. For example, in another study on the reduction of nitrate, surface area-normalized rate constants for 9.5 nm and 45 nm nanoparticles did not even vary by an order of magnitude (Liou et al., 2006). Various nZVI preparations have been shown to alter which products result from the reductive transformations of halogenated organics (Liu et al., 2005a; Liu et al., 2005b; Nurmi et al., 2005). In the reduction of carbon tetrachloride, two different preparations of nZVI and microscale ZVI produced different amounts of chloroform, an undesirable product (Nurmi et al., 2005). Such findings are significant, as they mean the chemical behaviour of nZVI might be controlled by merely altering the preparation used.

The origins of nZVI chemical behaviour have not yet been exactly determined, although various studies suggest differences in crystallinity (Liu et al., 2005a) and the amount of oxides or other elements present (Liu et al., 2005b; Nurmi et al., 2005) may be important. The Fe nanoparticle sizes used are far too large to have electronic structures significantly different from the bulk, so this is an unlikely cause of their differences in behaviour (Wang et al., 2000). One possible factor influencing the reactivity of nZVI would be nanoparticle shape and surface bonding coordination. Future studies of nZVI could utilize samples of higher uniformity in shape and size.

nZVI can effectively decompose pollutants *in situ*, as demonstrated with multiple field tests in which nZVI was directly introduced to the environment (Elliott and Zhang, 2001; Li et al., 2006c; Quinn et al., 2005; Zhang, 2003). Given this success, use of nZVI

for remediation may become more widespread. Thus, it is particularly important to consider its potential environmental effects. A recent study showed that humic acids can sorb strongly onto nZVI and even react with it, removing humic acid from solution (Giasuddin et al., 2007). While nZVI may be used with the best of intentions for remediation, it may have unintended consequences.

3.2.2.2. *Iron oxides*

It is already well-established that iron oxides, including hydroxides and oxyhydroxides, play an important role in the environment. Both macro- and nanoscaled iron oxides are naturally present in the environment and involved in multiple chemical and transport processes (Brown et al., 1999; Cornell and Schwertmann, 2003; Davison and De Vitre, 1992; Dzombak and Morel, 1990). It is therefore likely that synthetic iron oxides could influence the environment as well, if released in sufficient quantities.

Iron oxides are of interest for various nanotechnologies, not only because of their intrinsic properties, but also because of their low cost and low toxicity. Nanoscale iron oxides have been studied for applications such as magnetic resonance imaging contrast enhancement (Lee et al., 2006), hydrogen generation (Vayssieres et al., 2005) and catalysis (Halim et al., 2007; Liu et al., 2007b; Tsodikov et al., 2005). In addition to being synthesized for applications in their own right, nanoscaled iron oxides are also present in preparations of nZVI (Li et al., 2006a; Liu et al., 2005a; Martin et al., 2008; Nurmi et al., 2005).

As with their bulk counterparts, nanoscale iron oxides are known to be redox active. In particular, there are multiple examples of nanoscale iron (III) oxide reduction by organic molecules (Houben, 2003; Larsen and Postma, 2001; Roden, 2003; Torrent et al., 1987). This includes molecules such as hydroquinone, a synthetic analogue of biological electron transfer molecules (Anschutz and Penn, 2005). Iron (III) oxides can also participate in redox biochemistry as electron receptors for bacteria respiring under anaerobic conditions (Roden, 2003; Roden and Zachara, 1996).

As well as participating directly in redox reactions, nanoscale iron oxides can act as catalysts in low-temperature systems. One reaction that multiple types of iron oxide

nanoparticles (Fe_3O_4, ferrihydrite, α-Fe_2O_3) can catalyze is the decomposition of hydrogen peroxide, which can be useful for oxidizing and degrading organic pollutants in water (Filip et al., 2007; Gao et al., 2007; Hermanek et al., 2007; Zelmanov and Semiat, 2008). This catalytic activity may have significance in biological systems, as it mimics the enzyme activity of peroxidases (Gao et al., 2007). Another reaction of environmental importance that can be catalyzed (photocatalyzed) is the oxidation of sulfite (Faust et al., 1989).

The effect of size upon the redox reactivity of iron oxides is still not well-established. While a number of studies have examined the effect of varying particle surface area (or size) on reaction rates, results from studies vary (Gao et al., 2007; Houben, 2003; Larsen and Postma, 2001; Liu et al., 2006; Roden, 2003; Schwertmann et al., 1985; Torrent et al., 1987). The interpretation of results from these studies is often complicated by variation in iron oxide phase amongst samples of different sizes. Further studies are needed to specifically examine whether there are any intrinsic size-dependent effects present in iron oxide nanoparticles of the same phase, independent of surface area. One example of such a study concerns the oxidation rate of Mn^{2+} to Mn^{3+} by different sizes of α-Fe_2O_3 (hematite) (Madden and Hochella, 2005). Surface-normalized oxidation rates showed that 7 nm platelets catalyzed this oxidation over an order of magnitude more quickly than 37 nm platelets. It was suggested that the change in oxidation rate could be due to the increased Lewis basicity of surface oxygens on the smaller particles (Noguera et al., 2002). The increased electron-donating capacity could in turn decrease the redox potential of adsorbed Mn to make Mn oxidation more energetically favourable. Another likely cause suggested for the catalytic effect was altered geometry of Mn sorptive complexes, depending upon size. This change could decrease kinetic energy barriers for the electron transfer process, promoting oxidation.

4. Size effects in nanoparticle sorption processes

In nature, the sorption of metals and organics to inorganic surfaces (mineral surfaces) can greatly influence their mobility (Hochella et al., 2008; Kretzschmar and Schafer, 2005). As inorganic nanoparticles offer a large amount of surface area relative to

their volume or weight, it is expected that they would participate in sorption phenomena. Indeed, heavy metals and radionuclides have been found associated with nanoscale colloids in natural water (Hochella et al., 2005a; Hochella and Madden, 2005; Hochella et al., 2004; Hochella et al., 2005b; Kersting et al., 1999) and drinking water (Wigginton et al., 2007). The sorptive properties of nanoparticles have caught the attention of chemists and engineers, who are interested in using them for environmental remediation (Jeong et al., 2007; Yavuz et al., 2006; Yuan, 2004).

Predicting the sorption behaviour of nanoparticles is of interest when considering both natural nanoparticles and the accidental or purposeful release of synthetic nanoparticles into natural systems. Studies have shown that on a per-mass basis, nanoparticles sorb more than their bulk counterparts, as one would expect based upon surface area (Gao et al., 2004; Giammar et al., 2007; Waychunas et al., 2005; Yean et al., 2005). Also, other size effects (independent of surface area) are expected for nanoparticle sorption. Experiments have shown that for nanoparticulate TiO_2 and α-Fe_2O_3, the point of zero charge, or the pH at which the particles have zero charge, is shifted with respect to size (Guzman et al., 2006; He et al., 2008). The surface energy of nanoparticles is likely to vary with size (Zhang et al., 1999). Also, nanoparticle structures are often different from those of the bulk, displaying lowered atomic coordination and higher disorder (Aruguete et al., 2007; Hamad et al., 1999; Marcus et al., 1991; Rockenberger et al., 1997; Rockenberger et al., 1998); different crystalline phases may be favoured in the nanoscale as opposed to the bulk (Dinega and Bawendi, 1999). All of these phenomena could presumably alter sorption capacity and affinity.

Studies of sorption size-dependence show varying results. Examples of these are summarized in Table B.1. Many of these studies have fit their data to the Langmuir adsorption equation (Drever, 1997; McBride, 1994), which is

$$\Gamma = \Gamma_{\max} \frac{K_{ads} C}{1 + K_{ads} C} \qquad \text{(B. 1)}$$

where C is the activity (effective concentration) of the adsorbate in solution, K_{ads} is the adsorption equilibrium constant (related to the free energy change for the adsorption reaction), Γ is the number of molecules/ions sorbed per unit area, and $\Gamma_{\max}$ is the adsorption capacity (the maximum number of molecules/ions per unit area that can be

adsorbed). We refer to these parameters in the studies when applicable. (It should be noted that the Langmuir adsorption equation describes adsorption on a homogeneous surface. Because nanoparticle surfaces are heterogeneous by their very nature, parameters derived using this model should be interpreted with caution.)

As with many studies in the emerging field of nano-environmental science, interpretation of the results for size-dependent trends is complicated by variation within and/or among the samples. The samples often not only varied in size, but also in morphology, aggregation state, and even crystal phase. All of these variables can affect particle behaviour. While one can account for these added variables via careful characterization, it is not always simple to do, and in some cases may be impossible. As synthetic methods advance further, it should become easier to synthesize or purchase more homogeneous and well-characterised nanoparticle samples, and the results from such studies should become easier to interpret and compare.

5. Nanoparticle fate: dissolution and solid-state cation movement

Currently, the fate and degradation pathways of nanoparticles are unknown. One possible fate for nanoparticles is for them to dissolve. As many nanoparticles may contain toxic metals, this is a matter of concern. Here, we shall discuss what is known about nanoparticle dissolution, especially with respect to size and shape. Solid-state cation movement and exchange processes are discussed as well, as these may also alter nanoparticle fate in the environment.

5.1. Basic energetic and kinetic considerations of nanoparticle dissolution

Classically, the dependence of solubility upon particle size, assuming a spherical particle, can be expressed with a modified form of the Kelvin equation (Adamson, 1982),

$$\frac{S}{S_0} = \exp\left[\frac{2\gamma \overline{V}}{RTr}\right] \qquad \text{(B. 2)}$$

where S is the solubility of particles with inscribed radius r in m, S_0 is the solubility of the bulk material, γ is the surface free energy in mJ/m^2, R is the gas constant in nJ/mol·K, T is the temperature in K, and $\overline{V}$ is the molecular volume in m^3/mol. According to this relation, as the particle dimensions decrease, the solubility increases exponentially relative to the bulk solubility. An example of this relation is shown in Fig. B. 4, which is a plot of $\frac{S}{S_0}$ versus particle radius assuming γ and $\overline{V}$ values for quartz (Hochella, 2002).

Dissolution is generally assumed to be a spontaneous process. As long as particles are in a solution of constant undersaturation, the rate of dissolution should be constant. The relation of the normalized dissolution rate (in mol•m^{-2}•min^{-1}), R, has been empirically related to the undersaturation, σ, via the relation

$$R = k\,\sigma^n \qquad \text{(B. 3)}$$

where k is the rate constant and n is the effective reaction order (Budz and Nancollas, 1988; Zhang and Nancollas, 1990).

From these models of dissolution and solubility, we would expect smaller nanoparticles to dissolve more quickly than larger particles, and to dissolve to completion. For a number of systems, including nanoparticles of titanium dioxide (Schmidt and Vogelsberger, 2006), silica (Roelofs and Vogelsberger, 2004), and zinc oxide (Yang and Xie, 2006), smaller nanoparticles have been observed to dissolve more quickly than larger nanoparticles. Despite this, it is not always clear whether these models apply to all nanoparticulate systems. In some systems, chemical processes not included in these models, such as photocatalyzed oxidation, may affect dissolution (Aldana et al., 2001; Stouwdam et al., 2007).

Other experimental results indicate that small size does not always result in higher rates of dissolution. In one study of zinc oxides in aqueous systems, the same masses of nanoparticulate and bulk ZnO dissolved at similar rates (non-surface area-normalized), even though the increased surface area and smaller size of the nanoparticles would warrant otherwise (Franklin et al., 2007). On the other hand, the nanoparticles in the experiment were highly aggregated, which may have lessened surface or size-related effects.

In some cases, dissolution at the nanoscale may be slower. Indeed, studies on various calcium phosphate minerals (Tang et al., 2005; Tang and Nancollas, 2002; Tang et al., 2001; Tang et al., 2003; Tang et al., 2004a; Tang et al., 2004b; Tang et al., 2004c) display a phenomenon of self-inhibited dissolution occurring primarily at the nanoscale, in which dissolution rates dwindle over time.

In order to understand one of the means by which inhibited dissolution is possible, it is useful to consider the opposite process of nanoparticle growth from a solution. The energy of particle formation ΔG_{form}, can be expressed as

$$\Delta G_{form} = \Delta G_v + \Delta G_s \qquad \text{(B. 4)}$$

where ΔG_v is the negative energy term describing the spontaneous tendency of solute to precipitate as part of a solid particle, and ΔG_s describes the excess free energy to form a new solid-liquid interface. ΔG_v depends upon the degree of saturation of the solvent. Assuming a spherical particle morphology, both energy terms are functions of *r*, the radius of the particle. For a given level of saturation, there is a critical radius *r**, above which the magnitude of ΔG_v will be greater than that of ΔG_s, and a particle can form (McDonald, 1962; Tang et al., 2001).

An analogous critical radius is believed to exist for dissolution processes. In dissolution, which occurs in an undersaturated solution, there is a favourable energetic driving force for units of the solid particle to become solute. However, the formation of etch pits can increase the area of the solid-liquid interface, which is energetically disfavoured. For such a system, there is a critical radius (of etch pit) at which dissolution is energetically allowed. Below this radius, dissolution is inhibited. Such inhibition phenomena have been observed in a number of systems and particularly well-studied for various biologically-relevant calcium phosphates (Tang et al., 2005; Tang and Nancollas, 2002; Tang et al., 2003; Tang et al., 2004a; Tang et al., 2004b; Tang et al., 2004c). It is therefore reasonable to expect the possibility of such inhibited dissolution occurring for nanoparticles of sparingly soluble compounds, because the nanoparticle dimensions may be below this critical radius. Currently, there are few data to confirm or disprove these expectations.

5.2. Effects of nanoparticle morphology

Nanoparticles released into the environment will not only vary in size, but in their morphology, which may strongly affect dissolution. This particularly applies to cases in which the nanoparticles are crystalline. When nanoparticles of the same crystalline substance assume different shapes, this generally means that different crystal faces comprise their surfaces. For example, consider nanoparticles of a rocksalt structured mineral. A cubic nanoparticle displays {100} faces, a truncated cubooctahedron displays {100}, {111} and {110} faces, and an octahedral nanoparticle will display {111} faces. Different crystal faces will be more or less stable (have different surface energies), depending upon their surface bonding. It is expected that less stable faces would be etched more readily than more stable faces. In our example, assuming that all other conditions were equal (same crystal structure, composition, solution undersaturation, etc.), this would mean that the three differently-shaped nanoparticles might dissolve at different rates. While the energetic stability of crystal surfaces affects dissolving crystals of all sizes, it is particularly important for nanoparticles because even minimal dissolution may result in their annihilation.

In principle these concepts are simple, but applying them to quantitatively predict morphology-dependent dissolution trends in nanoparticles is difficult. This is because little is known regarding the relative stabilities of nanoscale surfaces. The presence of surface defects, steps, or kinks, which may be more evident on nanoparticle surfaces, will also influence the energetics of dissolution. Another complicating factor is the presence of coatings or other external substances, which we discuss in the following section.

5.3 Effects of nanoparticle coatings and external substances

As with the surfaces of bulk materials (Becker et al., 2005; Casey and Ludwig, 1995; Zhang and Nancollas, 1990), it has been shown that external substances, particularly those that can coordinate to nanoparticle surfaces, can strongly influence nanoparticle growth and dissolution (Jun et al., 2006; Li et al., 2005; Li et al., 2006b; Yin and Alivisatos, 2005). Anthropogenic nanoparticles released into the environment are

likely to encounter many substances that could interact strongly with or sorb onto their surfaces, and many will already have coatings on their surfaces.

One way such coatings or sorbed species may affect dissolution is by stabilizing particular crystal surfaces. Consider the partial dissolution of a truncated cubooctahedral nanoparticle composed of the rocksalt-structured material introduced in section 5.2. Fig. B. 5 displays the reaction coordinate for this process. Thermodynamically, the most favored end product of dissolution for this system is a sphere. (This is not to imply that a sphere is always the most favored shape for every system.) Imagine now adding a substance to the solution of nanoparticles which binds to and stabilizes the {100} and {110} crystal faces. This will increase the activation energy needed to obtain a spherical nanoparticle. Unless there is enough thermal energy in the system to surmount this kinetic barrier, it is likely that the process with the lower kinetic barrier (lower activation energy) will dominate. In this scenario, the {111} faces are energetically unstable relative to the other faces, so they will etch more readily. This etching results in an octahedrally-shaped particle rather than a spherical particle.

Coatings or external compounds can affect dissolution in other ways. For example, a coating that forms a micellar structure around a nanoparticle might reduce the activity of water at the surface. As for external compounds in the solution surrounding the nanoparticle, there are experimental examples of dissolution rates being increased by compounds such as acetic acid (Meulenkamp, 1998) or human serum albumin protein (Yang and Xie, 2006). External compounds might form stable ionic complexes with the constituent metal ions in the nanoparticle, hence energetically favoring dissolution. They also may alter pH, which again can affect nanoparticle stability.

It is evident from such considerations that in any study concerning nanoparticle dissolution, as much as possible should be known regarding the composition of the coatings or the compounds in the solution surrounding the nanoparticle. These characteristics can be as significant as the composition of the inorganic part of the nanoparticle.

5.4 Case study: the dissolution of PbS nanoparticles

From the previous discussion of nanoparticle dissolution, it is evident that not only is size important, but morphology, coatings, and molecules present in the surrounding solution. Currently, in our laboratory, we are studying the first two factors and present some of our preliminary data here. We are examining the non-oxidative dissolution of ~15 nm diameter PbS nanoparticles in hydrochloric acid (pH 3) (Liu et al., 2007a). Bright-field transmission electron microscopy (TEM) is used to track changes in particle size, and high-resolution TEM is used to measure changes in morphology and structure.

The dissolution of nanosized PbS (galena) may have implications for the behaviour of both synthetic and natural nanomaterials in the environment. PbS is a low band gap semiconductor used in applications such as infrared detectors. Nanoparticles of PbS are popular in nanoscience research and are commercially available. As for natural systems, it is known that nanoparticulate metal sulfides are present in some environments, and that mineral nanoparticles may be involved in the transport of heavy metals (Hochella et al., 2008; Hochella et al., 2004; Hochella et al., 2005b; Labrenz et al., 2000).

PbS nanoparticles are synthesized under inert atmosphere in organic solution with surfactant via a previously published procedure at high temperature (Joo et al., 2003). This synthetic procedure produces monodisperse, highly-crystalline nanoparticles, as confirmed with TEM and X-ray diffraction (XRD). Nanoparticles are washed to remove excess free surfactant. To monitor changes in particle size and morphology with TEM, nanoparticles are deposited onto a onto a carbon/gold TEM grid substrate. Having the particles on a substrate helps to prevent aggregation, as this would complicate analysis. X-ray photoelectron spectroscopy (XPS) confirms that subsequent washing steps remove the majority of the surfactant (although undetectable trace amounts may remain), and that washing does not significantly affect the presence of any oxidation species on the nanoparticle surfaces.

Washed, dried grids are exposed to nitrogen-purged pH 3 HCl solutions under constant stirring for varying periods of time. Images from samples exposed to the acid for different times are compared with each other using TEM measurements. Here, we wish to summarize two interesting trends.

First, the morphology of the PbS nanoparticles changes after dissolution. From high-resolution TEM measurements (Fig. B. 6), the {110} and {111} faces are being etched more quickly than the {100} faces ({111} data not shown). Such results match what might be expected from our knowledge of bulk crystals. Generally, on a crystal face, the rate at which an atom is removed from that face is inversely proportional to the number of bonds it has (Lasaga and Luttge, 2004). Atoms in the ideal bulk {110} and {111} faces have surface atomic coordination numbers of 4 and 3, respectively, while the {100} faces have an atomic coordination number of 5. Therefore, it would be expected that the {100} faces would etch more slowly than the {111} or {110} faces. At least for this system, these results indicate that we can use some of our current knowledge about bulk crystal surfaces to predict how nanoparticles might behave in the environment.

Second, PbS nanoparticles have been found to dissolve one to two orders of magnitude faster, after surface area normalization, than bulk PbS. This difference in dissolution rate may be attributed to the small size of the nanocrystals. As mentioned earlier, the modified Kelvin equation indicates that dissolution is more thermodynamically favored for smaller particles. Also, due to their size, nanocrystals have a larger fraction of their atoms at corners and edges than bulk crystals. Such undercoordinated atoms are more active in dissolution than ones from flat surfaces. Nanoparticle morphology may also play a role in faster dissolution. While bulk natural PbS mostly displays {100} faces, the PbS nanocrystals exhibit {111} and {110} faces. As described above, these faces dissolved more quickly than the {100} faces.

These initial results have important implications for the dissolution behaviour of nanoparticles in the environment. We are currently in the process of synthesizing larger micro-sized particles for further size comparative rate studies.

5.5. Solid-state cation movement in nanoparticles

Another phenomenon that may affect nanoparticle degradation and fate is solid-state cation movement into or out of nanoparticles. One type of cation movement is cation exchange, in which cations in solution replace cations in a lattice. Even if cation exchange does not occur significantly in the bulk form of a particular material (excluding

perhaps on its surfaces), this does not preclude this process from happening fully in the nanoparticulate form or in thin films (nanoscaled films <100 nm in thickness). In the bulk forms of such materials, cation exchange is kinetically controlled by the advancement of a reaction zone, along which cations and vacancies travel. If nanoparticles are small enough, they may be as large as or smaller than this minimum reaction zone, resulting in faster cation exchange (Son et al., 2004).

One fascinating example of this phenomenon is the room-temperature complete exchange of silver ions for cadmium in CdSe nanoparticles. Son et. al. (2004) synthesized spherical CdSe nanoparticles (4.2 nm in diameter) and rod-shaped CdSe nanoparticles (varying dimensions) and mixed them with solutions of $AgNO_3$. (While this was done in a toluene-methanol mixture, it should be noted that cation exchange in nanostructures has also been observed for aqueous systems (Dloczik and Koenenkamp, 2004; Lokhande et al., 1992; Mews et al., 1994). Within ~100 ms (Chan et al., 2007), CdSe nanospheres are transformed into Ag_2Se nanospheres as shown in Fig. B. 7. The exchange could be subsequently reversed by adding an excess of cadmium ions and a compound that forms a stable complex with Ag (tributylphosphine). When the same reaction was attempted with micrometer-sized powders of CdSe, cation exchange was not observed, even over weeks. Cation exchange in this system has also been tested with Pb^{2+} and Cu^{2+}, and has been demonstrated to occur with a variety of ions in metal sulphides in both nanoparticles and thin films (Dloczik and Koenenkamp, 2004; Lokhande et al., 1992; Mews et al., 1994; Robinson et al., 2007).

Another interesting aspect of cation movement in nanoparticles is that the morphology of particles can be altered. As morphology can affect the chemical and physical behaviour of nanoparticles, this has important implications. Two examples are displayed in Fig. B. 8. In the CdSe to Ag_2Se conversion as described above, smaller nanorods are converted to nanospheres. Another example of shape change due to cation diffusion is in the synthesis of cobalt sulphide from metallic cobalt nanospheres (Yin et al., 2006; Yin et al., 2004). When reacting with elemental sulphur, the outward diffusion of cobalt ions produces a hollow nanosphere.

The reader should take note of the fact that such cation movement processes are contingent upon favourable thermodynamic driving forces, as well as factors such as the

rate of diffusion for a particular atom in a given solid lattice. Cation movement will not necessarily occur for every sort of nanoparticle. Nevertheless, as nanoparticles will doubtless encounter metal ions when they are released into natural systems, it is important to keep these processes in mind.

6. Effect of nanoparticle aggregation on physical and chemical properties

Another structural characteristic that may well impact the behaviour and fate of nanoparticles is their degree of aggregation. It is well-established that under the proper conditions, nanoparticles can spontaneously self-assemble or aggregate (Gilbert et al., 2007; Guzman et al., 2006; He et al., 2008; Moreau et al., 2007; Shipway et al., 2000). Once nanoparticles are released into chemically complex natural systems, it is reasonable to expect that some of them will aggregate, and that aggregated nanoparticle systems may be as common as dispersed systems. Here we will briefly discuss some examples of how aggregation may affect nanoparticle behaviour.

There are many indications that nanoparticle aggregates behave differently from their well-dispersed counterparts. For example, 3 nm ZnS nanoparticles have more highly-ordered crystal structures when aggregated (Huang et al., 2004). The activation energies for phase transitions in TiO_2 nanoparticles were found to be lower for less aggregated nanoparticles. This was attributed to a lower surface energy of the more aggregated nanoparticles due to interparticle interactions (Zhang and Banfield, 2007). Aggregation has also been shown to affect the thermal conductivity of nanoparticle solutions (Hong et al., 2006). Recently, aggregates of 9 nm Fe_3O_4 nanoparticles were found to reduce CCl_4, a common organic contaminant, more slowly than non-aggregated Fe_3O_4 (Vikesland et al., 2007). As shown in table B. 1, in studies of metal sorption onto nanoparticles, in some cases it was suggested that the size-dependent differences observed were due to aggregation (Gao et al., 2004).

One of the well-known effects of aggregation is its contribution to nanoparticle growth (Banfield et al., 2000; Guyodo et al., 2003; Penn and Banfield, 1998; Penn and Banfield, 1999). Simply influencing growth is very important, as changing nanoparticle size may mean changing physical and chemical properties. Aggregative growth processes

also may have an impact upon metal sequestration. Waychunas et. al. (2005) found that when Zn^{2+} was added to mixtures of α-FeOOH (goethite) nanoparticles during aggregation, Zn was either incorporated directly into the crystal or that a secondary Zn-containing precipitate was formed. XAS results from Zn^{2+} sorbed to the nanoparticles after aggregation were very different (Waychunas et al., 2005).

The connection between degree of aggregation and chemical/physical properties is quite intriguing and invites further exploration.

7. Recommendations and outlook in gaining more understanding of environmental implications of nanoparticles

Nanoparticles have size-dependent properties that may affect many environmental processes. Nevertheless, it still remains difficult to predict what these actual environmental effects might be. It is clear that more research will be conducted regarding the fate and impact of nanoparticles in the environment with size-dependent properties in mind. Here, commentary and recommendations on future directions in this research are discussed.

First, it is critical to establish how and where nanoparticles are being released into the environment. Knowing the sources and means of entry for nanoparticles will reveal which environmental exposure scenarios are the most likely. The knowledge will in turn guide researchers attempting to study the most environmentally-relevant nanoparticle systems. Many nanoparticle-based technologies are still emerging. Therefore, various release scenarios may have to be postulated. The following list, by no means exclusive, has examples of nanoparticles likely to be released into the environment. These nanoparticles are used in current and emerging nanotechnologies.

(1) Titanium dioxide and other photoactive semiconductor nanoparticles (eg. CdSe, PbS, MoS_2). Titanium dioxide and zinc oxide nanoparticles are already available in commercial sunscreen creams, and multiple applications are being developed using semiconductor nanoparticles, including sensors, cells for solar power, water-splitting for hydrogen gas generation, air cleaners, etc. A recent report on exposure modelling of

manufactured nanoparticles in the environment (in Switzerland) indicated that nano-TiO_2 is a substance of concern (Mueller and Nowack, 2008).

(2) Silver nanoparticles. Silver nanoparticle coatings are already on many commercially-available products (*e.g.* bandages, clothing) as antibacterial barriers. While Mueller and Nowack's (2008) environmental modelling, mentioned above, concluded that nanosized silver pose little risk in Switzerland based upon present data, the widespread use of nanosized silver calls for additional study.

(3) Nanozerovalent iron particles. As these nanoparticles have proven to be effective at decomposing halogenated organics in the field, their continued and potentially increasing use is likely.

Aside from knowing entry routes of nanoparticles into the environment, researchers will need to build a comprehensive knowledge base linking aspects of nanoparticle structure or chemistry (*e.g.* size, shape, coating, composition) to their behaviour in a simulated or actual environmental system. This is important because an enormous number of nanoparticle types are possible and it will be impossible to test every single one of them. Understanding trends in nanoparticle behaviour provides the ability to predict how different nanoparticles behave based upon their characteristics, even in the absence of hard data for a particular nanoparticle. Science policymakers and regulatory agencies will find this ability to predict behaviour especially useful.

Towards the goal of linking nanoparticle structure and chemistry to behaviour, it is necessary for studies to utilize exceptionally well-characterized nanoparticles. In addition to particle size and composition, features such as particle shape, coatings and aggregation state should be carefully measured or controlled if possible. Researchers should also account for any known impurities. Preferably, in any study connecting nanoparticle characteristics to behaviour, nanoparticle features should be varied carefully. For example, in a study of size dependence in nanoparticles, researchers should strive to maintain the same morphology, aggregation state, and coatings between different sizes. If this is not possible due to synthetic limitations, the other varying characteristics must be taken into account when interpreting data. Given the need for well-characterized, pure nanoparticles, it may behove environmental scientists to synthesize and characterize their own materials or to collaborate with nanochemistry specialists.

In addition to beginning studies with well-defined, well-characterized nanoparticles, if possible it is important to be able to characterize the nanoparticle structure and chemical state throughout the study. Nanoparticles may change during the study, altering their morphology, degrading (*e.g.* oxidizing), aggregating, or losing coatings. Such changes will doubtless alter the physical and chemical behaviour of the nanoparticles. Characterizing the structures and chemical state of nanoparticles well will enable researchers to better explain changes in their behaviour. In actual natural systems, nanoparticles will have many opportunities to interact with substances such as organic matter or other natural particles, and may form complex assemblages that behave very differently from the original, pure nanoparticles. Characterization of these assemblages will doubtless be important for understanding their behaviour.

The study of the interactions of manufactured nanoparticles in the environment is one of the fastest growing areas of science today, not only from the viewpoint of the scientists in various fields personally involved in these efforts, but in terms of funding opportunities. Both governments and industries are anxious to become informed about the positive and negative environmental implications of nanoparticles before environments are significantly modified in their presence. This is, in part, so that environmental degradation can be avoided. Insofar as the environmental impact experience of technologies of the past provide general, but key insights into the future, we will be wise to accelerate environmentally-related studies as much as possible. Over the next number of decades, the ramifications of manufactured nanoparticle- interactions are likely to have, in a number of cases, significant to highly significant societal, political, and economic implications.environment

Acknowledgments

This material is based upon work supported by the National Science Foundation under a grant awarded in 2006. Grants from the U.S. Department of Energy (DE-FG02-06ER15786) and the Institute for Critical Technology and Applied Science at Virginia Tech also provided support. Bryce Sadtler and Dr. Can Erdonmez contributed useful discussions. We wish to also thank the anonymous reviewers for their thoughtful suggestions.

Table B.1. Summary of particle size-dependence adsorption studies

Material	Particle sizes	Adsorbate	Size dependence	Explanation Suggested	Hysteresis?	Other comments
TiO_2, anatase (Zhang et al., 1999)	6 nm, 16 nm	Organic acids	K_{ads} (6 nm) > K_{ads} (16 nm) (up to 70-fold increase)	Molar surface free energy higher for smaller particles	N/A	
TiO_2, anatase* (Gao et al., 2004)	8-145 nm	Cd^{2+}	K_{ads} much larger for bulk than for NP's	Intraparticle electrostatic repulsion in aggregated NP's; Ti site disorder in small NP's	No, completely reversible	Degree of aggregation not quantitatively assessed
TiO_2, anatase* (Giammar et al., 2007)	20-33 nm vs. 520 nm	Pb^{2+}	K_{ads} and Γ_{max} much larger for bulk than NP's	Surface geometry and bonding	N/A	Aggregation state and morphology of particles not characterized
α-Fe_2O_3, hematite (Madden et al., 2006)	7 nm, 25 nm, 88 nm	Cu^{2+}	SA- normalized sorption onto 7 nm > 25 nm = 88 nm	Distorted bonding geometry at intersections of crystal faces	N/A	88 nm sample had variable morphology and more aggregation
α-FeOOH (Waychunas et al., 2005)	5 nm, 25 nm, 75 nm	Hg^{2+}	SA-normalized sorption onto 5 nm < 25 nm = 75 nm	Surface geometry of atoms less favourable for bonding; charge distribution	N/A	
Fe_3O_4 (Yean et al., 2005)	11.72 nm, 20 nm, 300 nm	As (V) and As (III)	Γ_{max} for 11.72 nm particles greater	More surface sites due to less aggregation	Yes, greater for 20 nm than 300 nm	20 nm, 300 nm variable morphology, aggregated. NOM decreased As adsorption.

*One or more samples contained rutile-phase TiO_2. Note: SA = surface area, NP = nanoparticle, N/A means that hysteresis data was not available, and NOM stands for natural organic matter

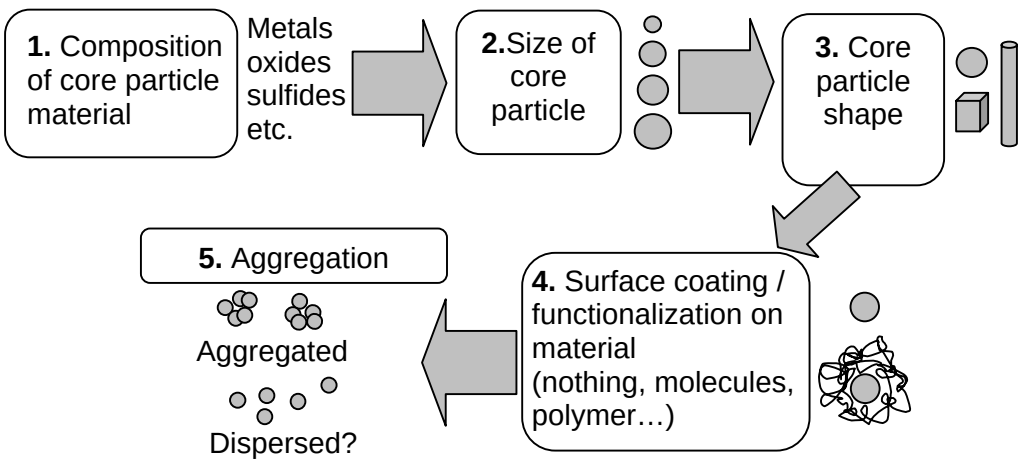

Figure B. 1. Flow diagram displaying variables in the "anatomy" of a colloidal inorganic nanoparticle.

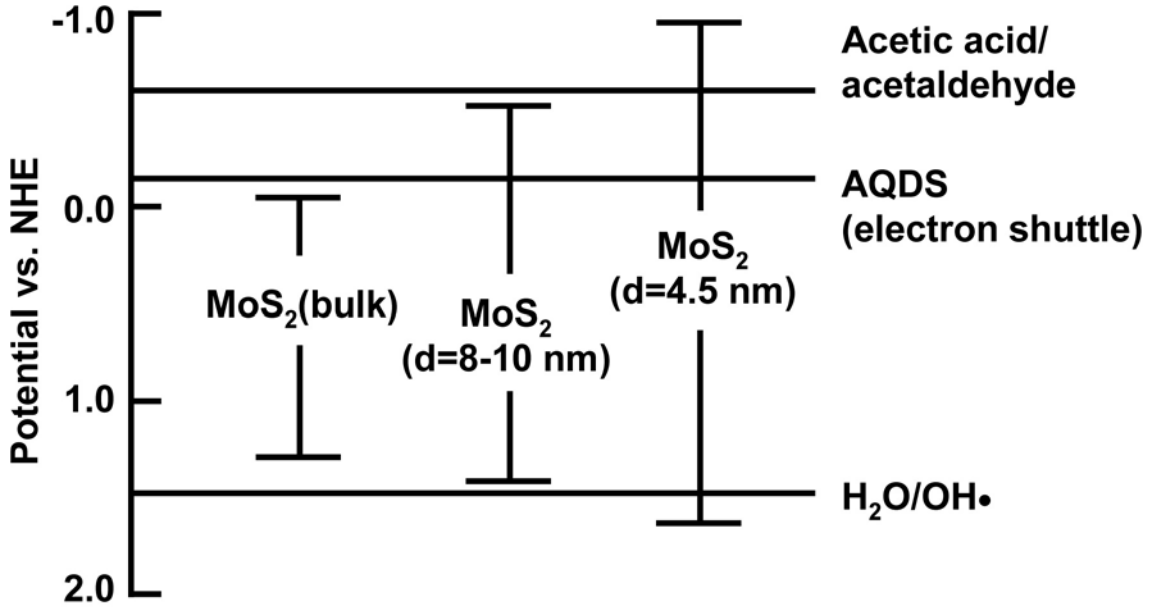

Figure B. 2. Position of the conduction and valence band edges versus the normal hydrogen electrode (NHE) for bulk and nanoparticulate MoS_2, plus redox potentials for environmentally- or biologically-relevant half reactions. Note that by varying size, the redox properties of MoS_2 are altered. For example, photoexcited 4.5 nm MoS_2 nanoparticles have holes with a redox potential more positive than 1.2-1.5 V, which means these holes can oxidize water and create hydroxyl radicals. The hydroxyl radicals can then degrade organic chemicals or potentially cause oxidative damage in biological systems. Also displayed are redox potentials for the carboxylation of acetate to pyruvate and for the reduction of AQDS, a synthetic analog of electron shuttle molecules important for bacterial respiration. Adapted with permission from T.R. Thurston and J.P. Wilcoxon (1999), Photooxidation of organic chemicals catalyzed by nanoscale MoS_2; Journal of Physical Chemistry B, 103, 11-17. Copyright (1999) American Chemical Society

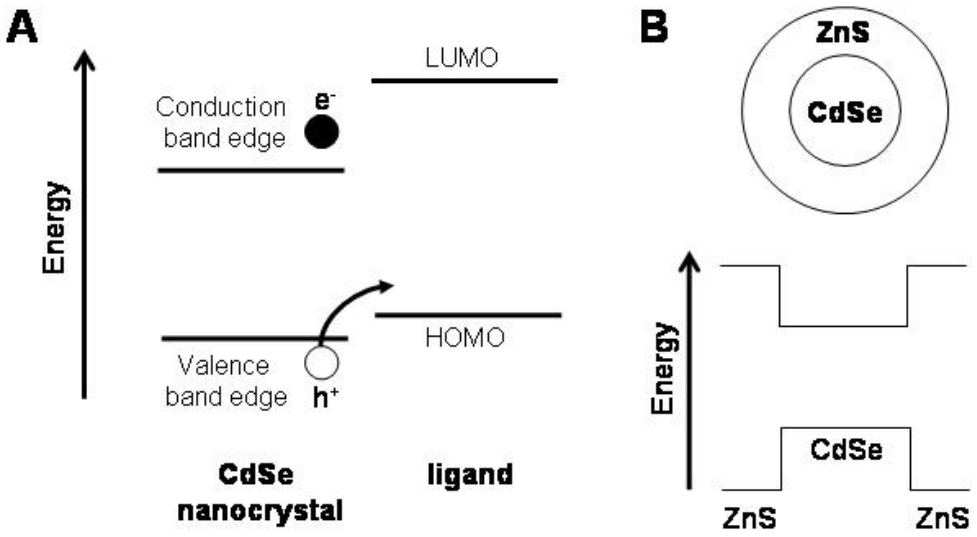

Figure B. 3. A. Schematic of valence and conduction band edges in a CdSe nanoparticle and their energetic alignment with a molecular ligand coating the particle. Mobile charge carriers (the hole and electron) are generated when a photon is absorbed by the nanoparticle, as shown. Holes can be transferred to the highest occupied molecular orbital (HOMO) of the ligand. Adapted from D.J. Milliron, A.P. Alivisatos, C. Pitois, C. Edder and J.M.J. Frechet (2003), Electroactive Surfactant Designed to Mediate Electron Transfer Between CdSe Nanocrystals and Organic Semiconductors; Advanced Materials, 15, 58-61. Copyright Wiley-VCH Verlag GmbH & Co. KGaA. Reproduced with permission. B. Schematic of a CdSe-ZnS core-shell nanoparticle and the corresponding band edges of the core and the shell. Adapted from B.O. Dabbousi, J. Rodriguez Viejo, F.V. Mikulec, J.R. Heine, H. Mattoussi, R. Ober, K.F. Jensen, and M.G. Bawendi, (1997), (CdSe)ZnS core-shell quantum dots: synthesis and characterization of a size series of highly luminescent nanocrystallites; Journal of Physical Chemistry B, 101, 9463-9475. Copyright (1997) American Chemical Society.

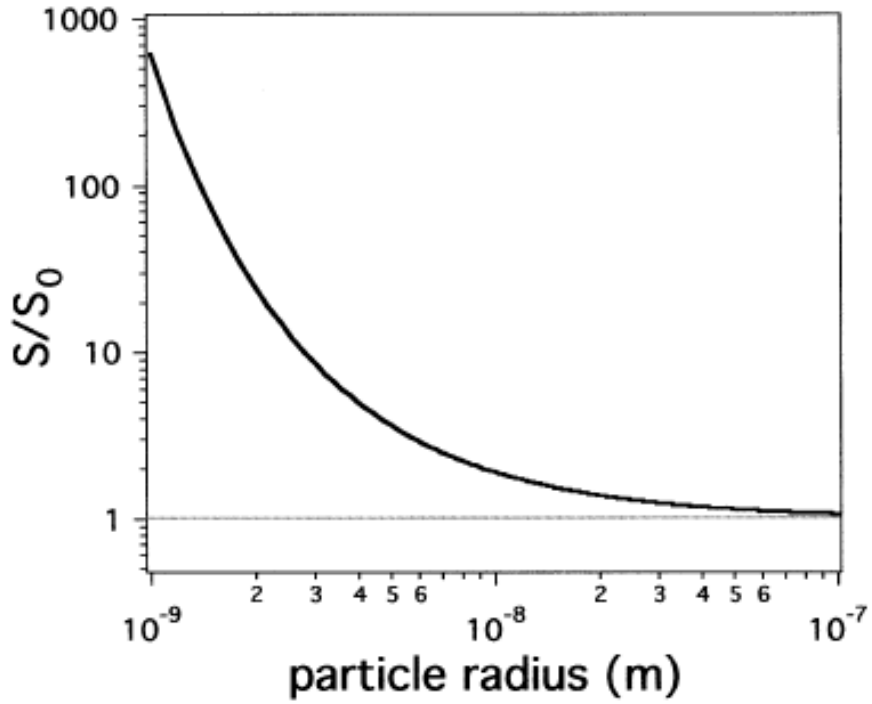

Figure B. 4. The deviation of the solubility of small grains of quartz relative to its bulk solubility (S/S_0) as a function of the size of the quartz grains being dissolved according to Eq. B. 2. The following values were used to produce this curve: T= 298 K, $\overline{V}$ = 22.68 x10^{-6} m^3/mol, γ= 350 mJ/m^2. At a particle radius of 100 nm, the solubility is indistinguishable from the bulk value. By the time the particle radius is reduced to 1 nm, the predicted solubility is nearly three orders of magnitude higher. Reprinted from Earth and Planetary Science Letters, 203, M.F. Hochella, Jr., Nanoscience and technology: the next revolution in the Earth Sciences, Pages 593-605, Copyright (2002), with permission from Elsevier.

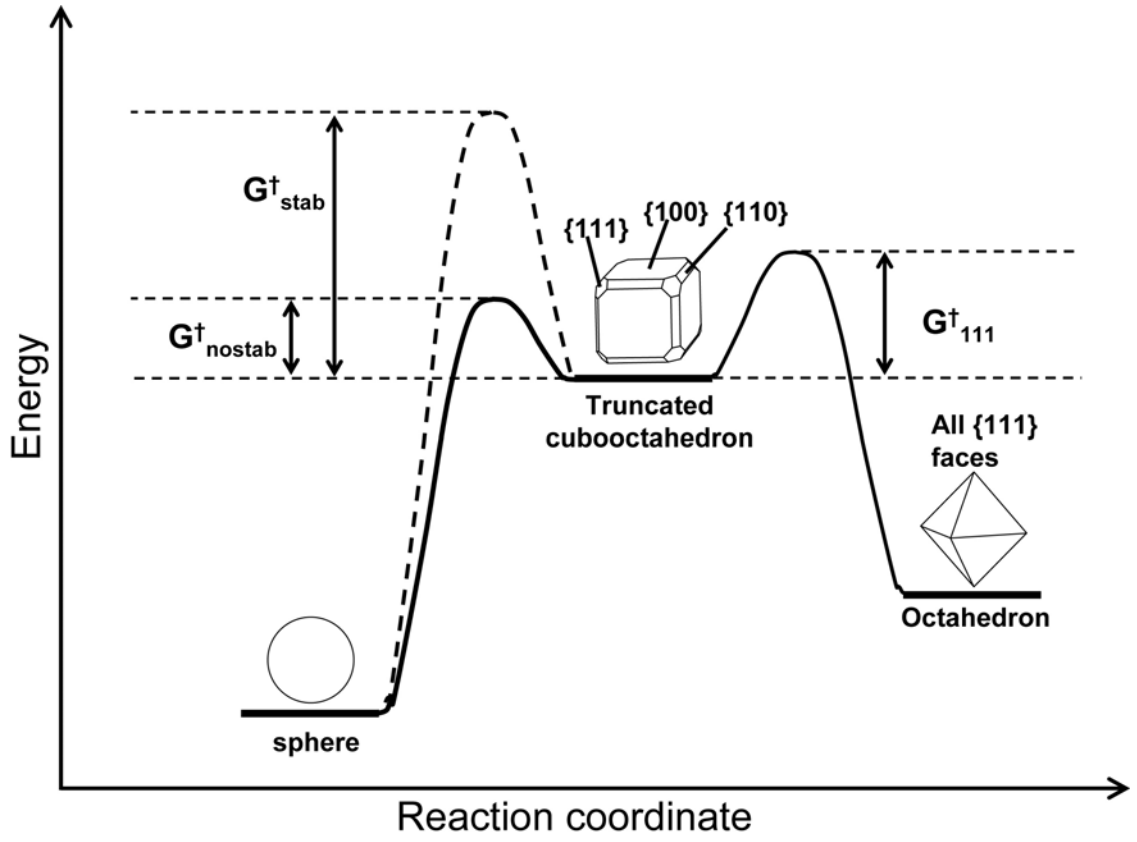

Figure B. 5. Reaction coordinate for the partial dissolution (etching) of a truncated cubooctahedral nanoparticle. For this system, the thermodynamically-favoured product is a spherical nanoparticle. In the absence of stabilizing coatings or ligands, formation of a spherical nanoparticle is kinetically favoured as well (the activation energy $\Delta G^{\dagger}_{nostab} < \Delta G^{\dagger}_{111}$). In the presence of compounds that stabilize the {100} and {110} faces, the activation energy to obtain a spherical nanoparticle increases. In this case, since this activation energy is greater than that necessary to form an octahedron (energy $\Delta G^{\dagger}_{stab} > \Delta G^{\dagger}_{111}$), formation of a sphere is no longer kinetically favoured. Etching the non-stabilized {111} faces is kinetically favoured. In the absence of enough thermal energy in the system, etching will result in an octahedral endproduct rather than a spherical one. Figure adapted from Y.W. Jun, J.S. Choi, and J.W. Cheon (2006), Shape control of semiconductor and metal oxide nanocrystals through nonhydrolytical colloidal routes; Angewandte Chemie, 45, 3414-3439. Copyright Wiley-VCH Verlag GmbH & Co. KGaA. Reproduced with permission.

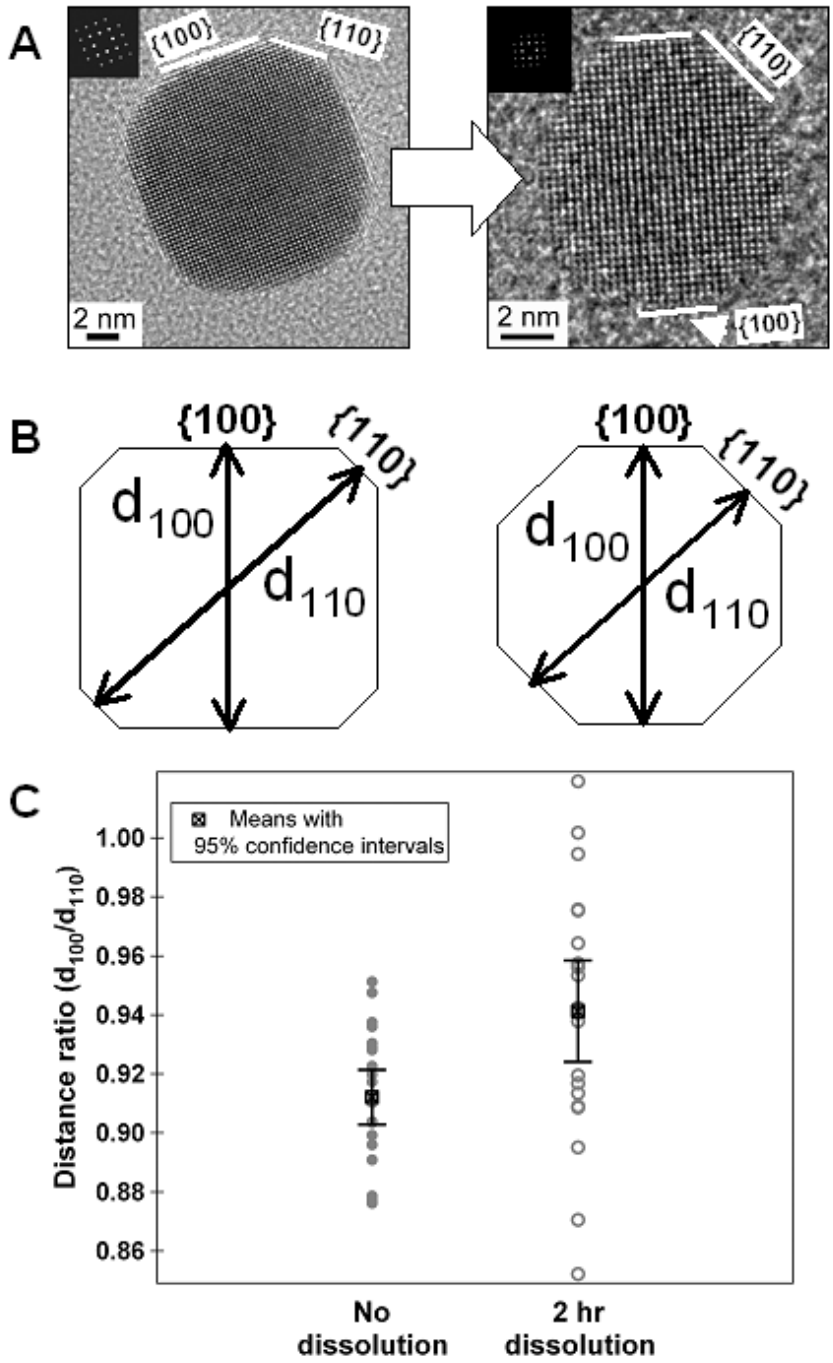

Figure B. 6. A. HRTEM images of a nanoparticle before dissolution (left) and a nanoparticle after 2 hours of dissolution (right). Note how the size of the {110} faces have increased. B. Schematic diagrams of the distances measured on particles to determine whether the change in {110} size is statistically significant. C. Distance ratios of d_{100}/d_{110} before and after dissolution, along with mean values and 95% confidence intervals. As the {110} face size increases after 2 hours of dissolution, the value of the ratio increases. Data in C. from Liu et.al. (2007).

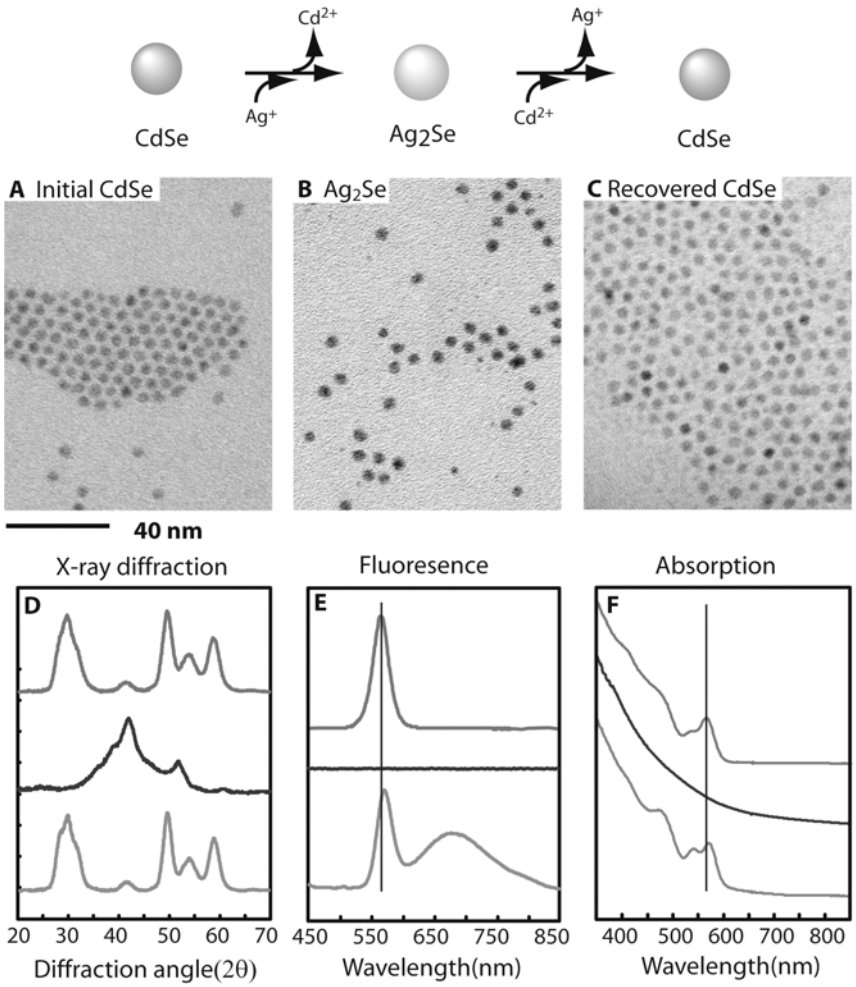

Figure B. 7. TEM images of (**A**) initial CdSe (diameter 4.2 nm), (**B**) Ag_2Se transformed from the forward cation exchange reaction, and (**C**) recovered CdSe nanocrystals from the reverse cation exchange reaction. (**D** to **F**) XRD patterns, fluorescence emission, and optical absorption spectra of initial CdSe (top diffractogram or spectrum), Ag_2Se (middle), and recovered CdSe (bottom) nanocrystals, respectively. In the recovered CdSe, the peak positions of the emission and absorption show a slight redshift from those of the initial CdSe, which becomes negligible for nanospheres larger than 6 nm in diameter. An additional fluorescence emission feature near 700 nm seen in the recovered CdSe (E) is due to the increased surface trap emission. Vertical lines in (E) and (F) are a guide for the comparison of peak positions. Figure and caption from D.H. Son, S.M. Hughes, Y.D. Yin, and A.P. Alivisatos (2004), Cation exchange reactions in ionic nanocrystals; Science, 306, 1009-1012. Reprinted with permission from AAAS.

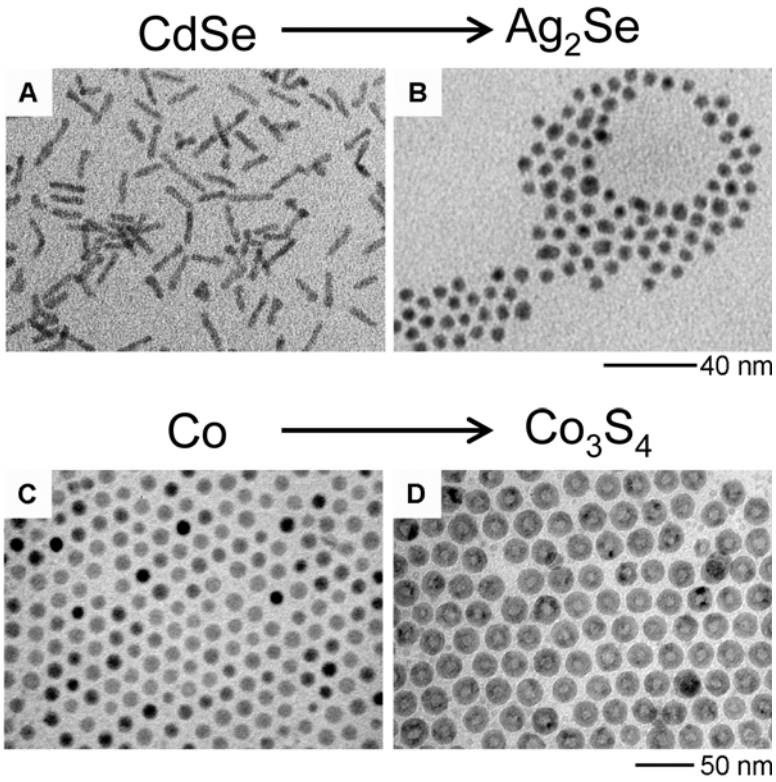

Figure B. 8. Examples of shape change after cation exchange reactions. A and B: Conversion of nanorods to nanospheres when exchanging Ag for Cd. C and D: Conversion of solid cobalt nanospheres to hollow cobalt sulphide nanospheres, due to rapid diffusion of Co ions**.** A and B from D.H. Son, S.M. Hughes, Y.D. Yin, and A.P. Alivisatos (2004), Cation exchange reactions in ionic nanocrystals; Science, 306, 1009-1012. C and D from Y.D. Yin, R.M. Rioux, C.K. Erdonmez, S.M. Hughes, G.A. Somorjai, and A.P. Alivisatos (2004), Formation of hollow nanocrystals through the nanoscale Kirkendall effect, Science, 304, 711-714. Reprinted with permission from AAAS.

References

Abrams, B.L. and Wilcoxon, J.P., 2005. Nanosize semiconductors for photooxidation. Critical Reviews in Solid State and Materials Sciences, 30(3): 153-182.

Adamson, A.W., 1982. Physical Chemistry of Surfaces. Wiley, New York, 664 pp.

Aldana, J., Wang, Y.A. and Peng, X.G., 2001. Photochemical instability of CdSe nanocrystals coated by hydrophilic thiols. Journal of the American Chemical Society, 123(36): 8844-8850.

Alivisatos, A.P., 1996. Perspectives on the physical chemistry of semiconductor nanocrystals. Journal of Physical Chemistry, 100(31): 13226-13239.

Anschutz, A.J. and Penn, R.L., 2005. Reduction of crystalline iron(III) oxyhydroxides using hydroquinone: Influence of phase and particle size. Geochemical Transactions, 6(3): 60-66.

Aruguete, D.M. et al., 2007. Surface structure of CdSe nanorods revealed by combined X-ray absorption fine structure measurements and ab initio calculations. Journal of Physical Chemistry C, 111(1): 75-79.

Atkins, P.W.P.W., 1940-, 1998. Physical chemistry, xvi, 999 p. :. Freeman,, New York :.

Banfield, J.F., Welch, S.A., Zhang, H.Z., Ebert, T.T. and Penn, R.L., 2000. Aggregation-based crystal growth and microstructure development in natural iron oxyhydroxide biomineralization products. Science, 289(5480): 751-754.

Becker, U. et al., 2005. Interactions between mineral surfaces and dissolved species: From monovalent ions to complex organic molecules. American Journal of Science, 305(6-8): 791-825.

Becker, W.M. and Deamer, D.W., 1986. The World of the Cell. Benjamin/Cummings Publishing Company, Inc., Redwood City, California.

Brown, G.E. et al., 1999. Metal oxide surfaces and their interactions with aqueous solutions and microbial organisms. Chemical Reviews, 99: 77-174.

Bruchez, M., Moronne, M., Gin, P., Weiss, S. and Alivisatos, A.P., 1998. Semiconductor nanocrystals as fluorescent biological labels. Science, 281(5385): 2013-2016.

Budz, J.A. and Nancollas, G.H., 1988. The mechanism of dissolution of hydroxyapatite and carbonated apatite in acidic solutions. Journal of Crystal Growth, 91(4): 490-496.

Casey, W.H. and Ludwig, C., 1995. Silicate mineral dissolution as a ligand-exchange reaction. In: A.F. White and S.L. Brantley (Editors), Chemical Weathering Rates of Silicate Minerals. Reviews in Mineralogy. Mineralogical Society of America, Washington, D.C., pp. 583.

Chan, E.M. et al., 2007. Millisecond kinetics of nanocrystal cation exchange using microfluidic X-ray absorption spectroscopy. Journal of Physical Chemistry A, 111(49): 12210-12215.

Cornell, R.M. and Schwertmann, U., 2003. The Iron Oxides: Structure, Properties, Reactions, Occurences and Uses. Wiley-VCH, Weinheim, 664 pp.

Cozzoli, P.D. et al., 2004. Role of Metal Nanoparticles in TiO2/Ag Nanocomposite-Based Microheterogeneous Photocatalysis. Journal of Physical Chemistry B, 108: 9623-9630.

Dabbousi, B.O. et al., 1997. (CdSe)ZnS core-shell quantum dots: Synthesis and characterization of a size series of highly luminescent nanocrystallites. Journal of Physical Chemistry B, 101(46): 9463-9475.

Davison, W. and De Vitre, R., 1992. Iron Particles in Freshwater. In: J. Buffle and H.P. Van Leeuwen (Editors), Environmental Particles. Lewis Publishers, Ann Arbor, MI, pp. 315-355.

Deng, J.P., Shih, W.C. and Mou, C.Y., 2005. Hydrogenation of anthracene catalyzed by surfactant-protected gold nanoparticles in aqueous solution: Size dependence. Chemphyschem, 6(10): 2021-2025.

Deng, J.P., Shih, W.C. and Mou, C.Y., 2007. Electron transfer-induced hydrogenation of anthracene catalyzed by gold and silver nanoparticles. Journal of Physical Chemistry C, 111(27): 9723-9728.

Dinega, D.P. and Bawendi, M.G., 1999. A solution-phase chemical approach to a new crystal structure of cobalt. Angewandte Chemie-International Edition, 38(12): 1788-1791.

Dloczik, L. and Koenenkamp, R., 2004. Nanostructured metal sulfide surfaces by ion exchange processes. Journal of Solid State Electrochemistry, 8(3): 142-146.

Drever, J.I., 1997. The Geochemistry of Natural Waters. Prentice Hall, Upper Saddle River, NJ.

Duan, C.F. et al., 2007. Size-dependent inhibition and enhancement by gold nanoparticles of luminol-ferricyanide chemiluminescence. Journal of Physical Chemistry C, 111(12): 4561-4566.

Dzombak, D.A. and Morel, F.M.M., 1990. Surface complexation modeling: hydrous ferric oxide. Wiley, New York.

Elliott, D.W. and Zhang, W.X., 2001. Field assessment of nanoscale bimetallic particles for groundwater treatment. Environmental Science & Technology, 35: 4922-4926.

El-Sayed, I., Huang, X. and El-Sayed, M., 2007. Multicolorimetric plasmonic gold nanoparticles for 8 optical detection of oral squamous carcinoma. Oral Oncology: 121-121.

El-Sayed, I.H., Huang, X.H. and El-Sayed, M.A., 2005. Surface plasmon resonance scattering and absorption of anti-EGFR antibody conjugated gold nanoparticles in cancer diagnostics: Applications in oral cancer. Nano Letters, 5(5): 829-834.

Faust, B.C., Hoffmann, M.R. and Bahnemann, D.W., 1989. Photocatalytic oxidation of sulfur dioxide in aqueous suspensions of alpha-Fe2O3. Journal of Physical Chemistry, 93: 6371-6381.

Filip, J. et al., 2007. Environmental applications of chemically pure natural ferrihydrite. Environmental Science & Technology, 41(12): 4367-4374.

Franklin, N.M. et al., 2007. Comparative toxicity of nanoparticulate ZnO, bulk ZnO, and ZnCl2 to a freshwater microalga (Pseudokirchneriella subcapitata): The importance of particle solubility. Environmental Science & Technology, 41: 8484-8490.

Gao, L.Z. et al., 2007. Intrinsic peroxidase-like activity of ferromagnetic nanoparticles. Nature Nanotechnology, 2: 577-583.

Gao, X.H. et al., 2005. In vivo molecular and cellular imaging with quantum dots. Current Opinion in Biotechnology, 16(1): 63-72.

Gao, Y. et al., 2004. Adsorption of cadmium on anatase nanoparticles-effect of crystal size and pH. Langmuir, 20(22): 9585-9593.
Giammar, D.E., Maus, C.J. and Xie, L.Y., 2007. Effects of particle size and crystalline phase on lead adsorption to titanium dioxide nanoparticles. Environmental Engineering Science, 24(1): 85-95.
Giasuddin, A.B.M., Kanel, S.R. and Choi, H., 2007. Adsorption of humic acid onto nanoscale zerovalent iron and its effect on arsenic removal. Environmental Science & Technology, 41(6): 2022-2027.
Gilbert, B., Lu, G.P. and Kim, C.S., 2007. Stable cluster formation in aqueous suspensions of iron oxyhydroxide nanoparticles. Journal of Colloid and Interface Science, 313(1): 152-159.
Guyodo, Y., Mostrom, A., Penn, R.L. and Banerjee, S.K., 2003. From Nanodots to Nanorods: Oriented aggregation and magnetic evolution of nanocrystalline goethite. Geophysical Research Letters, 30(10).
Guzman, K.A.D., Finnegan, M.P. and Banfield, J.F., 2006. Influence of surface potential on aggregation and transport of titania nanoparticles. Environmental Science & Technology, 40(24): 7688-7693.
Hagfeldt, A. and Gratzel, M., 1995. Light-Induced Redox Reactions in Nanocrystalline Systems. Chemical Reviews, 95(1): 49-68.
Halim, K.S.A., Khedr, M.H., Nasr, M.I. and El-Mansy, A.M., 2007. Factors affecting CO oxidation over nanosized Fe2O3. Materials Research Bulletin, 42(4): 731-741.
Hamad, K.S., Roth, R., Rockenberger, J., van Buuren, T. and Alivisatos, A.P., 1999. Structural disorder in colloidal InAs and CdSe nanocrystals observed by X-ray absorption near-edge spectroscopy. Physical Review Letters, 83(17): 3474-3477.
Harris, L.A. et al., 2003. Magnetite nanoparticle dispersions stabilized with triblock copolymers. Chemistry of Materials, 15(6): 1367-1377.
Hayat, M.A. (Editor), 1989. Colloidal gold : principles, methods, and applications, 2. Academic Press, San Diego.
He, Y.T., J., W. and T., T., 2008. Kinetic stability of hematite nanoparticles: the effect of particle sizes. Journal of Nanoparticle Research, 10: 321-332.
Hermanek, M., Zboril, R., Medrik, N., Pechousek, J. and Gregor, C., 2007. Catalytic efficiency of iron(III) oxides in decomposition of hydrogen peroxide: Competition between the surface area and crystallinity of nanoparticles. Journal of the American Chemical Society, 129(35): 10929-10936.
Hines, M.A. and Guyot-Sionnest, P., 1996. Synthesis and characterization of strongly luminescing ZnS-Capped CdSe nanocrystals. Journal of Physical Chemistry, 100(2): 468-471.
Hochella, M.F., 2002. Nanoscience and technology the next revolution in the Earth sciences. Earth and Planetary Science Letters, 203(2): 593-605.
Hochella, M.F., Kasama, T., Putnis, A., Putnis, C.V. and Moore, J.N., 2005a. Environmentally important, poorly crystalline Fe/Mn hydrous oxides: Ferrihydrite and a possibly new vernadite-like mineral from the Clark Fork River Superfund Complex. American Mineralogist, 90(4): 718-724.
Hochella, M.F. et al., 2008. Nanominerals, Mineral Nanoparticles, and Earth Systems. Science, 319(5870): 1631-1635.

Hochella, M.F. and Madden, A.S., 2005. Earth's nano-compartment for toxic metals. Elements, 1(4): 199-203.

Hochella, M.F. et al., 2004. Environmentally important nanoparticles from a massive acid mine drainage site. Geochimica Et Cosmochimica Acta, 68(11): A103-A103.

Hochella, M.F. et al., 2005b. Direct observation of heavy metal-mineral association from the Clark Fork River Superfund Complex: Implications for metal transport and bioavailability. Geochimica Et Cosmochimica Acta, 69(7): 1651-1663.

Hong, K.S., Hong, T.K. and Yang, H.S., 2006. Thermal conductivity of Fe nanofluids depending on the cluster size of nanoparticles. Applied Physics Letters, 88(3): 031901-1-031901-3.

Houben, G.J., 2003. Iron oxide incrustations in wells. Part 2: chemical dissolution and modeling. Applied Geochemistry, 18(6): 941-954.

Huang, F., Gilbert, B., Zhang, H.H. and Banfield, J.F., 2004. Reversible, surface-controlled structure transformation in nanoparticles induced by an aggregation state. Physical Review Letters, 92(15).

Huang, X., Qian, W., El-Sayed, I.H. and El-Sayed, M.A., 2007a. The potential use of the enhanced nonlinear properties of gold nanospheres in photothermal cancer therapy. Lasers in Surgery and Medicine, 39: 747-753.

Huang, X.H., El-Sayed, I.H., Qian, W. and El-Sayed, M.A., 2006. Cancer cell imaging and photothermal therapy in the near-infrared region by using gold nanorods. Journal of the American Chemical Society, 128(6): 2115-2120.

Huang, X.H., Jain, P.K., El-Sayed, I.H. and El-Sayed, M.A., 2007b. Gold nanoparticles: interesting optical properties and recent applications in cancer diagnostic and therapy. Nanomedicine, 2: 681-693.

Imlay, J.A., 2003. Pathways of oxidative damage. Annual Review of Microbiology, 57: 395-418.

Jeong, H.Y., Klaue, B., Blum, J.D. and Hayes, K.F., 2007. Sorption of mercuric ion by synthetic nanocrystalline mackinawite (FeS). Environmental Science & Technology, 41(22): 7699-7705.

Johnson, T.L., Scherer, M.M. and Tratnyek, P.G., 1996. Kinetics of halogenated organic compound degradation by iron metal. Environmental Science & Technology, 30(8): 2634-2640.

Joo, J. et al., 2003. Generalized and facile synthesis of semiconducting metal sulfide nanocrystals. Journal of the American Chemical Society, 125(36): 11100-11105.

Jun, Y.W., Choi, J.S. and Cheon, J.W., 2006. Shape control of semiconductor and metal oxide nanocrystals through nonhydrolytical colloidal routes. Angewandte Chemie-International Edition, 45: 3414-3439.

Kamat, P.V. and Meisel, D., 2002. Nanoparticles in advanced oxidation processes. Current Opinion in Colloid & Interface Science, 7: 282-287.

Kersting, A.B. et al., 1999. Migration of plutonium in ground water at the Nevada Test Site. Nature, 397(6714): 56-59.

Ketchie, W.C., Fang, Y.L., Wong, M.S., Murayama, M. and Davis, R.J., 2007. Influence of gold particle size on the aqueous-phase oxidation of carbon monoxide and glycerol. Journal of Catalysis, 250(1): 94-101.

Kiwi, J. and Gratzel, M., 1979. Protection, size factors, and reaction dynamics of colloidal redox catalysts mediating light induced hydrogen evolution from water. Journal of the American Chemical Society, 101(24): 7214-7216.

Kloepfer, J.A., Bradforth, S.E. and Nadeau, J.L., 2005. Photophysical properties of biologically compatible CdSe quantum dot structures. Journal of Physical Chemistry B, 109(20): 9996-10003.

Korgel, B.A. and Monbouquette, H.G., 1997. Quantum confinement effects enable photocatalyzed nitrate reduction at neutral pH using CdS nanocrystals. Journal of Physical Chemistry B, 101(25): 5010-5017.

Kretzschmar, R. and Schafer, T., 2005. Metal retention and transport on colloidal particles in the environment. Elements, 1(4): 205-210.

Labrenz, M. et al., 2000. Formation of sphalerite (ZnS) deposits in natural biofilms of sulfate-reducing bacteria. Science, 290(5497): 1744-1747.

Larsen, O. and Postma, D., 2001. Kinetics of reductive bulk dissolution of lepidocrocite, ferrihydrite, and goethite. Geochimica Et Cosmochimica Acta, 65(9): 1367-1379.

Lasaga, A.C., 1998. Kinetic theory in the earth sciences, x, 811 p. :. Princeton University Press, Princeton, N.J.

Lasaga, A.C. and Luttge, A., 2004. Mineralogical approaches to fundamental crystal dissolution kinetics. American Mineralogist, 89(4): 527-540.

Lee, J.H. et al., 2006. Artificially engineered magnetic nanoparticles for ultra-sensitive molecular imaging. Nature Medicine, 13: 95-99.

Li, L. et al., 2006a. Synthesis, properties, and environmental applications of nanoscale iron-based materials: A review. Critical Reviews in Environmental Science and Technology, 36(5): 405-431.

Li, R.F. et al., 2005. Amine-assisted facetted etching of CdSe nanocrystals. Journal of the American Chemical Society, 127: 2524-2532.

Li, R.F. et al., 2006b. Band-edge photoluminescence recovery from zinc-blende CdSe nanocrystals synthesized at room temperature. Advanced Functional Materials, 16(3): 345-350.

Li, X.Q., Elliott, D.W. and Zhang, W.X., 2006c. Zero-valent iron nanoparticles for abatement of environmental pollutants: Materials and engineering aspects. Critical Reviews in Solid State and Materials Sciences, 31(4): 111-122.

Liou, Y.H., Lo, S.L., Kuan, W.H., Lin, C.J. and Weng, S.C., 2006. Effect of precursor concentration on the characteristics of nanoscale zerovalent iron and its reactivity of nitrate. Water Research, 40(13): 2485-2492.

Liu, G. et al., 2006. Characterization and surface reactivity of ferrihydrite nanoparticles assembled in ferritin. Langmuir, 22(22): 9313-9321.

Liu, J., Aruguete, D., Jinschek, J. and Hochella, M.F., 2007a. TEM investigation of the non-oxidative dissolution of galena (PbS) nanoparticles in a hydrochloric acid solution. Geochimica Et Cosmochimica Acta, 71(15): A589.

Liu, Q. et al., 2007b. Morphology control of Fe2O3 nanocrystals and their application in catalysis. Nanotechnology, 18.

Liu, Y.Q., Choi, H., Dionysiou, D. and Lowry, G.V., 2005a. Trichloroethene hydrodechlorination in water by highly disordered monometallic nanoiron. Chemistry of Materials, 17(21): 5315-5322.

Liu, Y.Q., Majetich, S.A., Tilton, R.D., Sholl, D.S. and Lowry, G.V., 2005b. TCE dechlorination rates, pathways, and efficiency of nanoscale iron particles with different properties. Environmental Science & Technology, 39(5): 1338-1345.

Lo, I.M.C., Surampalli, R. and Lai, K.C.K. (Editors), 2007. Zerovalent iron reactive materials for hazardous waste and inorganics removal. American Society of Civil Engineers, Reston, VA.

Lokhande, C.D., Bhad, V.V. and Dhumure, S.S., 1992. Conversion of Tin Disulfide into Silver Sulfide by a Simple Chemical Method. Journal of Physics D-Applied Physics, 25(2): 315-318.

Lowry, G.V. and Johnson, K.M., 2004. Congener-specific dechlorination of dissolved PCBs by microscale and nanoscale zerovalent iron in a water/methanol solution. Environmental Science & Technology, 38(19): 5208-5216.

Madden, A.S. and Hochella, M.F., 2005. A test of geochemical reactivity as a function of mineral size: Manganese oxidation promoted by hematite nanoparticles. Geochimica Et Cosmochimica Acta, 69(2): 389-398.

Madden, A.S., Hochella, M.F. and Luxton, T.P., 2006. Insights for size-dependent reactivity of hematite nanomineral surfaces through Cu2+ sorption. Geochimica Et Cosmochimica Acta, 70(16): 4095-4104.

Marcus, M.A., Flood, W., Stiegerwald, M., Brus, L. and Bawendi, M., 1991. Structure of Capped Cdse Clusters by Exafs. Journal of Physical Chemistry, 95(4): 1572-1576.

Martin, J.E. et al., 2008. Determination of the oxide layer thickness in core-shell zerovalent iron nanoparticles. Langmuir, 24: 4329-4334.

McBride, M.B., 1994. Environmental Chemistry of Soils. Oxford University Press, New York.

McDonald, J.E., 1962. Homogeneous nucleation of vapor condensation. I. Thermodynamic Aspects. American Journal of Science, 30: 870-877.

Meulenkamp, E.A., 1998. Size dependence of the dissolution of ZnO nanoparticles. Journal of Physical Chemistry B, 102(40): 7764-7769.

Mews, A., Eychmuller, A., Giersig, M., Schooss, D. and Weller, H., 1994. Preparation, Characterization, and Photophysics of the Quantum-Dot Quantum-Well System Cds/Hgs/Cds. Journal of Physical Chemistry, 98(3): 934-941.

Miller, D.S., Bard, A.J., McLendon, G. and Ferguson, J., 1981. Catalytic water reduction at colloidal metal "microelectrodes". 2. Theory and experiment. Journal of the American Chemical Society, 103: 5336-5341.

Milliron, D.J., Alivisatos, A.P., Pitois, C., Edder, C. and Frechet, J.M.J., 2003. Electroactive surfactant designed to mediate electron transfer between CdSe nanocrystals and organic semiconductors. Advanced Materials, 15(1): 58-+.

Moreau, J.W. et al., 2007. Extracellular proteins limit the dispersal of biogenic nanoparticles. Science, 316(5831): 1600-1603.

Mueller, N.C. and Nowack, B., 2008. Exposure modeling of engineered nanoparticles in the environment. Environmental Science & Technology, 42: 4447-4453.

Narayanan, R. and El-Sayed, M.A., 2005. Catalysis with transition metal nanoparticles in colloidal solution: Nanoparticle shape dependence and stability. Journal of Physical Chemistry B, 109(26): 12663-12676.

Nie, S.M., Xing, Y., Kim, G.J. and Simons, J.W., 2007. Nanotechnology applications in cancer. Annual Review of Biomedical Engineering, 9: 257-288.

Noguera, C., Pojani, A., Casek, P. and Finocchi, F., 2002. Electron redistribution in low-dimensional oxide structures. Surface Science, 507: 245-255.

Nurmi, J.T. et al., 2005. Characterization and properties of metallic iron nanoparticles: Spectroscopy, electrochemistry, and kinetics. Environmental Science & Technology, 39(5): 1221-1230.

Oyelere, A.K., Chen, P.C., Huang, X.H., El-Sayed, I.H. and El-Sayed, M.A., 2007. Peptide-conjugated gold nanorods for nuclear targeting. Bioconjugate Chemistry, 18: 1490-1497.

Panigrahi, S. et al., 2007. Synthesis and size-selective catalysis by supported gold nanoparticles: Study on heterogeneous and homogeneous catalytic process. Journal of Physical Chemistry C, 111(12): 4596-4605.

Pellegrino, T. et al., 2004. Hydrophobic nanocrystals coated with an amphiphilic polymer shell: A general route to water soluble nanocrystals. Nano Letters, 4(4): 703-707.

Penn, R.L. and Banfield, J.F., 1998. Oriented attachment and growth, twinning, polytypism, and formation of metastable phases: Insights from nanocrystalline TiO2. American Mineralogist, 83(9-10): 1077-1082.

Penn, R.L. and Banfield, J.F., 1999. Morphology development and crystal growth in nanocrystalline aggregates under hydrothermal conditions: Insights from titania. Geochimica Et Cosmochimica Acta, 63(10): 1549-1557.

Quinn, J. et al., 2005. Field demonstration of DNAPL dehalogenation using emulsified zero-valent iron. Environmental Science & Technology, 39: 1309-1318.

Rhyner, M.N. et al., 2006. Quantum dots and multifunctional nanoparticles: new contrast agents for tumor imaging. Nanomedicine, 1(2): 209-217.

Robinson, R.D. et al., 2007. Spontaneous superlattice formation in nanorods through partial cation exchange. Science, 317(5836): 355-358.

Rockenberger, J. et al., 1997. EXAFS studies on the size dependence of structural and dynamic properties of CdS nanoparticles. Journal of Physical Chemistry B, 101(14): 2691-2701.

Rockenberger, J. et al., 1998. The contribution of particle core and surface to strain, disorder and vibrations in thiolcapped CdTe nanocrystals. Journal of Chemical Physics, 108(18): 7807-7815.

Roden, E.E., 2003. Fe(III) oxide reactivity toward biological versus chemical reduction. Environmental Science & Technology, 37: 1319-1324.

Roden, E.E. and Zachara, J.M., 1996. Microbial reduction of crystalline iron(III) oxides: Influence of oxide surface area and potential for cell growth. Environmental Science & Technology, 30(5): 1618-1628.

Roelofs, F. and Vogelsberger, W., 2004. Dissolution kinetics of synthetic amorphous silica in biological-like media and its theoretical description. Journal of Physical Chemistry B, 108(31): 11308-11316.

Sau, T.K., Pal, A. and Pal, T., 2001. Size regime dependent catalysis by gold nanoparticles for the reduction of eosin. Journal of Physical Chemistry B, 105(38): 9266-9272.

Sayre, L.M., Perry, G. and Smith, M.A., 2008. Oxidative stress and neurotoxicity. Chemical Research in Toxicology, 21: 172-188.

Schmidt, J. and Vogelsberger, W., 2006. Dissolution kinetics of titanium dioxide nanoparticles: The observation of an unusual kinetic size effect. Journal of Physical Chemistry B, 110(9): 3955-3963.

Schrick, B., Blough, J.L., Jones, A.D. and Mallouk, T.E., 2002. Hydrodechlorination of trichloroethylene to hydrocarbons using bimetallic nickel-iron nanoparticles. Chemistry of Materials, 14(12): 5140-5147.

Schwertmann, U., Cambier, P. and Murad, E., 1985. Properties of Goethites of Varying Crystallinity. Clays and Clay Minerals, 33(5): 369-378.

Sharma, R.K., Sharma, P. and Maitra, A., 2003. Size-dependent catalytic behavior of platinum nanoparticles on the hexacyanoferrate(III)/thiosulfate redox reaction. Journal of Colloid and Interface Science, 265(1): 134-140.

Shipway, A.N., Lahav, M., Gabai, R. and Willner, I., 2000. Investigations into the electrostatically induced aggregation of Au nanoparticles. Langmuir, 16(23): 8789-8795.

Somorjai, G.A., 1994. Introduction to surface chemistry and catalysis. Wiley, New York, 667 pp.

Son, D.H., Hughes, S.M., Yin, Y.D. and Alivisatos, A.P., 2004. Cation exchange reactions-in ionic nanocrystals. Science, 306(5698): 1009-1012.

Sonnichsen, C. and Alivisatos, A.P., 2005. Gold nanorods as novel nonbleaching plasmon-based orientation sensors for polarized single-particle microscopy. Nano Letters, 5(2): 301-304.

Stouwdam, J.W. et al., 2007. Photostability of colloidal PbSe and PbSe/PbS core/shell nanocrystals in solution and in the solid state. Journal of Physical Chemistry C, 111: 1086-1092.

Sund, C.J., McMasters, S., Crittenden, S.R., Harrell, L.E. and Sumner, J.J., 2007. Effect of electron mediators on current generation and fermentation in a microbial fuel cell. Applied Microbiology and Biotechnology, 76(3): 561-568.

Tang, R.K. et al., 2005. Control of biomineralization dynamics by interfacial energies. Angewandte Chemie-International Edition, 44(24): 3698-3702.

Tang, R.K. and Nancollas, G.H., 2002. New mechanism for the dissolution of sparingly soluble minerals. Pure and Applied Chemistry, 74(10): 1851-1857.

Tang, R.K., Nancollas, G.H. and Orme, C.A., 2001. Mechanism of dissolution of sparingly soluble electrolytes. Journal of the American Chemical Society, 123: 5437-5443.

Tang, R.K., Orme, C.A. and Nancollas, G.H., 2003. A new understanding of demineralization: The dynamics of brushite dissolution. Journal of Physical Chemistry B, 107(38): 10653-10657.

Tang, R.K., Orme, C.A. and Nancollas, G.H., 2004a. Dissolution of crystallites: Surface energetic control and size effects. Chemphyschem, 5(5): 688-696.

Tang, R.K., Wang, L.J. and Nancollas, G.H., 2004b. Size-effects in the dissolution of hydroxyapatite: an understanding of biological demineralization. Journal of Materials Chemistry, 14(14): 2341-2346.

Tang, R.K. et al., 2004c. Dissolution at the nanoscale: Self-preservation of biominerals. Angewandte Chemie-International Edition, 43(20): 2697-2701.

Thurston, T.R. and Wilcoxon, J.P., 1999. Photooxidation of organic chemicals catalyzed by nanoscale MoS2. Journal of Physical Chemistry B, 103(1): 11-17.

Torrent, J., Schwertmann, U. and Barron, V., 1987. The Reductive Dissolution of Synthetic Goethite and Hematite in Dithionite. Clay Minerals, 22(3): 329-337.
Tratnyek, P.G. and Johnson, R.L., 2006. Nanotechnologies for environmental cleanup. Nano Today, 1(2): 44-48.
Tsodikov, M.V. et al., 2005. Structure and size effects in catalysis by immobilized nanoclusters of iron oxides. Catalysis Today, 105(3-4): 634-640.
Valden, M., Lai, X. and Goodman, D.W., 1998. Onset of catalytic activity of gold clusters on titania with the appearance of nonmetallic properties. Science, 281(5383): 1647-1650.
Vayssieres, L. et al., 2005. One-dimensional quantum-confinement effect in alpha-Fe2O3 ultrafine nanorod arrays. Advanced Materials, 17(19): 2320-+.
Vikesland, P.J., Heathcock, A.M., Rebodos, R.L. and Makus, K.E., 2007. Particle size and aggregation effects on magnetite reactivity toward carbon tetrachloride. Environmental Science & Technology, 41(15): 5277-5283.
Wang, L.S., Li, X. and Zhang, H.F., 2000. Probing the electronic structure of iron clusters using photoelectron spectroscopy. Chemical Physics, 262: 53-63.
Waychunas, G.A., Kim, C.S. and Banfield, J.F., 2005. Nanoparticulate iron oxide minerals in soils and sediments: unique properties and contaminant scavenging mechanisms. Journal of Nanoparticle Research, 7(4-5): 409-433.
Wigginton, N.S., Haus, K.L. and Hochella, M.F., 2007. Aquatic environmental nanoparticles. Journal of Environmental Monitoring, 9: 1306-1316.
Wilcoxon, J.P., 2000. Catalytic Photooxidation of Pentachlorophenol Using Semiconductor Nanoclusters. Journal of Physical Chemistry B, 104: 7334-7343.
Yang, Z.H. and Xie, C.S., 2006. Zn2+ release from zinc and zinc oxide particles in simulated uterine solution. Colloids and Surfaces B-Biointerfaces, 47(2): 140-145.
Yavuz, C.T. et al., 2006. Low-field magnetic separation of monodisperse Fe3O4 nanocrystals. Science, 314(5801): 964-967.
Yean, S. et al., 2005. Effect of magnetite particle size on adsorption and desorption of arsenite and arsenate. Journal of Materials Research, 20(12): 3255-3264.
Yin, Y. and Alivisatos, A.P., 2005. Colloidal nanocrystal synthesis and the organic-inorganic interface. Nature, 437(7059): 664-670.
Yin, Y.D., Erdonmez, C.K., Cabot, A., Hughes, S. and Alivisatos, A.P., 2006. Colloidal synthesis of hollow cobalt sulfide nanocrystals. Advanced Functional Materials, 16(11): 1389-1399.
Yin, Y.D. et al., 2004. Formation of hollow nanocrystals through the nanoscale Kirkendall Effect. Science, 304(5671): 711-714.
Yu, W.W. et al., 2007. Forming biocompatible and nonaggregated nanocrystals in water using amphiphilic polymers. Journal of the American Chemical Society, 129(10): 2871-2879.
Yuan, G.D., 2004. Natural and modified nanomaterials as sorbents of environmental contaminants. Journal of Environmental Science and Health Part A--Toxic/Hazardous Substances and Environmental Engineering, A39(10): 2661-2670.
Zelmanov, G. and Semiat, R., 2008. Iron(3) oxide-based nanoparticles as catalysts in advanced organic aqueous oxidation. Water Research, 42: 492-498.

Zhang, H.Z. and Banfield, J.F., 2007. Polymorphic transformations and particle coarsening in nanocrystalline titania ceramic powders and membranes. Journal of Physical Chemistry C, 111(18): 6621-6629.

Zhang, H.Z., Penn, R.L., Hamers, R.J. and Banfield, J.F., 1999. Enhanced adsorption of molecules on surfaces of nanocrystalline particles. Journal of Physical Chemistry B, 103(22): 4656-4662.

Zhang, J.W. and Nancollas, G.H., 1990. Mechanisms of growth and dissolution of sparingly soluble salts. In: M.F. Hochella and A.F. White (Editors), Mineral-water Interface Geochemistry. Reviews in Mineralogy. Mineralogical Society of America, Washington, D.C., pp. 603.

Zhang, W.X., 2003. Nanoscale iron particles for environmental remediation: An overview. Journal of Nanoparticle Research, 5(3-4): 323-332.

Zhang, W.X., Wang, C.B. and Lien, H.L., 1998. Treatment of chlorinated organic contaminants with nanoscale bimetallic particles. Catalysis Today, 40(4): 387-395.